The Astrophysical Journal, 716:30–70, 2010 June 10 doi:10.1088/0004-637X/716/1/30

THE SPECTRAL ENERGY DISTRIBUTION OF *FERMI* BRIGHT BLAZARS

A. A. Abdo[1,2], M. Ackermann[3], I. Agudo[4], M. Ajello[3], H. D. Aller[5], M. F. Aller[5], E. Angelakis[6], A. A. Arkharov[7], M. Axelsson[8,9,10], U. Bach[6], L. Baldini[11], J. Ballet[12], G. Barbiellini[13,14], D. Bastieri[15,16], B. M. Baughman[17], K. Bechtol[3], R. Bellazzini[11], E. Benitez[18], A. Berdyugin[19], B. Berenji[3], R. D. Blandford[3], E. D. Bloom[3], M. Boettcher[20], E. Bonamente[21,22], A. W. Borgland[3], J. Bregeon[11], A. Brez[11], M. Brigida[23,24], P. Bruel[25], T. H. Burnett[26], D. Burrows[27], S. Buson[15], G. A. Caliandro[28], L. Calzoletti[29], R. A. Cameron[3], M. Capalbi[29], P. A. Caraveo[30], D. Carosati[31], J. M. Casandjian[12], E. Cavazzuti[29], C. Cecchi[21,22], Ö. Çelik[32,33,34], E. Charles[3], S. Chaty[12], A. Chekhtman[1,35], W. P. Chen[36], J. Chiang[3], G. Chincarini[37], S. Ciprini[22], R. Claus[3], J. Cohen-Tanugi[38], S. Colafrancesco[29], L. R. Cominsky[39], J. Conrad[10,40,90], L. Costamante[3], S. Cutini[29], F. D'Ammando[41], R. Deitrick[42], V. D'Elia[29], C. D. Dermer[1], A. de Angelis[43], F. de Palma[23,24], S. W. Digel[3], I. Donnarumma[41], E. do Couto e Silva[3], P. S. Drell[3], R. Dubois[3], D. Dultzin[18], D. Dumora[44,45], A. Falcone[27], C. Farnier[38], C. Favuzzi[23,24], S. J. Fegan[25], W. B. Focke[3], E. Forné[46], P. Fortin[25], M. Frailis[43,47], L. Fuhrmann[6], Y. Fukazawa[48], S. Funk[3], P. Fusco[23,24], J. L. Gómez[4], F. Gargano[24], D. Gasparrini[29], N. Gehrels[32], S. Germani[21,22], B. Giebels[25], N. Giglietto[23,24], P. Giommi[29], F. Giordano[23,24], A. Giuliani[30], T. Glanzman[3], G. Godfrey[3], I. A. Grenier[12], C. Gronwall[27], J. E. Grove[1], L. Guillemot[6,44,45], S. Guiriec[49], M. A. Gurwell[50], D. Hadasch[51], Y. Hanabata[48], A. K. Harding[32], M. Hayashida[3], E. Hays[32], S. E. Healey[3], J. Heidt[52], D. Hiriart[53], D. Horan[25], E. A. Hoversten[27], R. E. Hughes[17], R. Itoh[48], M. S. Jackson[10,54], G. Jóhannesson[3], A. S. Johnson[3], W. N. Johnson[1], S. G. Jorstad[55], M. Kadler[33,56,57,58], T. Kamae[3], H. Katagiri[48], J. Kataoka[59], N. Kawai[60,61], J. Kennea[27], M. Kerr[26], G. Kimeridze[62], J. Knödlseder[63], M. L. Kocian[3], E. N. Kopatskaya[64], E. Koptelova[36], T. S. Konstantinova[64], Y. Y. Kovalev[6,65], Yu. A. Kovalev[65], O. M. Kurtanidze[62], M. Kuss[11], J. Lande[3], V. M. Larionov[64], L. Latronico[11], P. Leto[66], E. Lindfors[19], F. Longo[13,14], F. Loparco[23,24], B. Lott[44,45], M. N. Lovellette[1], P. Lubrano[21,22], G. M. Madejski[3], A. Makeev[1,35], P. Marchegiani[67], A. P. Marscher[55], F. Marshall[32], W. Max-Moerbeck[68], M. N. Mazziotta[24], W. McConville[32,69], J. E. McEnery[32,69], C. Meurer[10,40], P. F. Michelson[3], W. Mitthumsiri[3], T. Mizuno[48], A. A. Moiseev[33,69], C. Monte[23,24], M. E. Monzani[3], A. Morselli[70], I. V. Moskalenko[3], S. Murgia[3], I. Nestoras[6], K. Nilsson[19], N. A. Nizhelsky[71], P. L. Nolan[3], J. P. Norris[42], E. Nuss[38], T. Ohsugi[72], R. Ojha[73], N. Omodei[3], E. Orlando[74], J. F. Ormes[42], J. Osborne[75], M. Ozaki[76], L. Pacciani[41], P. Padovani[77], C. Pagani[27], K. Page[75], D. Paneque[3], J. H. Panetta[3], D. Parent[1,35,44,45], M. Pasanen[19], V. Pavlidou[68], V. Pelassa[38], M. Pepe[21,22], M. Perri[29], M. Pesce-Rollins[11], S. Piranomonte[78], F. Piron[38], C. Pittori[29], T. A. Porter[3], S. Puccetti[29], F. Rahoui[12], S. Rainò[23,24], C. Raiteri[79], R. Rando[15,16], M. Razzano[11], A. Reimer[3,80], O. Reimer[3,80], T. Reposeur[44,45], J. L. Richards[68], S. Ritz[81], L. S. Rochester[3], A. Y. Rodriguez[28], R. W. Romani[3], J. A. Ros[46], M. Roth[26], P. Roustazadeh[20], F. Ryde[10,54], H. F.-W. Sadrozinski[81], A. Sadun[82], D. Sanchez[25], A. Sander[17], P. M. Saz Parkinson[81], J. D. Scargle[83], A. Sellerholm[10,40], C. Sgrò[11], M. S. Shaw[3], L. A. Sigua[62], E. J. Siskind[84], D. A. Smith[44,45], P. D. Smith[17], G. Spandre[11], P. Spinelli[23,24], J.-L. Starck[12], M. Stevenson[68], G. Stratta[29], M. S. Strickman[1], D. J. Suson[85], H. Tajima[3], H. Takahashi[72], T. Takahashi[76], L. O. Takalo[19], T. Tanaka[3], J. B. Thayer[3], J. G. Thayer[3], D. J. Thompson[32], L. Tibaldo[12,15,16,91], D. F. Torres[28,51], G. Tosti[21,22], A. Tramacere[3,86,87], Y. Uchiyama[3], T. L. Usher[3], V. Vasileiou[33,34], F. Verrecchia[29], N. Vilchez[63], M. Villata[79], V. Vitale[70,88], A. P. Waite[3], P. Wang[3], B. L. Winer[17], K. S. Wood[1], T. Ylinen[10,54,89], J. A. Zensus[6], G. V. Zhekanis[71], and M. Ziegler[81]

[1] Space Science Division, Naval Research Laboratory, Washington, DC 20375, USA
[2] National Research Council Research Associate, National Academy of Sciences, Washington, DC 20001, USA
[3] W. W. Hansen Experimental Physics Laboratory, Kavli Institute for Particle Astrophysics and Cosmology, Department of Physics and SLAC National Accelerator Laboratory, Stanford University, Stanford, CA 94305, USA
[4] Instituto de Astrofisica de Andalucía, CSIC, 18080 Granada, Spain
[5] Department of Astronomy, University of Michigan, Ann Arbor, MI 48109-1042, USA
[6] Max-Planck-Institut für Radioastronomie, Auf dem Hügel 69, 53121 Bonn, Germany
[7] Pulkovo Observatory, 196140 St. Petersburg, Russia
[8] Department of Astronomy, Stockholm University, SE-106 91 Stockholm, Sweden
[9] Lund Observatory, SE-221 00 Lund, Sweden
[10] The Oskar Klein Centre for Cosmoparticle Physics, AlbaNova, SE-106 91 Stockholm, Sweden
[11] Istituto Nazionale di Fisica Nucleare, Sezione di Pisa, I-56127 Pisa, Italy
[12] Laboratoire AIM, CEA-IRFU/CNRS/Université Paris Diderot, Service d'Astrophysique, CEA Saclay, 91191 Gif sur Yvette, France
[13] Istituto Nazionale di Fisica Nucleare, Sezione di Trieste, I-34127 Trieste, Italy
[14] Dipartimento di Fisica, Università di Trieste, I-34127 Trieste, Italy
[15] Istituto Nazionale di Fisica Nucleare, Sezione di Padova, I-35131 Padova, Italy
[16] Dipartimento di Fisica "G. Galilei," Università di Padova, I-35131 Padova, Italy
[17] Department of Physics, Center for Cosmology and Astro-Particle Physics, The Ohio State University, Columbus, OH 43210, USA
[18] Instituto de Astronomía, Universidad Nacional Autónoma de México, México, D.F., Mexico
[19] Tuorla Observatory, University of Turku, FI-21500 Piikkiö, Finland
[20] Department of Physics and Astronomy, Ohio University, Athens, OH 45701, USA
[21] Istituto Nazionale di Fisica Nucleare, Sezione di Perugia, I-06123 Perugia, Italy
[22] Dipartimento di Fisica, Università degli Studi di Perugia, I-06123 Perugia, Italy
[23] Dipartimento di Fisica "M. Merlin" dell'Università e del Politecnico di Bari, I-70126 Bari, Italy
[24] Istituto Nazionale di Fisica Nucleare, Sezione di Bari, 70126 Bari, Italy
[25] Laboratoire Leprince-Ringuet, École Polytechnique, CNRS/IN2P3, Palaiseau, France

[26] Department of Physics, University of Washington, Seattle, WA 98195-1560, USA
[27] Department of Astronomy and Astrophysics, Pennsylvania State University, University Park, PA 16802, USA
[28] Institut de Ciencies de l'Espai (IEEC-CSIC), Campus UAB, 08193 Barcelona, Spain
[29] Agenzia Spaziale Italiana (ASI) Science Data Center, I-00044 Frascati (Roma), Italy
[30] INAF-Istituto di Astrofisica Spaziale e Fisica Cosmica, I-20133 Milano, Italy
[31] EPT Observatories, Tijarafe, La Palma, Spain
[32] NASA Goddard Space Flight Center, Greenbelt, MD 20771, USA
[33] Center for Research and Exploration in Space Science and Technology (CRESST) and NASA Goddard Space Flight Center, Greenbelt, MD 20771, USA
[34] Department of Physics and Center for Space Sciences and Technology, University of Maryland Baltimore County, Baltimore, MD 21250, USA
[35] George Mason University, Fairfax, VA 22030, USA
[36] Graduate Institute of Astronomy, National Central University, Jhongli 32054, Taiwan
[37] Dipartimento di Fisica, Università degli Studi di Milano-Bicocca, 20126 Milano, Italy
[38] Laboratoire de Physique Théorique et Astroparticules, Université Montpellier 2, CNRS/IN2P3, Montpellier, France
[39] Department of Physics and Astronomy, Sonoma State University, Rohnert Park, CA 94928-3609, USA
[40] Department of Physics, Stockholm University, AlbaNova, SE-106 91 Stockholm, Sweden
[41] INAF-Istituto di Astrofisica Spaziale e Fisica Cosmica, I-00133 Roma, Italy
[42] Department of Physics and Astronomy, University of Denver, Denver, CO 80208, USA
[43] Dipartimento di Fisica, Università di Udine and Istituto Nazionale di Fisica Nucleare, Sezione di Trieste, Gruppo Collegato di Udine, I-33100 Udine, Italy
[44] CNRS/IN2P3, Centre d'Études Nucléaires Bordeaux Gradignan, UMR 5797, Gradignan, 33175, France
[45] Université de Bordeaux, Centre d'Études Nucléaires Bordeaux Gradignan, UMR 5797, Gradignan, 33175, France
[46] Agrupació Astronòmica de Sabadell, 08206 Sabadell, Spain
[47] Osservatorio Astronomico di Trieste, Istituto Nazionale di Astrofisica, I-34143 Trieste, Italy
[48] Department of Physical Sciences, Hiroshima University, Higashi-Hiroshima, Hiroshima 739-8526, Japan
[49] Center for Space Plasma and Aeronomic Research (CSPAR), University of Alabama in Huntsville, Huntsville, AL 35899, USA
[50] Harvard-Smithsonian Center for Astrophysics, Cambridge, MA 02138, USA
[51] Institució Catalana de Recerca i Estudis Avançats (ICREA), Barcelona, Spain
[52] Landessternwarte, Universität Heidelberg, Königstuhl, D 69117 Heidelberg, Germany
[53] Instituto de Astronomía, Universidad Nacional Autónoma de México, Ensenada, B.C., Mexico
[54] Department of Physics, Royal Institute of Technology (KTH), AlbaNova, SE-106 91 Stockholm, Sweden
[55] Institute for Astrophysical Research, Boston University, Boston, MA 02215, USA
[56] Dr. Remeis-Sternwarte Bamberg, Sternwartstrasse 7, D-96049 Bamberg, Germany
[57] Erlangen Centre for Astroparticle Physics, D-91058 Erlangen, Germany
[58] Universities Space Research Association (USRA), Columbia, MD 21044, USA
[59] Research Institute for Science and Engineering, Waseda University, 3-4-1, Okubo, Shinjuku, Tokyo, 169-8555, Japan
[60] Department of Physics, Tokyo Institute of Technology, Meguro City, Tokyo 152-8551, Japan
[61] Cosmic Radiation Laboratory, Institute of Physical and Chemical Research (RIKEN), Wako, Saitama 351-0198, Japan
[62] Abastumani Observatory, Mt. Kanobili, 0301 Abastumani, Georgia
[63] Centre d'Étude Spatiale des Rayonnements, CNRS/UPS, BP 44346, F-30128 Toulouse Cedex 4, France
[64] Astronomical Institute, St. Petersburg State University, St. Petersburg, Russia
[65] Astro Space Center of the Lebedev Physical Institute, 117810 Moscow, Russia
[66] Osservatorio Astrofisico di Catania, 95123 Catania, Italy
[67] Physics Department,, Università di Roma "La Sapienza," I-00185 Roma, Italy
[68] Cahill Center for Astronomy and Astrophysics, California Institute of Technology, Pasadena, CA 91125, USA
[69] Department of Physics and Department of Astronomy, University of Maryland, College Park, MD 20742, USA
[70] Istituto Nazionale di Fisica Nucleare, Sezione di Roma "Tor Vergata," I-00133 Roma, Italy
[71] Special Astrophysical Observatory, Nizhnij Arkhyz, Karachai-Cherkessian Republic 369167, Russia
[72] Hiroshima Astrophysical Science Center, Hiroshima University, Higashi-Hiroshima, Hiroshima 739-8526, Japan
[73] U. S. Naval Observatory, Washington, DC 20392, USA
[74] Max-Planck Institut für extraterrestrische Physik, 85748 Garching, Germany
[75] Department of Physics and Astronomy, University of Leicester, Leicester, LE1 7RH, UK
[76] Institute of Space and Astronautical Science, JAXA, 3-1-1 Yoshinodai, Sagamihara, Kanagawa 229-8510, Japan
[77] European Organization for Astronomical Research in the Southern Hemisphere (ESO), D-85748 Garching bei München, Germany
[78] Osservatorio Astronomico di Roma, 00040 Monte Porzio Catone, Italy
[79] INAF, Osservatorio Astronomico di Torino, I-10025 Pino Torinese (TO), Italy
[80] Institut für Astro- und Teilchenphysik and Institut für Theoretische Physik, Leopold-Franzens-Universität Innsbruck, A-6020 Innsbruck, Austria
[81] Santa Cruz Institute for Particle Physics, Department of Physics and Department of Astronomy and Astrophysics, University of California at Santa Cruz, Santa Cruz, CA 95064, USA
[82] Department of Physics, University of Colorado, Denver, CO 80220, USA
[83] Space Sciences Division, NASA Ames Research Center, Moffett Field, CA 94035-1000, USA
[84] NYCB Real-Time Computing Inc., Lattingtown, NY 11560-1025, USA
[85] Department of Chemistry and Physics, Purdue University Calumet, Hammond, IN 46323-2094, USA
[86] Consorzio Interuniversitario per la Fisica Spaziale (CIFS), I-10133 Torino, Italy
[87] INTEGRAL Science Data Centre, CH-1290 Versoix, Switzerland
[88] Dipartimento di Fisica, Università di Roma "Tor Vergata," I-00133 Roma, Italy
[89] School of Pure and Applied Natural Sciences, University of Kalmar, SE-391 82 Kalmar, Sweden
Received 2009 December 4; accepted 2010 March 27; published 2010 May 13

ABSTRACT

We have conducted a detailed investigation of the broadband spectral properties of the γ-ray selected blazars of the *Fermi* LAT Bright AGN Sample (LBAS). By combining our accurately estimated *Fermi* γ-ray spectra with *Swift*, radio, infra-red, optical, and other hard X-ray/γ-ray data, collected within 3 months of the LBAS data taking period, we were able to assemble high-quality and quasi-simultaneous spectral energy distributions (SED) for 48 LBAS blazars. The SED of these γ-ray sources is similar to that of blazars discovered at other

wavelengths, clearly showing, in the usual log ν–log νF_ν representation, the typical broadband spectral signatures normally attributed to a combination of low-energy synchrotron radiation followed by inverse Compton emission of one or more components. We have used these SED to characterize the peak intensity of both the low- and the high-energy components. The results have been used to derive empirical relationships that estimate the position of the two peaks from the broadband colors (i.e., the radio to optical, $\alpha_{\rm ro}$, and optical to X-ray, $\alpha_{\rm ox}$, spectral slopes) and from the γ-ray spectral index. Our data show that the synchrotron peak frequency ($\nu^S_{\rm peak}$) is positioned between $10^{12.5}$ and $10^{14.5}$ Hz in broad-lined flat spectrum radio quasars (FSRQs) and between 10^{13} and 10^{17} Hz in featureless BL Lacertae objects. We find that the γ-ray spectral slope is strongly correlated with the synchrotron peak energy and with the X-ray spectral index, as expected at first order in synchrotron–inverse Compton scenarios. However, simple homogeneous, one-zone, synchrotron self-Compton (SSC) models cannot explain most of our SED, especially in the case of FSRQs and low energy peaked (LBL) BL Lacs. More complex models involving external Compton radiation or multiple SSC components are required to reproduce the overall SED and the observed spectral variability. While more than 50% of known radio bright high energy peaked (HBL) BL Lacs are detected in the LBAS sample, only less than 13% of known bright FSRQs and LBL BL Lacs are included. This suggests that the latter sources, as a class, may be much fainter γ-ray emitters than LBAS blazars, and could in fact radiate close to the expectations of simple SSC models. We categorized all our sources according to a new physical classification scheme based on the generally accepted paradigm for Active Galactic Nuclei and on the results of this SED study. Since the LAT detector is more sensitive to flat spectrum γ-ray sources, the correlation between $\nu^S_{\rm peak}$ and γ-ray spectral index strongly favors the detection of high energy peaked blazars, thus explaining the *Fermi* overabundance of this type of sources compared to radio and EGRET samples. This selection effect is similar to that experienced in the soft X-ray band where HBL BL Lacs are the dominant type of blazars.

Key words: BL Lacertae objects: general – galaxies: active – gamma rays: galaxies – quasars: general – radiation mechanisms: non-thermal

Online-only material: color figures

1. INTRODUCTION

The Large Area Telescope (LAT) on board the *Fermi Gamma Ray Space Telescope*, launched on 2008 June 11, provides unprecedented sensitivity in the γ-ray band (20 MeV to over 300 GeV; Atwood et al. 2009) with a large increase over its predecessors EGRET (Thompson et al. 1993), and *AGILE*, an Italian small γ-ray astronomy mission launched in 2007 (Tavani et al. 2008). The first three months of operations in the sky-survey mode led to the compilation of a list of 205 γ-ray sources with statistical significance larger than 10σ (Abdo et al. 2009a). As largely expected from the results of EGRET and *AGILE*, most of the high Galactic latitude sources in this catalog are blazars (Abdo et al. 2009b), a type of active galactic nucleus (AGN) well known to display extreme observational properties like large and rapid variability, apparent super-luminal motion, flat or inverted radio spectrum, and large and variable polarization. According to a widely accepted scenario, blazars are thought to be objects emitting non-thermal radiation across the entire electromagnetic spectrum from a relativistic jet that is viewed closely along the line of sight, thus causing strong relativistic amplification (e.g., Blandford & Rees 1978; Urry & Padovani 1995).

Blazars are rare extragalactic objects as they are a subset of radio loud quasi-stellar objects (QSOs), which in turn are only $\approx$10% of radio quiet QSOs and Seyfert galaxies that are found in large numbers at optical and at X-ray frequencies. Despite that, the strong emission at all wavelengths that characterizes blazars makes them the dominant type of extragalactic sources in those energy windows where the accretion onto a supermassive black hole, or other thermal mechanisms, do not produce significant radiation. For instance, in the microwave band, Giommi & Colafrancesco (2004) showed that blazars are the largest population of extragalactic objects (see also Toffolatti et al. 1998). The same is true in the γ-ray band (Hartman et al. 1999; Abdo et al. 2009b) and at TeV energies where BL Lac objects are the most frequent type of sources found in the high Galactic latitude sky (e.g., Costamante & Ghisellini 2002; Colafrancesco & Giommi 2006), see, e.g., the Web-based TeVCat[92] catalog for an up-to-date list of TeV sources and Weekes (2008) for a recent review.

Blazars have been known and studied in different energy windows for over 40 years; however, many questions still remain open about their physics and demographics.

One of the most effective ways of studying the physical properties of blazars is through the use of multi-frequency data. This approach has been followed by a number of authors (e.g., Giommi et al. 1995; von Montigny et al. 1995; Sambruna et al. 1996; Fossati et al. 1998; Giommi et al. 2002; Nieppola et al. 2006; Padovani et al. 2006) who assembled the spectral energy distributions (SED) of many radio, X-ray, and γ-ray selected blazars. In all cases, however, the effectiveness of the method was limited by the availability of only sparse, often non-simultaneous, flux measurements covering a limited portion of the electromagnetic spectrum. The need to build simultaneous and detailed SED is usually addressed through the organization of specific multifrequency observation campaigns. However, so far these large efforts have been carried out almost exclusively on the occasion of large flaring events of a few bright and well-known blazars, e.g., 3C454.3 (Giommi et al. 2006; Abdo et al. 2010b; Vercellone et al. 2009), Mkn421 (Donnarumma et al. 2009), and PKS2155-304 (Aharonian et al. 2009).

With *Fermi*, *Swift*, and other high-energy astrophysics satellites simultaneously in orbit, complemented by other space and ground-based observatories, it is now possible to assemble high-quality data to build simultaneous and well-sampled SED of large and unbiased samples of AGNs.

[90] Royal Swedish Academy of Sciences Research Fellow, funded by a grant from the K. A. Wallenberg Foundation.
[91] Partially supported by the International Doctorate on Astroparticle Physics (IDAPP) program.

[92] http://tevcat.uchicago.edu/

In this paper, we study the broadband (radio to high-energy γ-ray) properties of the sample of *Fermi* bright blazars recently presented by Abdo et al. (2009b) and we derive the detailed SED of a subsample of 48 *Fermi* blazars using simultaneous or quasi-simultaneous data obtained from *Swift* and other ground- and space-based observatories. For the sake of brevity we will limit ourselves to presenting the data, to estimating some key parameters characterizing the SED, and to making some basic conclusions about the physics of blazars. Detailed fits, statistical studies, and more complete theoretical interpretations will be presented elsewhere. Full analysis of the LAT γ-ray spectra and γ-ray variability of all the LBAS sources is presented in dedicated papers (Abdo et al. 2010a, 2010b).

This paper is organized as follows. In Section 2, we present the sample; in Section 3, we describe the *Fermi* and *Swift* high energy data along with radio, near-infrared, optical, and other multi-frequency data. In Section 4, we build quasi-simultaneous SED for 48 LBAS AGNs. In Section 5, we use our SED to derive some key physical parameters such as the peak frequency of the synchrotron and inverse Compton power ($\nu^{S}_{\rm peak}$ and $\nu^{\rm IC}_{\rm peak}$) and the corresponding peak fluxes. We also describe an empirical method that can be used for approximating the synchrotron bump parameters from simple observational quantities such as $\alpha_{\rm ox}$ and $\alpha_{\rm ro}$. We then calculate physical parameters for all sources in the LBAS sample for which $\alpha_{\rm ox}$ and $\alpha_{\rm ro}$ are available from data in the literature. In Section 6, we derive a new physical classification of AGNs based on our findings and we categorize all our blazars accordingly. In Section 7, we discuss some physical implications of our findings. Finally, in Section 8 we summarize and discuss our results.

2. THE SAMPLE

The results of the first three months of operations of the *Fermi* γ-ray observatory, from 2008 August 4 to October 31, are described in Abdo et al. (2009a), who presented a list of 205 bright ($>10\sigma$) γ-ray sources. In a companion publication Abdo et al. (2009b) studied the AGN content of this list associating with high confidence 106 sources at $|b| > 10^{\circ}$ with AGNs; ten further sources were also associated with AGNs but with a lower degree of confidence. This sample has been named the "LAT Bright AGN Sample" or LBAS. The results of the Abdo et al. (2009b) paper that are most relevant for this work are as follows.

1. About 90% of the LBAS sources have been associated with AGNs listed in radio catalogs (CRATES/CGRaBS, BZCat), thus implying that the bright extragalactic γ-ray sky is confirmed to be dominated by radio-loud AGNs (flat spectrum radio quasars, FSRQs, BL Lacs, and radio galaxies).
2. The number of high-energy peaked (HBL) BL Lacs detected at GeV energies (even when not flaring) has risen to at least 10 (out of 42 BL Lacs) as compared to only one (out of 14 BL Lacs) detected by EGRET. Seven LBAS BL Lacs are known TeV blazars.
3. Only about one-third of the bright *Fermi* AGN were also detected by EGRET. This is a likely consequence of the strong variability and duty cycle of GeV blazars.
4. BL Lac objects make up almost half of the bright *Fermi* AGN sample, which consists of 58 FSRQs, 42 BL Lac objects, two radio galaxies, and four AGNs of unknown type; the BL Lac fraction in the 3EG catalog was only ~23%. This is probably the result of a selection effect induced by the different response of the EGRET and LAT instruments.
5. HBL BL Lacs show significantly harder spectra than FSRQs and low energy peaked (LBL) BL Lacs.

Our purpose here is to study in detail the broadband spectral properties of all blazars in the LBAS sample. The main properties of our sources are reported in Table 1. Column 1 gives the γ-ray source name as it appears in Abdo et al. (2009a); Column 2 gives the name(s) of the blazar associated with the γ-ray source; Columns 3 and 4 give the precise equatorial coordinates taken from the BZCat catalog (Massaro et al. 2009) or from NED; Column 5 gives the redshift (when known); Columns 6 and 7 give the 5 GHz radio flux density and the optical apparent magnitude, $V_{\rm mag}$, from the CRATES (Healey et al. 2007) and from the USNO-B1 (Monet et al. 2003) catalogs respectively; Column 8 gives the 0.1–2.4 keV X-ray flux from the BZcat, or from recent *Swift* observations processed at the ASI Science Data Center (ASDC), as described in Section 3.2.4. All fluxes are as observed, that is, not corrected for Galactic absorption. Finally, Columns 9, 10, and 11 give the broadband (rest-frame) spectral slopes between 5 GHz and 5000 Å ($\alpha_{\rm ro}$), 5000 Å and 1 keV ($\alpha_{\rm ox}$), 5 GHz and 1 keV ($\alpha_{\rm rx}$), and 1 keV and 100 MeV ($\alpha_{\rm x\gamma}$) respectively, with α_{ab} defined as

$$\alpha_{ab} = -\frac{\log(f_a/f_b)}{\log(\nu_a/\nu_b)}, \quad (1)$$

where f_a is the rest-frame flux at frequency ν_a properly dereddened for Galaxy absorption. The flux measurements and the redshifts used for the calculation of $\alpha_{\rm ro}$, $\alpha_{\rm ox}$, $\alpha_{\rm rx}$, and $\alpha_{\rm x\gamma}$ are from Table 1 of this paper and from Table 3 of Abdo et al. (2009b). For the case of BL Lac objects without known redshift we have assumed $z = 0.4$.

3. MULTI-FREQUENCY OBSERVATIONS

In this section, we describe the multi-frequency observations of LBAS blazars carried out between 2008 August and October with *Fermi*, and between 2008 May and 2009 January with *Swift* and other space and ground-based facilities.

3.1. Fermi-LAT Data Analysis and γ-ray Energy Spectra

The LAT γ-ray spectra of all the LBAS sources are studied in detail in a dedicated paper (Abdo et al. 2010a) based on 6 months of *Fermi* data. Here we derive the detailed γ-ray spectra of the 48 blazars for which we build the quasi-simultaneous SED based on the three months of data used to define the LBAS sample.

The *Fermi*-LAT data from 2008 August 4 to October 31 have been analyzed, selecting for each source only photons belonging to the diffuse class (Pass6 V3 IRF; Atwood et al. 2009). Events within a 15° region of interest (RoI) centered around the source have been selected. In order to discard photons from the Earth albedo, events with zenith angles larger than 105° with respect to the Earth reference frame (Abdo et al. 2009a) have been excluded from the data samples.

A maximum likelihood analysis (*gtlike*)[93] has been used to reconstruct the source energy spectrum. A model is assumed for the source spectrum as well as for the diffuse background components, depending on a set of free parameters. The Galactic diffuse emission is modeled using the GALPROP package while the extragalactic one is described by a simple power law (Abdo et al. 2009a). The method has been implemented to estimate the

[93] http://fermi.gsfc.nasa.gov/ssc/data/analysis/documentation/Cicerone/Cicerone_Likelihood

Table 1
Sources List and Basic Parameters

LAT Name 0FGL	Counterpart Name(s)	R.A. (J2000.0)	Decl. (J2000.0)	Z	Radio Flux (6 cm, mJy)	$V_{\rm mag}$	X-ray Flux [a] (erg cm^{-2} s^{-1})	$\alpha_{\rm ro}$	$\alpha_{\rm ox}$	$\alpha_{\rm rx}$	$\alpha_{\rm x\gamma}$
(1)	(2)	(3)	(4)	(5)	(6)	(7)	(8)	(9)	(10)	(11)	(12)
J0017.4−0503	1RXS J001736.1-0/BZQJ0017-0512	00 17 35.8	−05 12 41.6	0.227	274	18.2	8.03e-13	0.59	1.28	0.83	0.57
J0033.6−1921	1RXS J003334.6-1/BZBJ0033-1921	00 33 34.3	−19 21 33.6	0.61	...	16.1	8.43e-12	0.23	1.08	0.53	1.04
J0050.5−0928	PKS0048-09/BZBJ0050-0929	00 50 41.2	−09 29 05.2	...	931	17.3	2.33e-12	0.52	1.46	0.84	0.72
J0051.1−0647	PKS0048-71/BZQJ0051-0650	00 51 08.2	−06 50 02.1	1.975	841	20.1	4.18e-13	0.85	1.02	0.93	0.59
J0100.2+0750	GB6J0100+0745	01 00 20.8	+07 45 50.4	...	101	...	...	...	...	...	0
J0112.1+2247	GC 0109+224/BZBJ0112+2244	01 12 05.8	+22 44 38.7	...	304	15.3	1.93e-12	0.33	1.67	0.79	0.74
J0118.7−2139	PKS 0116-219/BZQJ0118-2141	01 18 57.1	−21 41 30.0	1.165	559	20	1.42e-13	0.79	1.23	0.97	0.47
J0120.5−2703	1Jy0118-272/BZBJ0120-2701	01 20 31.6	−27 01 24.7	0.557	1000	16.5	7.22e-13	0.49	1.66	0.91	0.74
J0136.6+3903	1RXS J013632.9+3/BZBJ0136+3905	01 36 32.4	+39 05 59.3	...	49	15.4	9.6e-12	0.24	1.28	0.59	1.04
J0137.1+4751	S40133+47/BZQJ0136+4751	01 36 58.4	+47 51 29.0	0.859	2016	16.7	1.04e-12	0.71	1.25	0.93	0.64
J0144.5+2709	CLASSJ0144+2705	01 44 33.4	+27 05 03.0	...	263	19.6	...	0.71	...	...	0
J0145.1−2728	PKS 0142-278/BZQJ0145-2733	01 45 03.2	−27 33 34.3	1.148	833	18.4	5e-13	0.7	1.3	0.92	0.57
J0204.8−1704	PKS 0202-17/BZQJ0204-1701	02 04 57.5	−17 01 18.8	1.74	1350	18.5	5.66e-13	0.71	1.3	0.94	0.57
J0210.8−5100	PKS0208-512/BZUJ0210-5101	02 10 46.1	−51 01 01.8	1.003	3198	16.9	7.51e-13	0.59	1.66	0.97	0.54
J0217.8+0146	PKS 0215+015/BZQJ0217+0144	02 17 48.9	+01 44 49.7	1.715	1419	19.4	1.17e-12	0.79	0.96	0.9	0.67
J0220.9+3607	1Jy0218+357/BZUJ0221+3556	02 21 05.5	+35 56 13.9	0.944	1480	20	3.97e-13	0.94	0.99	0.97	0.53
J0222.6+4302	3C 66A/BZBJ0222+4302	02 22 39.6	+43 02 07.7	0.444	988	14.4	2.29e-12	0.41	1.68	0.84	0.66
J0229.5−3640	PKS0227-369/BZQJ0229-3643	02 29 28.3	−36 43 56.7	2.115	149	18.6	5.33e-13	0.76	0.82	0.82	0.53
J0238.4+2855	4C28.07/BZQJ0237+2848	02 37 52.3	+28 48 08.9	1.213	2794	17.8	5.77e-13	0.86	1.13	0.98	0.59
J0238.6+1636	PKS0235+164/BZBJ0238+1636	02 38 38.8	+16 36 59.2	0.94	1935	18.1	1.24e-12	0.75	1.15	0.92	0.51
J0245.6−4656	PKS0244-470	02 45 59.8	−46 51 17.1	...	852	18.2	7.71e-13	0.74	1.21	0.9	0.66
J0303.7−2410	PKS 0301-243/BZBJ0303-2407	03 03 26.5	−24 07 13.0	0.26	397	15.8	5.78e-12	0.43	1.33	0.74	0.9
J0334.1−4006	PKS0332-403/BZBJ0334-4008	03 34 13.6	−40 08 25.4	...	1331	16.7	7.34e-13	0.71	1.34	0.93	0.68
J0349.8−2102	PKS 0347-211/BZQJ0349-2102	03 49 57.7	−21 02 47.6	2.944	403	21.1	4.07e-13	0.76	0.98	0.89	0.49
J0407.6−3829	PKS0405-385/BZUJ0406-3826	04 06 58.9	−38 26 27.9	1.285	830	18.4	3.06e-13	0.62	1.46	0.95	0.56
J0412.9−5341	SUMSSJ041313-533	04 13 13.3	−53 31 58.6	...	95	19.7	...	0.59	...	...	0
J0423.1−0112	PKS0420-01/BZQJ0423-0120	04 23 15.7	−01 20 33.1	0.916	4357	15.1	1.39e-12	0.73	1.31	0.96	0.68
J0428.7−3755	PKS0426-380/BZBJ0428-3756	04 28 40.3	−37 56 19.6	1.03	1202	18	4.23e-13	0.54	1.61	0.95	0.5
J0449.7−4348	PKS0447-439/BZBJ0449-4350	04 49 24.7	−43 50 08.9	0.205	242	15.3	8.12e-12	0.35	1.35	0.69	0.83
J0457.1−2325	PKS0454-234/BZQJ0457-2324	04 57 03.1	−23 24 51.9	1.003	1863	17.9	4.68e-13	0.79	1.26	0.97	0.46
J0507.9+6739	1ES0502+675/BZBJ0507+6737	05 07 56.2	+67 37 24.3	0.416	27	17.7	1.29e-11	0.3	0.97	0.54	1.07
J0516.2−6200	MC4 0516-621/BZUJ0516-6207	05 16 44.8	−62 07 05.4	...	564	17.6	4.95e-13	0.78	1.14	0.9	0.64
J0531.0+1331	PKS 0528+134/BZQJ0530+1331	05 30 56.3	+13 31 55.2	2.07	3043	19.6	7.97e-13	0.75	1.2	0.97	0.53
J0538.8−4403	PKS0537-441/BZBJ0538-4405	05 38 50.2	−44 05 08.9	0.892	4805	15.2	2.1e-12	0.64	1.41	0.94	0.6
J0654.3+5042	GB6J0654+5042	06 54 22.0	+50 42 21.0	...	136	15.6	...	0.33	...	...	0
J0654.3+4513	S4 0650+45/BZUJ0654+4514	06 54 23.6	+45 14 23.4	0.933	467	18.9	2.38e-13	0.79	1.14	0.93	0.44
J0700.0−6611	PKS0700-661	07 00 31.0	−66 10 44.2	...	245	14.8	3.53e-13	0.31	1.96	0.87	0.66
J0712.9+5034	BZBJ0712+5033	07 12 43.6	+50 33 22.7	...	127	19.3	2.48e-13	0.55	1.45	0.85	0.62
J0714.2+1934	87GB071100.0+194	07 13 55.6	+19 35 03.9	...	116	18.6	...	0.55	...	...	0
J0719.4+3302	GB2 0716+332/BZUJ0719+3307	07 19 19.3	+33 07 09.6	0.779	321	16.3	2.51e-13	0.64	1.35	0.91	0.54
J0722.0+7120	S50716+714/BZBJ0721+7120	07 21 53.4	+71 20 36.3	...	859	14.6	2.27e-12	0.39	1.71	0.84	0.69
J0730.4−1142	PKS0727-11/BZQJ0730-1141	07 30 19.0	−11 41 12.5	1.589	5771	...	4.68e-13	0.87	1.19	1.03	0.48
J0738.2+1738	PKS0735+17/BZBJ0738+1742	07 38 07.3	+17 42 19.0	0.424	1812	15.7	9.67e-13	0.47	1.78	0.93	0.72
J0818.3+4222	S4 0814+425/BZBJ0818+4222	08 18 16.0	+42 22 45.4	0.53	1866	18.6	3.23e-13	0.88	1.11	0.99	0.56
J0824.9+5551	OJ 535/BZQJ0824+5552	08 24 47.2	+55 52 42.7	1.417	1155	17.3	6.4e-13	0.77	1.18	0.93	0.56
J0855.4+2009	PKS0851+202/BZBJ0854+2006	08 54 48.7	+20 06 30.5	0.306	2908	15.4	1.72e-12	0.49	1.69	0.92	0.7
J0909.7+0145	PKS0907+022/BZBJ0909+0200	09 09 39.7	+02 00 05.2	...	218	18.3	...	0.68	...	...	0
J0921.2+4437	S40917+44/BZQJ0920+4441	09 20 58.3	+44 41 53.9	2.19	1085	16.6	1.04e-12	0.85	0.89	0.89	0.65
J0948.3+0019	1RXS J094856.9+0/BZQJ0948+0022	09 48 57.3	+00 22 25.6	0.585	295	17.7	5.24e-13	0.56	1.33	0.86	0.55
J0957.6+5522	4C55.17/BZQJ0957+5522	09 57 38.1	+55 22 57.7	0.896	2015	17.4	5.13e-13	0.73	1.41	0.97	0.62
J1012.9+2435	B2 1011+25/BZQJ1013+2449	10 12 41.2	+24 39 21.7	1.805	94	19.3	6.24e-13	0.38	1.51	0.79	0.65
J1015.2+4927	1H 1013+498/BZBJ1015+4926	10 15 04.0	+49 26 00.7	0.2	299	14.8	1.32e-11	0.38	1.23	0.68	0.98
J1015.9+0515	SDSSJ101603.13+0/BZQJ1016+0513	10 16 03.1	+05 13 02.3	1.713	593	19.9	...	0.84	...	...	0
J1034.0+6051	S4 1030+61/BZQJ1033+6051	10 33 51.4	+60 51 07.3	1.401	532	19.5	3.19e-13	0.82	1.03	0.92	0.54
J1053.7+4926	WE 1050+49W1/BZBJ1053+4929	10 53 44.0	+49 29 56.0	0.14	59	15.1	8.21e-13	0.14	1.9	0.74	0.98
J1054.5+2212	SDSSJ105430.62+2/BZBJ1054+2210	10 54 30.7	+22 10 55.3	...	55	18.8	2.55e-13	0.4	1.59	0.81	0.59
J1058.9+5629	RXJ10586+5628/BZBJ1058+5628	10 58 37.6	+56 28 11.2	0.143	247	15.4	3.13e-12	0.28	1.65	0.75	0.84
J1057.8+0138	4C01.28/BZUJ1058+0133	10 58 29.5	+01 33 58.7	0.888	3403	17.5	1.08e-12	0.75	1.27	0.96	0.72
J1100.2−8000	PKS1057-79/BZUJ1058-8003	10 58 43.3	−80 03 54.2	...	2130	18.5	4.34e-13	0.7	1.52	0.98	0.5
J1104.5+3811	MKN421/BZBJ1104+3812	11 04 27.3	+38 12 31.7	0.03	723	8.6	1.81e-10	−0.08	1.86	0.58	1.1
J1129.8−1443	PKS1127-145/BZQJ1130-1449	11 30 07.0	−14 49 27.4	1.184	4209	16.1	1.39e-12	0.72	1.37	0.95	0.65
J1146.7−3808	PKS1144-379/BZUJ1147-3812	11 47 01.3	−38 12 11.0	1.048	1825	16.7	9.06e-13	0.6	1.53	0.93	0.69
J1159.2+2912	4C29.45/BZQJ1159+2914	11 59 31.7	+29 14 44.8	0.729	1461	17	8.44e-13	0.67	1.4	0.92	0.61
J1218.0+3006	ON 325/BZBJ1217+3007	12 17 52.0	+30 07 00.5	0.13	478	13.7	2.49e-11	0.38	1.21	0.67	0.96

Table 1
(Continued)

LAT Name 0FGL	Counterpart Name(s)	R.A. (J2000.0)	Decl. (J2000.0)	Z	Radio Flux (6 cm, mJy)	V_{mag}	X-ray Flux [a] (erg cm^{-2} s^{-1})	α_{ro}	α_{ox}	α_{rx}	$\alpha_{x\gamma}$
(1)	(2)	(3)	(4)	(5)	(6)	(7)	(8)	(9)	(10)	(11)	(12)
J1221.7+2814	ON 231/BZBJ1221+2813	12 21 31.6	+28 13 58.5	0.102	1085	14.1	1.3e-12	0.23	2.14	0.88	0.71
J1229.1+0202	3C273/BZQJ1229+0203	12 29 06.7	+02 03 08.6	0.158	43572	13.2	6.31e-11	0.76	1.09	0.87	0.8
J1246.6−2544	PKS1244-255/BZQJ1246-2547	12 46 46.7	−25 47 49.3	0.635	2317	17.3	1.3e-12	0.67	1.33	0.92	0.7
J1248.7+5811	PG 1246+586/BZBJ1248+5820	12 48 18.7	+58 20 28.7	...	356	15.9	3.99e-12	0.35	1.55	0.76	0.87
J1253.4+5300	1RXS J125311.9+5/BZBJ1253+5301	12 53 11.8	+53 01 11.7	...	363	16.3	2.7e-13	0.5	1.7	0.91	0.6
J1256.1−0548	3C279/BZQJ1256-0547	12 56 11.0	−05 47 21.5	0.536	11192	16.9	2.09e-11	0.71	1.1	0.86	0.8
J1310.6+3220	1Jy1308+326/BZUJ1310+3220	13 10 28.6	+32 20 43.8	0.997	1447	19.9	5.28e-13	0.92	0.97	0.95	0.55
J1331.7−0506	PKS 1329-049/BZQJ1332-0509	13 32 04.3	−05 09 43.3	2.15	471	17.6	3e-13	0.72	1.22	0.92	0.5
J1333.3+5058	CLASSJ1333+5057	13 33 53.8	+50 57 35.7	1.362	51	20.6	...	0.71	...	...	0
J1355.0−1044	PKS1352-104/BZUJ1354-1041	13 54 46.4	−10 41 02.6	0.33	686	16.5	1.88e-12	0.6	1.27	0.84	0.72
J1427.1+2347	PG 1424+240/BZBJ1427+2348	14 27 00.3	+23 48 00.0	...	335	15	3.57e-12	0.34	1.57	0.76	0.84
J1457.6−3538	PKS1454-354/BZQJ1457-3539	14 57 26.7	−35 39 10.0	1.424	566	17.3	5.1e-13	0.77	1.09	0.9	0.47
J1504.4+1030	PKS1502+106/BZQJ1504+1029	15 04 24.9	+10 29 39.1	1.839	2325	18.8	1.6e-13	0.92	1.16	1.04	0.31
J1511.2−0536	4C-05.64/BZQJ1510-0543	15 10 53.5	−05 43 07.3	1.191	1742	16.6	4.56e-13	0.73	1.45	0.97	0.58
J1512.7−0905	PKS1510-08/BZQJ1512-0905	15 12 50.5	−09 05 59.7	0.36	...	16.2	1.15e-12	0.61	1.54	0.93	0.49
J1517.9−2423	APLIB/BZBJ1517-2422	15 17 41.8	−24 22 19.4	0.048	2013	10.9	1.05e-12	0.33	2.09	0.93	0.75
J1522.2+3143	B2 1520+31/BZQJ1522+3144	15 22 09.8	+31 44 14.3	1.487	302	20	1.77e-13	0.8	1.1	0.92	0.4
J1543.1+6130	1RXS J154256.6+6/BZBJ1542+6129	15 42 56.8	+61 29 55.2	...	121	15.8	5.17e-13	0.43	1.56	0.81	0.73
J1553.4+1255	PKS1551+130/BZQJ1553+1256	15 53 32.5	+12 56 51.6	1.29	742	17.2	...	0.66	...	...	0
J1555.8+1110	PG 1553+113/BZBJ1555+1111	15 55 43.0	+11 11 24.3	...	510	13.8	1.79e-11	0.34	1.39	0.69	0.97
J1625.8−2527	OS-237.8/BZUJ1625-2527	16 25 46.7	−25 27 38.3	0.786	3449	20.5	9.34e-14	0.99	1.23	1.1	0.39
J1625.9−2423	PMNJ1626-2426	16 26 59.7	−24 26 41.8	...	132	...	...	...	...	...	0
J1635.2+3809	4C38.41/BZQJ1635+3808	16 35 15.4	+38 08 04.4	1.814	3221	17.4	1.68e-13	0.78	1.49	1.06	0.41
J1641.4+3939	NRAO512/BZQJ1640+3946	16 40 29.5	+39 46 44.2	1.66	1117	18.5	3.46e-13	0.81	1.15	0.96	0.52
J1653.9+3946	MKR501/BZBJ1653+3945	16 53 52.2	+39 45 36.6	0.033	1375	9.2	3.69e-11	−0.03	2.13	0.71	1.11
J1719.3+1746	PKS 1717+177/BZBJ1719+1745	17 19 13.0	+17 45 06.4	0.137	559	17.5	3.57e-13	0.62	1.47	0.92	0.62
J1751.5+0935	OT 081/BZBJ1751+0939	17 51 32.8	+09 39 00.6	0.322	2455	16.6	1.18e-12	0.65	1.4	0.93	0.6
J1802.2+7827	S51803+784/BZBJ1800+7828	18 00 45.6	+78 28 04.0	0.68	2633	16	7.9e-13	0.6	1.57	0.96	0.67
J1847.8+3223	B21846+32A/BZQJ1848+3219	18 48 22.0	+32 19 02.6	0.798	762	18.3	1e-12	0.75	1.04	0.88	0.6
J1849.4+6706	4C66.20/BZQJ1849+6705	18 49 16.0	+67 05 41.7	0.657	845	17.5	4.07e-13	0.66	1.39	0.93	0.53
J1911.2−2011	1908-201/BZQJ1911-2006	19 11 09.5	−20 06 55.1	1.119	2053	17.6	1.77e-12	0.85	0.97	0.9	0.61
J1923.3−2101	PMNJ1923-2104/BZQJ1923-2104	19 23 32.1	−21 04 33.3	0.874	2885	14.9	7.67e-13	0.71	1.43	0.97	0.59
J2000.2+6506	1ES1959+650/BZBJ1959+6508	19 59 59.8	+65 08 54.7	0.047	238	12	3.53e-11	0.08	1.64	0.61	1.06
J2009.4−4850	1Jy2005-489/BZBJ2009-4849	20 09 25.3	−48 49 53.6	0.071	1192	10.6	3.32e-11	0.16	1.75	0.7	1.09
J2017.2+0602	CLASSJ2017+0603	20 17 13.3	+06 03 06.5	...	36	17.7	6.48e-14	0.35	1.85	0.86	0.53
J2025.6−0736	2022-077/BZQJ2025-0735	20 25 40.6	−07 35 52.6	1.388	879	17.6	6.29e-13	0.81	1.09	0.91	0.46
J2056.1−4715	PKS2052-47/BZQJ2056-4714	20 56 16.3	−47 14 47.6	1.491	2026	17.9	5.86e-13	0.82	1.16	0.96	0.57
J2139.4−4238	MH 2136-428/BZBJ2139-4239	21 39 24.1	−42 35 20.3	...	108	16.5	7.3e-13	0.34	1.64	0.78	0.66
J2143.2+1741	S32141+17/BZQJ2143+1743	21 43 35.5	+17 43 48.7	0.213	1006	15.1	6.3e-13	0.43	1.85	0.92	0.56
J2147.1+0931	1Jy2144+092/BZQJ2147+0929	21 47 10.0	+09 29 46.7	1.113	1233	17.7	5.95e-13	0.66	1.39	0.93	0.54
J2157.5+3125	B2 2155+31/BZQJ2157+3127	21 57 28.8	+31 27 01.4	1.486	452	20.4	2.44e-13	0.8	1.09	0.93	0.54
J2158.8−3014	PKS 2155-304/BZBJ2158-3013	21 58 52.0	−30 13 32.0	0.116	407	11.9	3.25e-10	0.22	1.07	0.51	1.13
J2202.4+4217	BLLAC/BZBJ2202+4216	22 02 43.2	+42 16 40.0	0.069	2940	14.9	1.58e-12	0.29	2.17	0.93	0.7
J2203.2+1731	PKS2201+171/BZQJ2203+1725	22 03 26.8	+17 25 48.2	1.076	834	13.2	4.61e-13	0.81	1.06	0.93	0.61
J2207.0−5347	PKS2204-54/BZQJ2207-5346	22 07 43.6	−53 46 33.8	1.215	1410	17.8	5.22e-13	0.8	1.19	0.95	0.55
J2229.8−0829	PKS2227-08/BZQJ2229-0832	22 29 40.0	−08 32 54.3	1.56	2423	18	3.74e-12	0.66	1.08	0.87	0.69
J2232.4+1141	4C-11.69/BZQJ2232+1143	22 32 36.4	+11 43 50.9	1.037	3967	16.5	1.26e-12	0.77	1.32	0.96	0.61
J2254.0+1609	3C454.3/BZQJ2253+1608	22 53 57.7	+16 08 53.5	0.859	14468	15.8	7.8e-12	0.58	1.55	0.93	0.53
J2325.3+3959	BZBJ2325+3957	23 25 17.8	+39 57 37.0	...	135	20.3	1.02e-13	0.5	1.7	0.91	0.59
J2327.3+0947	PKS2325+093/BZQJ2327+0940	23 27 33.4	+09 40 09.5	1.843	643	18.1	7.27e-13	0.77	1.04	0.89	0.54
J2345.5−1559	PMN 2345-1555/BZQJ2345-1555	23 45 12.4	−15 55 07.7	0.621	504	18.6	2.6e-13	0.7	1.28	0.93	0.51

Note. [a] 0.1–2.4 keV band.

parameters in each individual energy bin (two bins per decade, starting from 100 MeV), and the parameters obtained from the fits are used to evaluate the sources fluxes. For each energy bin the source under investigation and all nearby sources in the RoI are described by one parameter representing the integral flux in that energy bin. The diffuse background components are modeled with one single parameter each, describing the normalization. For each bin, only fit results with a significance larger than 3σ have been retained. Depending on the flux and energy spectrum, 4–7 bins had positive detections for each AGN in the sample. The results are shown in Table 2.

As a cross check a deconvolution technique (unfolding; Mazziotta 2009) has been used to reconstruct the source energy spectra from the observed data, after background subtraction. This method allows us to reconstruct the source spectrum from the data without assuming any spectral model, also taking into

Table 2
Results of *Fermi*-LAT Data Analysis (Flux in Units of photons MeV^{-1} cm^{-2} s^{-1})

LAT Name 0FGL	Band 1 100–316.2 MeV	Band 2 316.2–1000 MeV	Band 3 1000–3162.3 MeV	Band 4 3162.3–10000 MeV	Band 5 10000–31623 MeV	Band 6 31623–100000 MeV	Band 7 100000–316230 MeV
J0033.6−1921	...	(4.45 ± 1.06) 10^{-12}	(1.23 ± 0.28) 10^{-12}	(1.16 ± 0.47) 10^{-13}	(1.67 ± 0.96) 10^{-14}	...	...
J0050.5−0928	(3.83 ± 0.64) 10^{-10}	(3.83 ± 0.31) 10^{-11}	(3.04 ± 0.49) 10^{-12}	(2.02 ± 0.65) 10^{-13}	...	...	...
J0137.1+4751	(3.33 ± 0.72) 10^{-10}	(3.14 ± 0.44) 10^{-11}	(3.29 ± 0.50) 10^{-12}	(2.64 ± 0.72) 10^{-13}	...	...	...
J0210.8−5100	(9.20 ± 0.80) 10^{-10}	(7.23 ± 0.55) 10^{-11}	(5.99 ± 0.68) 10^{-12}	(2.87 ± 0.79) 10^{-13}	...	...	...
J0222.6+4302	(9.70 ± 0.47) 10^{-10}	(9.89 ± 0.49) 10^{-11}	(8.77 ± 0.72) 10^{-12}	(9.26 ± 1.35) 10^{-13}	(1.16 ± 0.25) 10^{-13}	(1.47 ± 0.49) 10^{-14}	(6.57 ± 6.14) 10^{-16}
J0229.5−3640	(6.18 ± 0.68) 10^{-10}	(3.26 ± 0.40) 10^{-11}	(2.08 ± 0.42) 10^{-12}	(7.60 ± 4.00) 10^{-14}	...	...	...
J0238.4+2855	(3.01 ± 0.65) 10^{-10}	(1.95 ± 0.37) 10^{-11}	(1.56 ± 0.38) 10^{-12}	(6.91 ± 4.04) 10^{-14}	...	...	...
J0238.6+1636	(2.63 ± 0.11) 10^{-9}	(2.64 ± 0.09) 10^{-10}	(2.74 ± 0.13) 10^{-11}	(2.27 ± 0.20) 10^{-12}	(9.74 ± 2.27) 10^{-14}	(2.12 ± 2.04) 10^{-15}	...
J0349.8−2102	(6.94 ± 0.71) 10^{-10}	(4.15 ± 0.32) 10^{-11}	(2.62 ± 0.47) 10^{-12}	(5.73 ± 3.74) 10^{-14}	...	...	...
J0423.1−0112	(5.92 ± 0.77) 10^{-10}	(2.33 ± 0.24) 10^{-11}	(1.52 ± 0.30) 10^{-12}	(1.25 ± 0.53) 10^{-13}	...	...	...
J0428.7−3755	(8.74 ± 0.78) 10^{-10}	(7.12 ± 0.43) 10^{-11}	(7.96 ± 0.76) 10^{-12}	(6.71 ± 1.18) 10^{-13}	(2.84 ± 1.28) 10^{-14}	...	...
J0449.7−4348	(4.31 ± 0.67) 10^{-10}	(3.38 ± 0.30) 10^{-11}	(4.60 ± 0.51) 10^{-12}	(4.02 ± 0.91) 10^{-13}	(4.10 ± 1.55) 10^{-14}	(2.55 ± 2.50) 10^{-15}	...
J0457.1−2325	(1.46 ± 0.09) 10^{-9}	(1.27 ± 0.06) 10^{-10}	(1.11 ± 0.09) 10^{-11}	(6.54 ± 1.15) 10^{-13}	(2.78 ± 1.25) 10^{-14}	...	...
J0507.9+6739	(9.77 ± 6.47) 10^{-11}	(1.16 ± 0.34) 10^{-11}	(5.66*e* ± 2.66) 10^{-13}	(1.74 ± 0.58) 10^{-13}	(7.13 ± 6.55) 10^{-15}	(7.27 ± 3.43) 10^{-15}	(1.07 ± 0.76) 10^{-15}
J0516.2−6200	(3.41 ± 0.71) 10^{-10}	(1.68 ± 0.21) 10^{-11}	(1.79 ± 0.40) 10^{-12}	(1.06 ± 0.50) 10^{-13}	(8.93 ± 8.13) 10^{-15}	...	...
J0531.0+1331	(9.52 ± 1.05) 10^{-10}	(5.35 ± 0.63) 10^{-11}	(3.50 ± 0.58) 10^{-12}	(1.21 ± 0.56) 10^{-13}	...	...	...
J0538.8−4403	(1.29 ± 0.09) 10^{-9}	(1.21 ± 0.06) 10^{-10}	(1.02 ± 0.09) 10^{-11}	(7.97 ± 1.30) 10^{-13}	(1.81 ± 1.05) 10^{-14}	(1.83 ± 1.82) 10^{-15}	...
J0712.9+5034	(8.82 ± 6.15) 10^{-11}	(1.65 ± 0.35) 10^{-11}	(1.42 ± 0.36) 10^{-12}	(9.94 ± 4.70) 10^{-14}	...	...	...
J0722.0+7120	(6.17 ± 0.72) 10^{-10}	(5.51 ± 0.46) 10^{-11}	(5.70 ± 0.60) 10^{-12}	(5.80 ± 1.00) 10^{-13}	(9.83 ± 7.05) 10^{-15}	...	...
J0730.4−1142	(1.25 ± 0.11) 10^{-9}	(8.46 ± 0.46) 10^{-11}	(7.43 ± 0.68) 10^{-12}	(3.33 ± 0.85) 10^{-13}	(3.85 ± 1.46) 10^{-14}	...	...
J0855.4+2009	(3.53 ± 0.64) 10^{-10}	(2.74 ± 0.38) 10^{-11}	(1.71 ± 0.39) 10^{-12}	(1.12 ± 0.50) 10^{-13}	...	...	...
J0921.2+4437	(3.62 ± 0.59) 10^{-10}	(2.02 ± 0.22) 10^{-11}	(1.55 ± 0.37) 10^{-12}	(1.47 ± 0.52) 10^{-13}	(1.08 ± 0.77) 10^{-14}	...	...
J1015.2+4927	(2.72 ± 0.58) 10^{-10}	(1.69 ± 0.31) 10^{-11}	(3.25 ± 0.49) 10^{-12}	(3.85 ± 0.87) 10^{-13}	(4.66 ± 1.63) 10^{-14}	(3.33 ± 2.35) 10^{-15}	...
J1057.8+0138	(2.73 ± 0.64) 10^{-10}	(1.13 ± 0.32) 10^{-11}	(1.44 ± 0.35) 10^{-12}	(9.10 ± 4.89) 10^{-14}	(8.84 ± 8.20) 10^{-15}	...	...
J1058.9+5629	(1.82 ± 0.58) 10^{-10}	(1.12 ± 0.16) 10^{-11}	(1.44 ± 0.29) 10^{-12}	(5.27 ± 3.30) 10^{-14}	...	...	...
J1104.5+3811	(5.67 ± 0.65) 10^{-10}	(6.04 ± 0.38) 10^{-11}	(8.54 ± 0.72) 10^{-12}	(1.06 ± 0.14) 10^{-12}	(7.40 ± 2.03) 10^{-14}	(2.71 ± 0.68) 10^{-14}	(2.47 ± 1.23) 10^{-15}
J1159.2+2912	(4.41 ± 0.65) 10^{-10}	(2.70 ± 0.26) 10^{-11}	(1.14 ± 0.32) 10^{-12}	(9.05 ± 4.46) 10^{-14}	...	...	...
J1221.7+2814	(2.66 ± 0.72) 10^{-10}	(3.20 ± 0.41) 10^{-11}	(4.07 ± 0.55) 10^{-12}	(2.78 ± 0.73) 10^{-13}	(2.68 ± 1.20) 10^{-14}	(3.72 ± 2.70) 10^{-15}	...
J1229.1+0202	(2.92 ± 0.11) 10^{-9}	(1.45 ± 0.06) 10^{-10}	(7.70 ± 0.73) 10^{-12}	(1.13 ± 0.49) 10^{-13}	(5.36 ± 5.37) 10^{-15}	...	...
J1248.7+5811	(1.66 ± 0.57) 10^{-10}	(1.48 ± 0.27) 10^{-11}	(1.40 ± 0.34) 10^{-12}	(8.65 ± 4.11) 10^{-14}	(1.84 ± 1.02) 10^{-14}	(4.84 ± 2.81) 10^{-15}	...

Table 2
(Continued)

LAT Name 0FGL	Band 1 100–316.2 MeV	Band 2 316.2–1000 MeV	Band 3 1000–3162.3 MeV	Band 4 3162.3–10000 MeV	Band 5 10000–31623 MeV	Band 6 31623–100000 MeV	Band 7 100000–316230 MeV
J1256.1−0547	$(9.69 \pm 0.83)\ 10^{-10}$	$(8.01 \pm 0.44)\ 10^{-11}$	$(5.66 \pm 0.59)\ 10^{-12}$	$(4.06 \pm 0.87)\ 10^{-13}$	$(1.90 \pm 1.05)\ 10^{-14}$	...	...
J1310.6+3220	$(6.42 \pm 0.67)\ 10^{-10}$	$(4.66 \pm 0.44)\ 10^{-11}$	$(3.76 \pm 0.52)\ 10^{-12}$	$(3.29 \pm 0.80)\ 10^{-13}$	...	...	...
J1457.6−3538	$(1.21 \pm 0.10)\ 10^{-9}$	$(1.24 \pm 0.06)\ 10^{-10}$	$(8.42 \pm 0.73)\ 10^{-12}$	$(5.07 \pm 1.03)\ 10^{-13}$	$(2.45 \pm 1.25)\ 10^{-14}$	...	...
J1504.4+1030	$(2.81 \pm 0.11)\ 10^{-9}$	$(2.67 \pm 0.08)\ 10^{-12}$	$(2.40 \pm 0.12)\ 10^{-11}$	$(1.75 \pm 0.18)\ 10^{-12}$	$(5.16 \pm 1.64)\ 10^{-14}$	$(5.23 \pm 2.97)\ 10^{-15}$	...
J1512.7−0905	$(2.23 \pm 0.11)\ 10^{-9}$	$(1.54 \pm 0.08)\ 10^{-10}$	$(8.83 \pm 0.80)\ 10^{-12}$	$(2.81 \pm 0.79)\ 10^{-13}$	$(5.02 \pm 5.63)\ 10^{-15}$	...	...
J1522.2+3143	$(9.36 \pm 0.73)\ 10^{-10}$	$(7.16 \pm 0.40)\ 10^{-11}$	$(4.87 \pm 0.56)\ 10^{-12}$	$(1.54 \pm 0.54)\ 10^{-13}$	$(4.95 \pm 4.99)\ 10^{-15}$	$(1.59 \pm 1.59)\ 10^{-15}$	...
J1543.1+6130	$(9.39 \pm 5.10)\ 10^{-11}$	$(9.49 \pm 2.63)\ 10^{-12}$	$(1.06 \pm 0.27)\ 10^{-12}$	$(1.23 \pm 0.49)\ 10^{-13}$	...	...	...
J1653.9+3946	$(7.02 \pm 6.26)\ 10^{-11}$	$(1.52 \pm 0.31)\ 10^{-11}$	$(1.97 \pm 0.38)\ 10^{-12}$	$(2.27 \pm 0.65)\ 10^{-13}$	$(3.90 \pm 1.45)\ 10^{-14}$	$(3.06 \pm 2.17)\ 10^{-15}$	$(5.41 \pm 5.40)\ 10^{-16}$
J1719.3+1746	$(1.46 \pm 0.61)\ 10^{-10}$	$(2.47 \pm 0.23)\ 10^{-11}$	$(4.31 \pm 0.48)\ 10^{-12}$	$(3.68 \pm 0.83)\ 10^{-13}$	$(3.61 \pm 1.37)\ 10^{-14}$	$(2.94 \pm 2.04)\ 10^{-15}$	...
J1751.5+0935	$(6.53 \pm 0.86)\ 10^{-10}$	$(4.74 \pm 3.22)\ 10^{-11}$	$(3.92 \pm 5.53)\ 10^{-12}$	$(2.64 \pm 0.69)\ 10^{-13}$	$(1.27 \pm 0.82)\ 10^{-14}$	...	...
J1849.4+6706	$(5.03 \pm 0.71)\ 10^{-10}$	$(4.55 \pm 0.32)\ 10^{-11}$	$(4.60 \pm 0.50)\ 10^{-12}$	$(2.57 \pm 0.65)\ 10^{-13}$	$(9.51 \pm 6.80)\ 10^{-15}$	...	...
J2000.2+6506	...	$(2.13 \pm 0.40)\ 10^{-11}$	$(1.88 \pm 0.39)\ 10^{-12}$	$(9.78 \pm 4.44)\ 10^{-14}$	$(5.06 \pm 1.61)\ 10^{-14}$	$(1.58 \pm 1.58)\ 10^{-15}$	...
J2143.2+1741	$(3.96 \pm 0.29)\ 10^{-10}$	$(2.77 \pm 0.25)\ 10^{-11}$	$(2.12 \pm 0.34)\ 10^{-12}$	...	...	...	...
J2158.8−3014	$(6.14 \pm 0.67)\ 10^{-10}$	$(7.50 \pm 0.55)\ 10^{-11}$	$(8.66 \pm 0.79)\ 10^{-12}$	$(9.41 \pm 1.38)\ 10^{-13}$	$(9.60 \pm 2.38)\ 10^{-14}$	...	...
J2202.4+4217	$(2.30 \pm 0.76)\ 10^{-10}$	$(2.57 \pm 0.45)\ 10^{-11}$	$(2.27 \pm 0.45)\ 10^{-12}$	$(7.49 \pm 4.05)\ 10^{-14}$	...	...	...
J2254.0+1609	$(9.76 \pm 0.17)\ 10^{-9}$	$(6.73 \pm 0.12)\ 10^{-10}$	$(4.59 \pm 0.17)\ 10^{-11}$	$(1.54 \pm 0.17)\ 10^{-12}$	$(1.97 \pm 1.00)\ 10^{-14}$	...	...
J2327.3+0947	$(5.98 \pm 0.71)\ 10^{-10}$	$(3.62 \pm 0.43)\ 10^{-11}$	$(1.69 \pm 0.37)\ 10^{-12}$	...	...	...	...
J2345.5−1559	$(4.25 \pm 0.59)\ 10^{-10}$	$(2.76 \pm 0.26)\ 10^{-11}$	$(1.56 \pm 0.38)\ 10^{-12}$	$(9.21 \pm 4.44)\ 10^{-14}$	...	...	...

account the finite energy dispersion of the detector. The results of the two different methods are consistent as illustrated in Appendix A.

Once the differential flux in each energy bin $\phi(E)$ has been evaluated, the corresponding SED is then obtained by multiplying the differential flux by the square of the central energy value of that bin, i.e., $\nu F(\nu) = E^2\phi(E)$ where $E = h\nu$. The vertical error bars represent only the statistical errors. The systematic uncertainties in the effective area for the Pass6 V3 DIFFUSE event selection have been estimated to be 10% at 100 MeV, 5% at 562 MeV, and 20% for energies greater than 10 GeV (Abdo et al. 2009c).

3.2. Swift Data

The *Swift* Gamma-Ray-Burst (GRB) Explorer (Gehrels et al. 2004) is a multi-frequency, rapid response space observatory that was launched on 2004 November 20. To fulfill its purposes *Swift* carries three instruments on board: the Burst Alert Telescope (BAT; Barthelmy et al. 2005) sensitive in the 15–150 keV band, the X-Ray Telescope (XRT; Burrows et al. 2005) sensitive in the 0.3–10.0 keV band, and the UV and Optical Telescope (170–600 nm, UVOT; Roming et al. 2005). The very wide spectral range covered by these three instruments is of crucial importance for blazar issues as it covers where the transition between the synchrotron and inverse Compton emission usually occurs.

The primary objective of the *Swift* scientific program is the discovery and rapid follow-up of GRBs. However, as these elusive sources explode at random times and their frequency of occurrence is subject to large statistical fluctuations, there are periods when *Swift* is not engaged with GRB observations and the observatory can be used for different scientific purposes. The sources observed through this secondary science program are usually called *Swift* fill-in targets. Since the beginning of its activities *Swift* has observed hundreds of blazars as part of the fill-in program (e.g., Giommi et al. 2007). With the launch of *AGILE* and *Fermi*, the rate of *Swift* blazar observations increased significantly, leading to the observation (and detection) of all but six blazars in the LBAS sample.

The *Swift* database currently includes 119 observations of 48 LBAS blazars that were carried out either simultaneously or within three months of the *Fermi* LBAS data taking period. We used the UVOT, XRT, and BAT data of these observations to build our SED. Some blazars were observed several times in the period that we consider in this paper; in such cases, we considered only the exposures where the source was detected at minimum and maximum intensity by the XRT instrument.

3.2.1. UVOT Data Analysis

Swift observations are normally carried out so that UVOT produces a series of images in each of the lenticular filters (*V*, *B*, *U*, *UVW1*, *UVM2*, and *UVW2*). The photometry analysis of all our sources was performed using the standard UVOT software distributed within the HEAsoft 6.3.2 package and the calibration included in the latest release of the "Calibration Database." Counts were extracted from an aperture of 5″ radius for all filters and converted to fluxes using the standard zero points (Poole et al. 2008). The fluxes were then de-reddened using the appropriate values of $E(B-V)$ for each source taken from Schlegel et al. (1998) with $A_\lambda/E(B-V)$ ratios calculated for UVOT filters using the mean interstellar extinction curve from Fitzpatrick (1999). No variability was detected within single exposures in any filter.

The results of our analysis are summarized in Table 3 where Column 1 gives the source name, Column 2 gives the observation date, and the other columns report the magnitudes in the five UVOT filters with the own errors.

3.2.2. XRT Data Analysis

The XRT is usually operated in the auto state mode which automatically adjusts the readout mode of the CCD detector to the source brightness, in an attempt to avoid pile-up (see Burrows et al. 2005; Hill et al. 2004, for details of the XRT observing modes). Given the low count rate of our blazars most of the data were collected using the most sensitive photon counting (PC) mode while the windowed timing (WT) mode was used for bright sources with shorter exposures.

The XRT data were processed with the XRTDAS software package (ver. 2.4.1) developed at the ASDC and distributed by the NASA High Energy Astrophysics Archive Research Center (HEASARC) within the HEASoft package (ver. 6.6.1). Event files were calibrated and cleaned with standard filtering criteria with the *xrtpipeline* task using the latest calibration files available in the *Swift* CALDB. Events in the energy range 0.3–10 keV with grades 0–12 (PC mode) and 0–2 (WT mode) were used for the analysis.

Events for the spectral analysis were selected within a circle of 20 pixel (∼47″) radius, which encloses about 90% of the PSF at 1.5 keV (Moretti et al. 2005), centered on the source position. For PC mode data, when the source count rate is above ∼0.5 counts s^{-1} data are significantly affected by pile-up in the inner part of the point spread function (PSF). For such cases, after comparing the observed PSF profile with the analytical model derived by Moretti et al. (2005), we removed pile-up effects by excluding events detected within up to 6 pixels from the source position, and used an outer radius of 30 pixels. The value of the inner radius was evaluated individually for each observation affected by pile-up, depending on the observed count rate.

Ancillary response files were generated with the *xrtmkarf* task applying corrections for the PSF losses and CCD defects. Source spectra were binned to ensure a minimum of 20 counts per bin to utilize the χ^2 minimization fitting technique.

We fitted the spectra adopting an absorbed power-law model with photon index Γ_x. When deviations from a single power-law model were found, we adopted a log-parabolic law of the form $F(E) = K E^{(-a+b\cdot\log(E))}$ (Massaro et al. 2004) which has been shown to fit well the X-ray spectrum of blazars (e.g., Giommi et al. 2005; Tramacere et al. 2009). This spectral model is described by only two parameters: a, the photon index at 1 keV, and b, the curvature of the parabola. For both models the amount of hydrogen-equivalent column density (N_H) was fixed to the Galactic value along the line of sight (Kalberla et al. 2005).

The results of the spectral fits are shown in Table 4 where Column 1 gives the source name, Column 2 gives the observation date, Column 3 gives the net XRT exposure time, Column 4 gives the 2–10 keV X-ray flux, Column 5 gives the best-fit photon index Γ_x or the log parabola parameter a when a simple power-law model was not a good representation of the data, Column 6 gives the best-fit curvature parameter b, Column 7 gives the number of degrees of freedom, and Column 8 gives the value of the reduced χ^2.

3.2.3. BAT Hard X-ray Data Analysis

We used survey data from the BAT on board *Swift* to produce 15–200 keV spectra of the blazars presented in this analysis.

Table 3
Results of *Swift* UVOT Analysis

Source Name (1)	Observation Date (2)	V_{mag}[a] (3)	B_{mag}[a] (4)	U_{mag}[a] (5)	UVW1[a] (6)	UVM2[a] (7)	UVW2[a] (8)
J0033.5−1921	2008 Nov 11	16.30 ± 0.04	16.59 ± 0.03	15.67 ± 0.03	15.59 ± 0.04	15.44 ± 0.04	15.60 ± 0.03
...	2008 Nov 15	16.33 ± 0.07	16.60 ± 0.05	15.65 ± 0.04	15.59 ± 0.05	15.44 ± 0.05	15.57 ± 0.04
J0050.5−0928	2008 Jun 4	...	...	...	...	...	15.074 ± 0.033
J0137.1+4751	2008 Nov 18	15.43 ± 0.03	15.84 ± 0.02	15.14 ± 0.04	15.38 ± 0.05	15.18 ± 0.04	15.43 ± 0.04
...	2008 Feb 11	...	...	...	...	...	...
...	2007 Nov 22	15.007 ± 0.02	15.554 ± 0.019	14.966 ± 0.023	13.354 ± 0.033	15.632 ± 0.036	15.772 ± 0.033
J0210.7−5100	2005 May 4	...	...	...	...	...	...
...	2008 Dec 26	17.553 ± 0.062	17.037 ± 0.039	18.059 ± 0.046	16.784 ± 0.043	16.679 ± 0.044	17.058 ± 0.039
...	2008 Oct 23	16.849 ± 0.046	16.490 ± 0.034	17.419 ± 0.036	16.511 ± 0.042	16.378 ± 0.043	16.726 ± 0.036
...	2008 Aug 31	17.465 ± 0.102	18.035 ± 0.076	16.993 ± 0.06	16.875 ± 0.062	16.756 ± 0.068	17.073 ± 0.054
J0222.6+4302	2008 Oct 3	14.07 ± 0.03	14.37 ± 0.02	13.46 ± 0.02	13.43 ± 0.03	13.25 ± 0.04	13.40 ± 0.03
...	2008 Oct 5	14.312 ± 0.019	14.640 ± 0.018	13.790 ± 0.022	13.88 ± 0.032	13.901 ± 0.032	13.989 ± 0.031
...	2005 Nov 27	15.054 ± 0.014	15.528 ± 0.016	14.757 ± 0.02	14.939 ± 0.03	15.03 ± 0.03	15.149 ± 0.03
...	2005 Jun 29	14.798 ± 0.018	15.298 ± 0.018	14.476 ± 0.021	14.638 ± 0.031	14.723 ± 0.032	14.840 ± 0.031
J0229.3−3640	2008 Nov 7	18.41 ± 0.20	19.12 ± 0.17	18.19 ± 0.12	18.47 ± 0.13	18.58 ± 0.16	19.38 ± 0.17
J0238.4+2855	2007 Jul 16	...	...	...	17.928 ± 0.046	...	...
...	2007 Jul 6	...	...	...	...	...	18.671 ± 0.042
...	2008 Sep 6	...	...	...	17.21 ± 0.05	...	...
J0238.6+1636	2007 Feb 19	...	...	16.336 ± 0.041	16.514 ± 0.048	16.679 ± 0.053	17.024 ± 0.047
...	2005 Jul 7	19.284 ± 0.258	19.876 ± 0.22	19.712 ± 0.225	19.326 ± 0.11	19.816 ± 0.120	19.863 ± 0.093
...	2008 Oct 22	16.089 ± 0.057	16.964 ± 0.051	17.021 ± 0.072	17.198 ± 0.079	17.306 ± 0.094	17.552 ± 0.070
...	2008 Sep 2	16.75 ± 0.10	17.69 ± 0.10	17.90 ± 0.15	17.88 ± 0.14	18.32 ± 0.21	18.31 ± 0.13
J0349.8−2102	2008 Oct 15	18.17(UL)	19.22(UL)	18.73(UL)	18.88(UL)	18.40(UL)	19.14(UL)
J0423.1−0112	2007 Mar 24	17.501 ± 0.061	18.024 ± 0.045	17.327 ± 0.041	17.456 ± 0.048	17.659 ± 0.053	17.908 ± 0.045
...	2008 Jan 3	...	17.185 ± 0.022	...	...	...	...
...	2008 Aug 6	17.237 ± 0.129	17.955 ± 0.099	17.151 ± 0.081	17.218 ± 0.08	17.249 ± 0.085	17.607 ± 0.074
J0428.7-3755	2008 Oct 27	...	...	...	...	19.97 ± 0.97	...
J0449.7−4348	2008 Dec 19	14.33 ± 0.02	14.57 ± 0.02	13.62 ± 0.02	13.49 ± 0.03	13.32 ± 0.03	13.39 ± 0.03
...	2009 Jan 12	14.251 ± 0.014	14.534 ± 0.016	13.591 ± 0.02	13.476 ± 0.03	13.324 ± 0.03	13.425 ± 0.03
J0457.1-2325	2008 Nov 16						
...	2008 Oct 26	17.011 ± 0.055	17.507 ± 0.035	16.770 ± 0.035	16.907 ± 0.044	16.983 ± 0.058	17.457 ± 0.044
J0507.9+6739	2009 Jan 4	16.15 ± 0.04	16.43 ± 0.04	15.47 ± 0.04	15.35 ± 0.04	15.19 ± 0.04	15.29 ± 0.04
J0516.2−6200	2009 Jan 11	17.441 ± 0.035	17.881 ± 0.026	17.171 ± 0.028	17.359 ± 0.037	17.413 ± 0.041	17.778 ± 0.037
...	2009 Jan 15	17.668 ± 0.068	18.053 ± 0.046	17.262 ± 0.043	17.546 ± 0.054	17.586 ± 0.060	18.058 ± 0.052
J0531.0+1331	2006 Apr 12	18.20 (UL)	19.03 (UL)	18.57(UL)	18.63(UL)	...	...
	2006 Mar 28	18.57(UL)	19.08(UL)	18.90(UL)	18.94(UL)	...	...
	2008 Sep 23	17.99(UL)	18.71(UL)	18.22(UL)	18.16(UL)	17.63(UL)	18.21 (UL)
	2008 Oct 22	...	...	...	19.51(UL)	...	...
J0538.8−4403	2005 Jan 26	...	...	...	...	...	...
...	2005 Nov 17	16.443 ± 0.018	16.152 ± 0.022	16.912 ± 0.019	...	...	...
...	2008 Oct 12	...	16.585 ± 0.033	15.904 ± 0.034	16.039 ± 0.042	...	16.292 ± 0.040
...	2008 Oct 7	15.867 ± 0.027	16.315 ± 0.022	15.967 ± 0.027	15.730 ± 0.034	15.757 ± 0.036	15.967 ± 0.033
J0712.9+5034	2009 Jan 21	16.070 ± 0.043	17.516 ± 0.032	16.794 ± 0.033	16.983 ± 0.041	17.100 ± 0.045	17.176 ± 0.038
J0722.0+7120	2005 Apr 4	14.024 ± 0.013	14.490 ± 0.016	13.553 ± 0.020	12.522 ± 0.03	13.479 ± 0.03	12.618 ± 0.03
...	2008 Dec 13	13.403 ± 0.017	13.793 ± 0.017	13.048 ± 0.021	13.126 ± 0.031	13.104 ± 0.032	13.216 ± 0.031
...	2008 Apr 28	12.853 ± 0.014	13.233 ± 0.016	12.340 ± 0.020	12.334 ± 0.030	12.277 ± 0.030	12.384 ± 0.030
...	2007 Nov 3	13.114 ± 0.014	13.500 ± 0.016	12.650 ± 0.020	12.685 ± 0.03	12.777 ± 0.03	12.660 ± 0.031
J0730.4−1142	2007 Dec 8	...	...	...	...	18.77(UL)	...
...	2007 Sep 27	...	...	...	...	...	...
...	2008 Dec 6	...	...	...	...	17.62 ± 0.29	...
...	2008 Nov 8	...				16.70-13.85	17.99−17.96
J0855.4+2009	2007 Nov 7	...	...	...	13.91 ± 0.03	...	...
	2005 May 20	15.00 ± 0.02			14.65 ± 0.06		
	2008 Oct 30	14.821 ± 0.041	15.299 ± 0.024	14.677 ± 0.024	14.863 ± 0.033	...	...
	2008 Nov 8	14.82 ± 0.03	15.31 ± 0.02	14.65 ± 0.03	14.82 ± 0.04	...	15.00 ± 0.04
J0921.2+4437	2009 Jan 18	17.307 ± 0.048	17.692 ± 0.034	17.033 ± 0.035	18.365 ± 0.065	20.948 ± 0.312	19.976 ± 0.110
J1015.2+4927	2007 Sep 24	...	...	...	...	...	...
	2005 Jun 26	...	...	...	...	...	...
	2008 May 2	15.312 ± 0.042	15.574 ± 0.029	14.631 ± 0.030	14.402 ± 0.037	14.233 ± 0.040	14.312 ± 0.034
	2008 May 8	15.288 ± 0.03	15.533 ± 0.023	14.589 ± 0.025	14.423 ± 0.033	14.233 ± 0.035	14.310 ± 0.032
J1057.8+0138	2007 Apr 9	...	...	...	...	...	...
	2008 Jul 19	...	...	...	...	16.980 ± 0.048	...
J1058.9+5629	2009 Jan 21	15.424 ± 0.016	...	14.884 ± 0.021	...	...	14.767 ± 0.031
J1104.5+3811	2005 Mar 1	...	...	...	...	...	...
	2006 Jun 24	...	...	...	...	...	...

Table 3
(Continued)

Source Name (1)	Observation Date (2)	V_{mag}[a] (3)	B_{mag}[a] (4)	U_{mag}[a] (5)	UVW1[a] (6)	UVM2[a] (7)	UVW2[a] (8)
	2008 Jun 12	...	...	...	11.91 ± 0.03	11.64 ± 0.03	11.75 ± 0.03
	2008 Dec 5	...	...	...	12.54 ± 0.03	12.25 ± 0.03	12.35 ± 0.03
J1159.2+2912	2007 Nov 24	...	...	17.277 ± 0.022	...	...	...
	2007 Jun 27	...	...	...	...	16.24 ± 0.04	...
	2008 Nov 21	...	...	...	16.849 ± 0.032	...	...
J1221.7+2814	2008 Jun 7	14.677 ± 0.017	15.050 ± 0.017	14.214 ± 0.021	14.169 ± 0.030	14.011 ± 0.021	14.169 ± 0.030
...	2008 Dec 28	15.081 ± 0.030	15.481 ± 0.022	14.961 ± 0.025	14.703 ± 0.034	14.902 ± 0.085	14.876 ± 0.033
...	2008 Mar 28	14.649 ± 0.024	15.031 ± 0.020	14.200± 0.023	14.155 ±0.033	14.072 ± 0.033	14.201 ± 0.032
...	2005 Jul 14	15.283 ± 0.033	15.681 ± 0.032	14.870 ± 0.029	14.957 ± 0.038	14.874 ± 0.039	14.957 ± 0.033
J1229.1+0202	2005 Nov 24	...	...	...	...	...	...
	2006 May 26	...	...	...	...	...	...
	2008 May 10	12.67 ± 0.02	...	11.82 ± 0.02	11.34 ± 0.03	11.14 ± 0.03	...
	2008 Jun 1	12.65 ± 0.02	12.89 ± 0.02	11.82 ± 0.02	11.38 ± 0.03	11.15 ± 0.03	11.15 ± 0.03
J1248.7+5811	2008 May 15	15.6477 ± 0.032	16.0047 ± 0.025	15.1167 ± 0.027	15.0747 ± 0.035	14.9637 ± 0.036	15.1067 ± 0.033
J1256.1−0547	2007 Jan 13	13.421 ± 0.014	13.927 ± 0.016	13.196 ± 0.02	13.349 ± 0.030	13.397 ± 0.031	13.559 ± 0.030
...	2007 Jul 12	14.671 ± 0.018	15.173 ± 0.018	14.428 ± 0.022	14.601 ± 0.032	14.608 ± 0.032	14.795 ± 0.031
...	2008 Aug 20	16.381 ± 0.065	16.680 ± 0.04	15.868 ± 0.036	15.886 ± 0.042	15.835 ± 0.066	15.956 ± 0.037
...	2008 Aug 18	16.597 ± 0.084	17.104 ± 0.058	16.148 ± 0.044	16.244 ± 0.049	16.107 ± 0.052	16.252 ± 0.041
J1310.6+3220	2007 Aug 1	16.781 ± 0.044	17.277 ± 0.033	16.491 ± 0.033	16.623 ± 0.037	16.667 ± 0.045	16.937 ± 0.038
...	2007 Apr 2	17.417 ± 0.048	16.949 ± 0.064	16.594 ± 0.044	16.649 ± 0.050	16.661 ± 0.057	16.949 ± 0.046
...	2008 May 12	...	...	...	...	17.335 ± 0.036	...
...	2008 Aug 20	...	...	...	...	16.715 ± 0.034	...
J1457.6−3538	2008 Jan 1	...	...	...	...	18.432 ± 0.042	...
...	2008 Sep 7	16.807 ± 0.093	17.588 ± 0.061	16.789 ± 0.053	17.159 ± 0.065	17.584 ± 0.152	18.138 ± 0.079
J1504.4+1030	2007 Jan 1	18.14 ± 0.10	18.61 ± 0.07	17.70 ± 0.05	18.20 ± 0.06	...	...
	2007 Feb 2	18.66 ± 0.00	19.53 ± 0.34	18.25 ± 0.17	18.53 ± 0.18	...	...
	2008 Aug 8	16.54 ± 0.03	16.95 ± 0.02	16.21 ± 0.03	16.42 ± 0.04	16.43 ± 0.04	16.63 ± 0.03
	2008 Aug 20	...	...	...	...	...	...
J1512.7−0905	2009 Jan 16	...	...	15.84 ± 0.04	15.90 ± 0.05	15.65 ± 0.04	15.76 ± 0.05
J1522.2+3143	2008 Nov 12	19.776 ± 0.403	20.173 ± 0.272	18.975 ± 0.142	19.499 ± 0.153	20.061 ± 0.042	21.174 ± 0.305
J1543.1+6130	2009 Jan 18	16.465 ± 0.043	16.741 ± 0.029	15.929 ± 0.030	15.963 ± 0.038	15.901 ± 0.039	16.023 ± 0.035
...	2009 Jan 20	16.332 ± 0.031	16.723 ± 0.024	15.804 ± 0.025	15.810 ± 0.034	15.769 ± 0.035	15.879 ± 0.032
J1653.9+3946	2008 May 12	...	...	...	...	...	...
J1719.3+1746	2009 Jan 8	17.764 ± 0.099	18.101 ± 0.055	17.291 ± 0.046	17.390 ± 0.048	17.378 ± 0.056	17.610 ± 0.046
J1751.5+0935	2008 Jan 24	...	...	...	16.40 ± 0.06	...	...
J1849.4+6706	2006 Jun 11	17.715 ± 0.059	18.150 ± 0.045	17.483 ± 0.043	17.544 ± 0.045	...	...
...	2007 Jan 23	17.492 ± 0.139	17.830 ± 0.082	17.120 ± 0.075	17.230 ± 0.080	...	...
...	2008 Aug 4	...	...	...	16.141 ± 0.035	...	...
J2000.2+6506	2006 May 23	14.982 ± 0.019	15.493 ± 0.045	14.720 ± 0.022	14.921 ± 0.032	15.031 ± 0.033	15.011 ± 0.034
...	2006 Jun 22	...	...	...	...	...	15.389 ± 0.037
...	2008 Oct 13	15.085 ± 0.033	15.564 ± 0.026	14.728 ± 0.028	14.969 ± 0.038	15.050 ± 0.044	15.060 ± 0.035
...	2008 Oct 31	15.076 ± 0.034	15.587 ± 0.027	14.952 ± 0.030	15.211 ± 0.041	15.346 ± 0.047	15.450 ± 0.038
J2143.2+1741	2007 Apr 23	...	...	...	...	15.169 ± 0.033	15.130 ± 0.030
	2008 Jan 1	...	...	...	...	...	...
...	2009 Jan 15	...	...	...	...	15.007 ± 0.031	...
J2158.8−3014	2006 Aug 1	...	...	...	...	...	...
...	2006 Apr 30	13.023 ± 0.013	13.349 ± 0.016	12.445 ± 0.020	12.341 ± 0.03	12.259 ± 0.030	12.387 ± 0.03
...	2008 Sep 5	13.077 ± 0.017	13.364 ± 0.017	12.367 ± 0.020	12.206 ± 0.03	12.09 ± 0.031	12.178 ± 0.03
...	2008 Oct 17	13.441 ± 0.018	13.747 ± 0.017	12.787 ± 0.021	12.691 ± 0.031	12.566 ± 0.031	12.667 ± 0.03
J2202.4+4217	2008 Sep 4	13.80 ± 0.04	14.33 ± 0.04	13.60 ± 0.04	13.74 ± 0.04	13.78 ± 0.05	13.96 ± 0.04
J2254.0+1609							
J2327.7+0947	2008 Jun 3	...	...	17.748 ± 0.028	...	...	...
J2345.5−1559	2009 Jan 10	18.494 ± 0.128	18.598 ± 0.062	17.923 ± 0.053	17.786 ± 0.047	17.664 ± 0.052	17.780 ± 0.039

Note. [a] All magnitudes are corrected for Galactic extintion.

In order to do so, we used three years of survey data (see Ajello et al. 2009, for details) and extracted the spectra of those blazars that are significantly detected in the 15–55 keV band. Because of the very long integration time these data are not simultaneous with our *Fermi* data.

Only 15 blazars, among those presented here, were detected by BAT at a significance $\geqslant 4\ \sigma$. The spectral extraction is performed as described in Ajello et al. (2008) and the background-subtracted spectra represent the average emissions of the sources within the time spanned by the BAT survey.

3.2.4. Swift Observations of LBAS Blazars Carried out Before 2008 May or After 2009 January

The *Swift* database includes a number of observations of LBAS blazars that were carried out outside the period that we consider useful to build our quasi-simultaneous SED. These

Table 4
Results of *Swift* XRT Data Analysis

Source Name (1)	Observation Date (2)	XRT Exposure (s) (3)	X-ray Flux (2–10 keV)[a] (4)	Γ_x/a[b] (5)	b (6)	dof (7)	$\chi^2_{\rm reduced}$ (8)
J0033.5−1921	2008 Nov 11	2946.2	2.32×10^{-12}	2.29 ± 0.07	−0.15 ± 0.27	23	1.03
...	2008 Nov 15	3939.8	1.86×10^{-12}	2.4 ± 0.06	−0.29 ± 0.24	31	1.3
J0050.5−0928	2008 Jun 4	865	1.27×10^{-12}	...	...	...	...
J0137.1+4751	2008 Nov 18	6520	2.4×10^{-12}	1.38 ± 0.11	...	11	1.51
...	2008 Feb 11	4674	1.7×10^{-12}	1.59 ± 0.16	...	4	1.6
...	2007 Nov 22	4643	2.2×10^{-12}	1.58 ± 0.01	...	11	1.19
J0210.7−5100	2005 May 4	2102	1.89×10^{-12}	1.85 ± 0.12	...	6	0.53
...	2008 Dec 26	4595	1.28×10^{-12}	1.66 ± 0.13	...	7	1.93
...	2008 Oct 23	3688	2.67×10^{-12}	1.64 ± 0.08	...	14	1.13
...	2008 Aug 31	1475	1.39×10^{-12}	...	...	...	...
J0222.6+4302	2008 Oct 3	4525	4.16×10^{-12}	2.67 ± 0.39	...	72	0.90
...	2008 Oct 5	2704	2.09×10^{-12}	2.80 ± 0.70	...	29	0.87
...	2005 Nov 27	52415	2.15×10^{-12}	2.3 ± 0.02	...	215	1.022
...	2005 Jun 29	5541	1.74×10^{-12}	2.34 ± 0.07	...	25	1.44
J0229.3−3640	2008 Nov 7	12428	9.64×10^{-13}	1.03 ± 0.15	−0.52 ± 0.27	12	0.54
J0238.4+2855	2007 Jul 16	7269	1.6×10^{-12}	1.56 ± 0.10	...	10	0.64
...	2007 Jun 6	2901	1.57×10^{-12}	1.55 ± 0.14	...	4	1.06
...	2008 Sep 6	2417	1.44×10^{-12}	...	...	...	...
J0238.6+1636	2007 Feb 19	1936	1.026×10^{-11}	1.14 ± 0.08	...	15	0.58
...	2005 Jul 7	12042	1.64×10^{-12}	1.44 ± 0.07	...	20	1.46
...	2008 Oct 22	1198	2.24×10^{-11}	1.93 ± 0.06	...	26	1.74
...	2008 Sep 2	6944	3.8×10^{-12}	1.37 ± 0.06	...	26	1.7
J0349.8−2102	2008 Oct 15	1557	7.8×10^{-13}	...	...	...	...
J0423.1−0112	2007 Mar 23	7044	2.54×10^{-12}	1.71 ± 0.06	...	25	0.93
...	2008 Jan 3	5536	2.39×10^{-12}	1.57 ± 0.08	...	14	0.45
...	2008 Aug 6	1306	4.65×10^{-12}	1.56 ± 0.13	...	5	0.75
J0428.7−3755	2008 Oct 27	4483	7.07×10^{-13}	1.89 ± 0.14	...	5	0.96
J0449.7−4348	2008 Dec 19	7981	7.6×10^{-12}	2.53 ± 0.02	−0.36 ± 0.06	165	1.07
...	2009 Jan 12	10967	2.53×10^{-12}	2.85 ± 0.03	−0.38 ± 0.09	122	1.14
J0457.1−2325	2008 Nov 16	3034	6.33×10^{-13}	...	...	...	...
...	2008 Oct 25	3970.1	7.92×10^{-13}	1.9 ± 0.3	...	4	0.01
J0507.9+6739	2009 Jan 4	28998	4.41×10^{-11}	2.29 ± 0.03	...	388	1.06
J0516.2−6200	2009 Jan 11	14024	7.49×10^{-13}	1.70 ± 0.09	...	11	1.06
...	2009 Jan 15	4343	5.18×10^{-13}-	...	...	...	
J0531.0+1331	2006 Apr 12	2572	5.3×10^{-12}	1.4 ± 0.1	...	11	1.84
...	2006 Mar 28	3332	3.3×10^{-12}	1.33 ± 0.15	...	7	0.67
...	2008 Sep 23	1982	4.42×10^{-12}	1.14 ± 0.17	...	4	0.59
...	2008 Oct 22	2471	2.9×10^{-12}	...	...	...	...
J0538.8−4403	2005 Jan 26	7438	8.30×10^{-12}	1.78 ± 0.03	...	97	1.04
	2005 Nov 17	6431	2.15×10^{-12}	1.84 ± 0.06	...	22	1.00
	2008 Oct 12	1413	4.72×10^{-12}	1.69 ± 0.09	...	9	0.31
	2008 Oct 7	5054	4.33×10^{-12}	1.70 ± 0.05	...	32	0.98
J0712.9+5034	2009 Jan 21	6234	3.67×10^{-13}	...	...	...	...
J0722.0+7120	2005 Apr 4	18887	1.06×10^{-12}	2.78 ± 0.05	...	48	0.95
	2008 Dec 13	1442	2.8×10^{-12}	2.45 ± 0.13	...	8	0.96
	2008 Apr 28	2002	9.7×10^{-12}	2.7 ± 0.06	...	44	1.25
	2007 Nov 3	2802	6.82×10^{-12}	2.6 ± 0.05	...	38	0.85
J0730.4−1142	2007 Dec 8	6028	1.45×10^{-12}	1.55 ± 0.14	...	6	0.45
	2007 Sep 27	1918	1.07×10^{-12}	...	...	...	...
	2008 Dec 6	6234	1.47×10^{-12}	1.72 ± 0.13	...	8	1.29
	2008 Nov 8	1989	1.35×10^{-12}	...	...	...	...
J0855.4+2009	2007 Nov 7	1854	5.29×10^{-12}	1.35 ± 0.12	...	8	0.75
	2005 May 20	3793	2.12×10^{-12}	1.62 ± 0.09	...	10	0.96
	2008 Oct 30	952	8.75×10^{-12}	1.47 ± 0.12	...	8	1.00
	2008 Nov 8	994	7.02×10^{-12}	1.43 ± 0.12	...	5	0.84
J0921.2+4437	2009 Jan 18	6534	2.86×10^{-12}	1.63 ± 0.06	...	22	1.04
J1015.2+4927	2007 Sep 24	2870	7.02×10^{-12}	2.47 ± 0.04	−0.49 ± 0.13	73	0.81
	2005 Jun 26	9962	9.67×10^{-12}	2.26 ± 0.02	−0.09 ± 0.06	152	0.95
	2008 May 2	862	2.31×10^{-11}	2.14 ± 0.06	−0.53 ± 0.20	32	0.94
	2008 May 8	1769	1.01×10^{-11}	2.47 ± 0.04	−0.28 ± 0.15	50	0.92
J1057.8+0138	2007 Apr 9	662	2.52×10^{-12}	...	...	...	...
	2008 Jul 19	1064	1.76×10^{-12}	...	...	...	...
J1058.9+5629	2009 Jan 21	3817	1.36×10^{-12}	2.48 ± 0.05	−0.47 ± 0.20	40	0.79
J1104.5+3811	2006 Jun 24	12944	1.10×10^{-09}	1.86 ± 0.02	−0.092 ± 0.004	802	3.6
	2005 Mar 1	7197	4.14×10^{-11}	2.60 ± 0.007	−0.099 ± 0.002	320	1.35

Table 4
(Continued)

Source Name (1)	Observation Date (2)	XRT Exposure (s) (3)	X-ray Flux (2–10 keV)[a] (4)	Γ_x/a[b] (5)	b (6)	dof (7)	$\chi^2_{\rm reduced}$ (8)
	2008 Jun 12	4980	2.62×10^{-09}	1.74 ± 0.004	−0.202 ± 0.009	652	2.31
	2008 Dec 5	5361	2.69×10^{-10}	2.190 ± 0.005	−0.349 ± 0.013	496	1.88
J1159.2+2912	2007 Nov 24	8268	1.29×10^{-12}	1.71 ± 0.08	...	14	1.22
	2007 Jun 27	2767	8.09×10^{-13}	1.63 ± 0.25	...	...	...
	2008 Nov 21	6968	1.86×10^{-12}	1.50 ± 0.09	...	11	1.09
1221.7+2814	2008 Jun 7	9087	5.14×10^{-12}	2.04 ± 0.03	−0.19 ± 0.08	130	1.03
...	2008 Dec 28	1548	7.4×10^{-12}	...	...	...	...
...	2008 Mar 28	1705	1.9×10^{-12}	2.4 ± 0.08	−0.47 ± 0.29	17	0.94
...	2005 Jul 14	1191	7.7×10^{-13}	...	...	...	...
J1229.1+0202	2005 Nov 24	4008	1.33×10^{-10}	1.68 ± 0.02	...	143	1.31
	2006 May 26	2349	9.9×10^{-11}	1.68 ± 0.03	...	80	1.13
	2008 May 10	2249	1.02×10^{-10}	1.57 ± 0.02	...	115	1.14
	2008 Jun 1	1313	7.9×10^{-11}	1.64 ± 0.03	...	62	0.86
J1248.7+5811	2008 May 15	2283	6.19×10^{-13}	2.42 ± 0.13	−0.18 ± 0.49	5	1.18
J1256.1−0547	2008 Aug 18	1777	4.51×10^{-12}	1.8 ± 0.09	...	12	0.75
...	2008 Aug 20	1922	6.05×10^{-12}	1.8 ± 0.07	...	22	1.34
...	2007 Jul 12	4839	8.04×10^{-12}	1.5 ± 0.04	...	51	0.87
...	2007 Jan 12	9700	1.27×10^{-11}	1.6 ± 0.02	...	150	1.36
J1310.6+3220	2007 Aug 1	4913	2.15×10^{-12}	1.61 ± 0.09	...	11	0.55
	2007 Apr 2	2150	2.52×10^{-12}	1.61 ± 0.11	...	6	0.36
	2008 May 12	5342	1.62×10^{-12}	1.66 ± 0.08	...	12	1.13
	2008 Aug 20	4773	2.51×10^{-12}	1.56 ± 0.08	...	13	0.82
J1457.6−3538	2008 Jan 1	9128	5.65×10^{-13}	1.96 ± 0.13	...	7	1.30
	2008 Sep 7	1596	1.80×10^{-12}	...	...	...	...
J1504.4+1030	2007 Jan 1	10351	9.28×10^{-13}	1.45 ± 0.1	...	9	0.65
	2007 Feb 2	5074	8.93×10^{-13}	...	...	...	...
	2008 Aug 8	12466	1.66×10^{-12}	1.53 ± 0.06	...	27	1.22
	2008 Aug 20	1912	9.94×10^{-13}	...	...	...	...
J1512.7−0905	2009 Jan 16	7124	5.47×10^{-12}	1.40 ± 0.10	...	31	0.57
J1522.2+3143	2008 Nov 12	5884	2.68×10^{-13}	...	...	...	...
J1543.1+6130	2009 Jan 18	3367	2.06×10^{-13}	...	...	...	...
	2009 Jan 20	6875	1.68×10^{-13}	...	...	...	...
J1653.9+3946	2008 May 12	1160	1.40×10^{-10}	2.07 ± 0.07	...	186	0.95
J1719.3+1746	2009 Jan 8	4808	9.28×10^{-13}	1.70 ± 0.12	...	5	1.42
J1751.5+0935	2009 Jan 24	983	2.71×10^{-12}	1.97 ± 0.51	...	8	0.8
J1849.4+6706	2006 Jun 11	8897	1.17×10^{-12}	1.70 ± 0.09	...	14	1.50
	2007 Jan 23	1171	1.96×10^{-11}	...	...	...	...
	2008 Aug 4	2206	2.48×10^{-12}	1.47 ± 0.16	...	4	0.63
J2000.2+6506	2006 May 23	5372	2.14×10^{-10}	1.91 ± 0.01	−0.26 ± 0.02	488	1.31
	2006 Jun 22	438	9.90×10^{-11}	1.89 ± 0.09	−0.44 ± 0.20	28	1.48
	2008 Oct 13	1204	1.22×10^{-10}	1.82 ± 0.05	−0.31 ± 0.11	72	1.15
	2008 Oct 31	1084	5.61×10^{-11}	2.16 ± 0.05	−0.25 ± 0.13	63	0.73
J2143.2+1741	2007 Apr 23	7180	1.16×10^{-12}	1.79 ± 0.10	...	12	1.38
	2009 Jan 15	5913	1.60×10^{-12}	1.74 ± 0.10	...	12	2.14
J2158.8−3014	2006 Aug 1	1541	4.47×10^{-11}	2.55 ± 0.03	−0.37 ± 0.10	96	1.07
...	2006 Apr 30	8217	1.5×10^{-11}	2.52 ± 0.02	−2.38 ± 0.06	149	1.00
...	2008 Sep 5	1091	5.59×10^{-11}	2.42 ± 0.01	−0.10 ± 0.05	185	1.35
...	2008 Oct 17	1229	1.83×10^{-11}	2.35 ± 0.05	−0.18 ± 0.14	41	1.03
J2202.4+4217	2008 Sep 4	5787	1.01×10^{-11}	2.05 ± 0.15	...	61	1.11
J2254.0+1609	2008 Aug 8	4216	3.32×10^{-11}	1.55 ± 0.03	...	91	1.30
J2327.7+0947	2008 Jun 3	4486	2.80×10^{-12}	1.13 ± 0.09	...	9	0.78
J2345.5−1559	2009 Jan 10	9503	2.41×10^{-13}	...	...	...	...

Notes.
[a] When the photon statistics were too poor to allow a reliable best fit, the flux was estimated converting the observed count rate assuming a power-law model with photon index of 1.9 and low energy absorption due to Galactic N_H.
[b] This column gives the power-law photon index γ when a simple power-law model could be used. In the case where the log parabola model was used this column gives the a parameter which represents the photon index at 1 keV.

measurements are particularly important for the case of blazars that have never previously been observed by any X-ray astronomy satellite and were below the detection threshold of the *ROSAT* all-sky survey. When these *Swift* observations have been analyzed and published by other authors we use the flux intensities reported in the literature, with particular reference to the latest online version of the BZcat catalog.[94] For the cases where

[94] http://www.asdc.asi.it/bzcat

the *Swift* results have not yet appeared in the literature we list in Column 8 of Table 1 the X-ray fluxes estimated from the standard pipeline processing that is run at ASDC on all *Swift* XRT data shortly after they are added to the archive. This ASDC processing makes use of the "xrtpipeline" task of the XRTDAS package that is run after applying very tight data screening criteria, e.g., a CCD temperature lower than −50°C (instead of the standard limit of −47°C), thus ensuring a very effective background reduction. The calibrated and cleaned PC mode event files produced are then analyzed with the XIMAGE package v.4.4.1 and the point sources present in each XRT field are searched using the XIMAGE detection algorithm. For each source the net counts are corrected to account for CCD defects, effective exposure and vignetting using the exposure maps and a PSF correction. The count rates are finally converted into fluxes in the 0.1–2.4 keV band assuming a power-law spectral model with energy slope of 0.9 and low-energy absorption due to Galactic N_H.

3.3. Other Multi-frequency Data

In order to improve the quality of our SED we complemented the *Fermi* and *Swift* quasi-simultaneous data with other multi-frequency flux measurements obtained from a number of ongoing programs from ground- and space-based observatories. In the following sections, we describe each program and the corresponding data analysis.

3.3.1. Effelsberg Radio Observations

Quasi-simultaneous radio data for 25 sources of the first *Fermi* bright source catalog were obtained within a *Fermi* -related monthly broadband monitoring program including the Effelsberg 100 m radio telescope of the MPIfR (F-GAMMA project; Fuhrmann et al. 2007; Angelakis et al. 2009). From this program, radio spectra covering the frequency range 2.6–42 GHz were selected to be within the time period 2008 August 4 to 2008 October 31, i.e., quasi-simultaneous to the *Fermi* and *Swift* observations presented in Sections 3.1 and 3.2.

The Effelsberg observations were conducted with cross-scans in azimuth/elevation with the number of sub-scans matching the source brightness at the given frequencies. The individual spectra were measured quasi-simultaneously within $\leqslant$40 minutes rapidly switching between the various secondary focus receivers. The data reduction was done applying standard procedures and post-observational corrections including (1) opacity correction, (2) pointing off-set correction, (3) gain correction, and (4) sensitivity correction (see Fuhrmann et al. 2008; Angelakis et al. 2009, for details). The sensitivity correction was done with reference to standard calibrators (e.g., 3C 286) and the measured antenna temperatures were linked to the absolute flux-density scale (Baars et al. 1977; Ott et al. 1994). The precision ranges between $\lesssim$1% to a few percent.

The results are reported in Table 5 where Column 1 gives the source name, Column 2 gives the observation date, Column 3 gives the frequency, and Column 4 gives the flux density in units of Jansky.

3.3.2. OVRO Radio Data

Quasi-simultaneous 15 GHz observations of 24 *Fermi* LBAS sources were made using the Owens Valley Radio Observatory (OVRO) 40 m telescope. These observations were made as part of an ongoing *Fermi* -LAT blazar monitoring program. In this program, all 1158 CGRaBS blazars north of decl. −20° have

Table 5
Effelsberg Radio Data

Source Name 0FGL (1)	Observation Date (2)	Frequency (GHz) (3)	Flux Density (Jy) (4)
J0222.6+4302	2008 Aug 8	4.85	1.434
	2008 Aug 8	8.35	1.247
	2008 Aug 8	10.45	1.159
	2008 Aug 8	14.60	1.087
	2008 Aug 8	23.05	1.086
J0238.4+2855	2008 Sep 17	2.64	3.221
	2008 Sep 17	4.85	3.609
	2008 Sep 17	8.35	3.614
	2008 Sep 17	10.45	3.495
	2008 Sep 17	14.60	3.331
	2008 Sep 17	23.05	3.124
	2008 Sep 17	42.00	2.960
J0238.6+1636	2008 Sep 17	2.64	2.174
	2008 Sep 17	4.85	3.235
	2008 Sep 17	8.35	4.102
	2008 Sep 17	10.45	4.295
	2008 Sep 17	14.60	4.450
	2008 Sep 17	23.05	4.569
	2008 Sep 17	42.00	5.030
J0423.1-0112	2008 Oct 18	2.64	2.851
	2008 Oct 18	4.85	3.397
	2008 Oct 18	8.35	3.726
	2008 Oct 18	10.45	3.930
	2008 Oct 18	14.60	4.154
	2008 Oct 18	23.05	4.057
	2008 Oct 18	32.00	3.769
	2008 Oct 18	42.00	3.748
J0507.9+6739	2008 Nov 9	2.64	0.038
	2008 Nov 9	4.85	0.035
	2008 Nov 9	8.35	0.030
J0531.0+1331	2008 Dec 6	2.64	3.945
	2008 Dec 6	4.85	4.052
	2008 Dec 6	8.35	3.646
	2008 Dec 6	10.45	3.459
	2008 Dec 6	14.60	3.188
	2008 Dec 6	23.05	2.553
	2008 Dec 6	32.00	2.281
J0722.0+7120	2008 Sep 17	2.64	1.000
	2008 Sep 17	4.85	1.110
	2008 Sep 17	8.35	1.408
	2008 Sep 17	10.45	1.544
	2008 Sep 17	14.60	1.744
	2008 Sep 17	23.05	1.928
	2008 Sep 17	42.00	1.833
J0855.4+2009	2008 Oct 18	2.64	1.373
	2008 Oct 18	4.85	1.786
	2008 Oct 18	8.35	2.333
	2008 Oct 18	10.45	2.531
	2008 Oct 18	14.60	2.815
	2008 Oct 18	23.05	3.072
	2008 Oct 18	32.00	2.828
	2008 Oct 18	42.00	2.740
J1104.5+3811	2008 Sep 18	4.85	0.600
	2008 Sep 18	8.35	0.499
	2008 Sep 18	10.45	0.468
	2008 Sep 18	14.60	0.428
J1159.2+2912	2008 Sep 18	4.85	1.705
	2008 Sep 18	8.35	2.386
	2008 Sep 18	10.45	2.663
	2008 Sep 18	14.60	2.831
	2008 Sep 18	42.00	2.661
J1221.7+2814	2008 Oct 18	4.85	0.486
	2008 Oct 18	8.35	0.458
	2008 Oct 18	10.45	0.440

Table 5
(Continued)

Source Name 0FGL (1)	Observation Date (2)	Frequency (GHz) (3)	Flux Density (Jy) (4)
	2008 Oct 18	14.60	0.412
J1229.1+0202	2008 Sep 18	4.85	38.557
	2008 Sep 18	8.35	35.822
	2008 Sep 18	10.45	34.332
	2008 Sep 18	14.60	30.181
	2008 Sep 18	23.05	24.733
	2008 Sep 18	42.00	18.097
J1256.1-0547	2008 Oct 18	2.64	10.136
	2008 Oct 18	4.85	11.535
	2008 Oct 18	8.35	13.974
	2008 Oct 18	10.45	15.263
	2008 Oct 18	14.60	16.560
	2008 Oct 18	23.05	18.230
	2008 Oct 18	32.00	16.895
	2008 Oct 18	42.00	15.287
J1310.6+3220	2008 Sep 16	2.64	0.863
	2008 Sep 16	4.85	0.915
	2008 Sep 16	8.35	1.272
	2008 Sep 16	10.45	1.472
	2008 Sep 16	14.60	1.796
	2008 Sep 16	23.05	2.218
	2008 Sep 16	42.00	2.648
J1504.3+1030	2008 Sep 16	2.64	1.468
	2008 Sep 16	4.85	1.391
	2008 Sep 16	8.35	1.486
	2008 Sep 16	10.45	1.582
	2008 Sep 16	14.60	1.815
	2008 Sep 16	23.05	2.007
	2008 Sep 16	42.00	2.231
J1512.7-0905	2009 Jan 25	2.64	2.346
	2009 Jan 25	4.85	2.371
	2009 Jan 25	8.35	2.206
	2009 Jan 25	10.45	2.164
	2009 Jan 25	14.60	2.065
J1653.9+3946	2008 Aug 23	2.64	1.536
	2008 Aug 23	4.85	1.465
	2008 Aug 23	8.35	1.345
	2008 Aug 23	10.45	1.278
	2008 Aug 23	14.60	1.195
	2008 Aug 23	23.05	1.056
J1751.5+0935	2009 Jan 25	2.64	2.999
	2009 Jan 25	4.85	3.880
	2009 Jan 25	8.35	5.093
	2009 Jan 25	10.45	5.298
	2009 Jan 25	14.60	6.265
	2009 Jan 25	23.05	6.722
J1719.1+1744	2009 Jan 25	2.64	0.670
	2009 Jan 25	4.85	0.675
	2009 Jan 25	8.35	0.626
	2009 Jan 25	10.45	0.599
	2009 Jan 25	14.60	0.599
	2009 Jan 25	32.00	0.516
J2000.2+6506	2008 Nov 8	4.85	0.239
	2008 Nov 8	8.35	0.230
	2008 Nov 8	10.45	0.217
J2143.2+1741	2009 Jan 25	2.64	0.639
	2009 Jan 25	4.85	0.683
	2009 Jan 25	10.45	0.701
	2009 Jan 25	14.60	0.740
	2009 Jan 25	32.00	0.801
J2158.8-3014	2008 Sep 16	2.64	0.619
	2008 Sep 16	4.85	0.592
	2008 Sep 16	8.35	0.560
	2008 Sep 16	10.45	0.560

Table 5
(Continued)

Source Name 0FGL (1)	Observation Date (2)	Frequency (GHz) (3)	Flux Density (Jy) (4)
	2008 Sep 16	14.60	0.548
	2008 Sep 16	32.00	0.715
J2202.4+4217	2008 Sep 16	2.64	2.117
	2008 Sep 16	4.85	2.365
	2008 Sep 16	8.35	2.461
	2008 Sep 16	10.45	2.440
	2008 Sep 16	14.60	2.446
	2008 Sep 16	23.05	2.373
	2008 Sep 16	42.00	2.393
J2254.0+1609	2008 Sep 17	2.64	11.304
	2008 Sep 17	4.85	9.493
	2008 Sep 17	8.35	10.595
	2008 Sep 17	10.45	11.945
	2008 Sep 17	14.60	14.837
	2008 Sep 17	23.05	20.564
	2008 Sep 17	42.00	29.924

been observed approximately twice per week or more frequently since 2007 June (Healey et al. 2008).

The OVRO flux densities are measured in a single 3 GHz wide band centered at 15 GHz. Observations were performed using azimuth double switching as described in Readhead et al. (1989), which removes much atmospheric and ground interference. The relative uncertainties in flux density result from a 5 mJy typical thermal uncertainty in quadrature with a 1.6% systematic uncertainty. The absolute flux density scale is calibrated to about 5% via observations of the steady calibrator 3C 286, using the (Baars et al. 1977) model.

For each source, the maximum and minimum observed 15 GHz flux densities during the 2008 August 4 to October 31 period were included in the quasi-simultaneous SED. The included OVRO 40 m observations are summarized in Table 6. Column 1 lists the 0FGL source name. Columns 2 and 4 list the dates of the observed maximum and minimum. Columns 3 and 5 list the measured maximum and flux density in Jansky, including the 5% absolute calibration uncertainty in the quoted error.

3.3.3. RATAN-600 1–22 GHz Radio Observations

Among the 48 objects for which we present *Swift* and *Fermi* simultaneous SED, 32 were observed between 2008 September 10 and October 3 with the 600 m ring radio telescope RATAN-600 (Korolkov & Parijskij 1979) of the Special Astrophysical Observatory, Russian Academy of Sciences, located in Zelenchukskaya, Russia. These observations, which produced 1–22 GHz instantaneous radio spectra, are part of a long-term program (e.g., Kovalev et al. 2002) to monitor continuum spectra of active galactic nuclei (AGNs) with a strong parsec-scale component of radio emission. The current list contains a complete sample of more than 600 AGNs with decl. $\delta > -30^{\circ}$ and correlated VLBI flux density greater than 400 mJy selected from Kovalev et al. (2007).

Broadband radio continuum spectra were measured quasi-simultaneously in a transit mode at six different bands with the following central frequencies (and frequency bands): 0.95 GHz (0.03 GHz), 2.3 GHz (0.25 GHz), 4.8 GHz (0.6 GHz), 7.7 GHz (1.0 GHz), 11.2 GHz (1.4 GHz), and 21.7 GHz (2.5 GHz). Each source was observed in the upper culmination with an unmoved

Table 6
OVRO Radio Data (15 GHz)

Name 0FGL (1)	Date of Max. (2)	Max. Flux Density (Jy) (3)	Date of Min. (4)	Min. Flux Density (Jy) (5)
J0050.5-0928	2008 Oct 23	1.079 ± 0.057	2008 Dec 19	1.761 ± 0.092
J0137.1+4751	2008 Aug 16	3.05 ± 0.16	2008 Oct 24	3.73 ± 0.20
J0222.6+4302	2008 Dec 20	0.861 ± 0.045	2008 Aug 16	1.070 ± 0.056
J0238.4+2855	2008 Oct 22	2.99 ± 0.16	2008 Aug 30	3.34 ± 0.18
J0423.1-0112	2008 Nov 4	3.90 ± 0.20	2008 Nov 19	4.40 ± 0.23
J0531.0+1331	2008 Aug 23	2.87 ± 0.15	2008 Nov 5	3.26 ± 0.17
J0722.0+7120	2008 Dec 6	1.511 ± 0.079	2008 Aug 26	3.16 ± 0.17
J0855.4+2009	2008 Nov 12	2.37 ± 0.13	2008 Dec 24	3.21 ± 0.17
J1015.2+4927	2008 Aug 8	0.246 ± 0.014	2008 Dec 6	0.286 ± 0.016
J1057.8+0138	2008 Oct 29	4.26 ± 0.22	2008 Dec 23	4.63 ± 0.24
J1104.5+3811	2008 Aug 27	0.424 ± 0.023	2008 Dec 14	0.477 ± 0.025
J1159.2+2912	2008 Aug 14	2.48 ± 0.13	2008 Dec 12	3.52 ± 0.19
J1221.7+2814	2008 Aug 20	0.382 ± 0.021	2008 Aug 18	0.425 ± 0.023
J1229.1+0202	2008 Dec 14	27.3 ± 1.4	2008 Aug 11	30.6 ± 1.6
J1248.7+5811	2008 Aug 22	0.149 ± 0.010	2008 Nov 7	0.172 ± 0.010
J1256.1-0547	2008 Oct 18	16.48 ± 0.87	2008 Aug 12	17.82 ± 0.94
J1310.6+3220	2008 Aug 10	1.613 ± 0.085	2008 Nov 16	1.819 ± 0.095
J1504.4+1030	2008 Sep 2	1.667 ± 0.088	2008 Dec 23	2.40 ± 0.13
J1522.2+3143	2008 Nov 10	0.333 ± 0.018	2008 Aug 14	0.502 ± 0.027
J1653.9+3946	2008 Nov 11	1.002 ± 0.053	2008 Dec 5	1.185 ± 0.062
J1751.5+0935	2008 Aug 8	4.48 ± 0.24	2008 Dec 21	7.12 ± 0.37
J1849.4+6706	2008 Nov 2	1.705 ± 0.090	2008 Dec 13	2.41 ± 0.13
J2000.2+6506	2008 Aug 18	0.167 ± 0.010	2008 Dec 5	0.226 ± 0.012
J2327.3+0947	2008 Aug 9	1.494 ± 0.078	2008 Dec 17	1.95 ± 0.10

antenna due to the Earth rotation collecting a multi-frequency source scan within several minutes. Details on the method of observation, data processing, and amplitude calibration are described in Kovalev et al. (1999). Presented data were collected using the Southern ring sector with the Flat reflector of RATAN-600. The spectrum of every object was measured, typically, 3 times during the observing set. Averaged flux density spectra used in our SED are presented in Table 7 where Column 1 gives the source name, Column 2 gives the frequency of observations, and Column 3 gives the radio flux density in units of Jansky. During recent years, the radio frequency interference became stronger at the two lowest frequency bands, 1 and 2.3 GHz. This results in higher measurement errors and sometimes even loss of data, especially at the lowest frequency band. Bad weather conditions resulted in elevated errors at 22 GHz in a few cases.

3.3.4. Radio, mm, NIR and Optical Data from the GASP–WEBT Collaboration

The GLAST–*AGILE* Support Program (GASP) originated from the Whole Earth Blazar Telescope[95] (WEBT; see e.g., Villata et al. 2007; Raiteri et al. 2008a)) and started its operation in 2007 September (see Villata et al. 2008), with the aim of performing long-term optical-to-radio monitoring of 28 γ-loud blazars, to compare the low-energy flux behavior with the behavior observed at γ-ray energies.

In the period considered in this work, the GASP carried out ∼3000 optical (*R* band) observations of 19 LBAS blazars, while ∼700 near-IR (*JHK*, Campo Imperatore), and ∼600 microwave (230 and 345 GHz, SMA) and radio data (5–43 GHz, Medicina, Noto, UMRAO) observations were taken on the same sources.

The optical and near-IR magnitudes were de-reddened by assuming the Galactic extinction in the *B* band from Schlegel et al. (1998) and deriving the extinction in the other bands according to Cardelli et al. (1989). The conversion to fluxes was performed adopting the zero-mag fluxes by Bessel et al. (1998).

In the SED plots, we report the average, maximum, and minimum values at each observed frequency in the period 2008 August 4–October 31.[96]

Table 8 reports the plotted values directly as $\log(\nu F_\nu)$: the average, maximum, and minimum values are shown in Columns 3, 4, and 5, respectively. Column 6 displays the number of data available in the period. When the number of data available is reported as "0" this indicates that the data given in the table and shown in the SED plots are not strictly inside the period (this happens for ON 231 and 3C 279 in the optical, and for 3C 273 in both the optical and near-IR, because of solar conjunction), but come from immediately outside and, due to the smoothness of the light curve, they can represent the state in between. Note that Columns 4 and 5 report the error bar extremes instead of maximum and minimum values.

The optical data of Mkn 421 have been cleaned for the contribution of the host galaxy, according to Nilsso et al. (2007). As for PKS 0235+164, we corrected the fluxes for both the photometric contribution from the southern AGN and the additional extinction due to the intervening DLA system, according to Raiteri et al. (2005); see also Raiteri et al. (2008b).

3.3.5. Mid-infrared VISIR Observations

The MIR observations were carried out from 2006 to 2008 using VISIR (Lagage et al. 2004), the ESO/VLT mid-infrared imager and spectrograph, composed of an imager and a long-slit spectrometer covering several filters in *N* and *Q* bands and

[95] http://www.oato.inaf.it/blazars/webt/

[96] Average flux densities were calculated on the one day binned data sets, to avoid giving too much weight to the days with denser sampling.

Table 7
RATAN-600 Flux Density Measurements in 2008 September 10–October 3

Source Name 0FGL (1)	Central Frequency (GHz) (2)	Flux Density (Jy) (3)
0FGL J0050.5−0928	21.7	0.98 ± 0.06
	11.2	1.10 ± 0.04
	7.7	1.09 ± 0.03
	4.8	0.97 ± 0.01
	2.3	0.95 ± 0.11
	1.0	0.91 ± 0.15
0FGL J0137.1+4751	21.7	3.43 ± 0.06
	11.2	3.75 ± 0.07
	7.7	3.61 ± 0.06
	4.8	3.00 ± 0.04
	2.3	2.06 ± 0.31
0FGL J0222.6+4302	21.7	0.88 ± 0.06
	11.2	1.13 ± 0.02
	7.7	1.32 ± 0.03
	4.8	1.19 ± 0.08
0FGL J0238.4+2855	21.7	2.69 ± 0.17
	11.2	3.10 ± 0.07
	7.7	3.44 ± 0.07
	4.8	3.50 ± 0.05
	2.3	3.51 ± 0.27
	1.0	3.75 ± 0.55
0FGL J0238.6+1636	21.7	3.76 ± 0.20
	11.2	3.96 ± 0.14
	7.7	3.70 ± 0.11
	4.8	3.11 ± 0.12
	2.3	2.09 ± 0.10
	1.0	1.15 ± 0.19
0FGL J0349.8−2102	21.7	1.10 ± 0.10
	11.2	0.79 ± 0.03
	7.7	0.82 ± 0.07
	4.8	0.61 ± 0.11
	2.3	0.28 ± 0.11
	1.0	0.18 ± 0.03
0FGL J0423.1−0112	21.7	3.34 ± 0.05
	11.2	3.52 ± 0.04
	7.7	3.44 ± 0.07
	4.8	3.42 ± 0.08
	2.3	2.63 ± 0.20
0FGL J0457.1−2325	21.7	1.98 ± 0.09
	11.2	3.02 ± 0.16
	7.7	3.02 ± 0.20
	4.8	2.28 ± 0.11
	2.3	1.61 ± 0.27
	1.0	1.50 ± 0.15
0FGL J0531.0+1331	21.7	2.37 ± 0.06
	11.2	2.95 ± 0.04
	7.7	3.10 ± 0.04
	4.8	3.33 ± 0.08
	2.3	2.99 ± 0.11
	1.0	1.35 ± 0.19
0FGL J0722.0+7120	21.7	2.26 ± 0.16
	11.2	2.23 ± 0.06
	7.7	1.81 ± 0.07
	4.8	1.43 ± 0.10
	2.3	1.05 ± 0.18
0FGL J0730.4−1142	21.7	5.99 ± 0.23
	11.2	7.55 ± 0.12
	7.7	7.33 ± 0.09
	4.8	5.64 ± 0.35
	2.3	3.54 ± 0.25
0FGL J0855.4+2009	21.7	2.81 ± 0.19
	11.2	2.73 ± 0.04
	7.7	2.45 ± 0.04
	4.8	1.88 ± 0.17
	2.3	1.38 ± 0.16
0FGL J0921.2+4437	21.7	2.12 ± 0.10
	11.2	1.69 ± 0.03
	7.7	1.31 ± 0.24
	4.8	1.13 ± 0.13
	2.3	1.22 ± 0.17
0FGL J1057.8+0138	21.7	3.67 ± 0.13
	11.2	3.98 ± 0.24
	7.7	3.56 ± 0.05
	4.8	3.07 ± 0.09
	2.3	2.89 ± 0.13
0FGL J1104.5+3811	21.7	0.53 ± 0.14
	11.2	0.43 ± 0.03
	7.7	0.47 ± 0.04
	4.8	0.49 ± 0.11
	2.3	0.44 ± 0.13
	1.0	0.38 ± 0.06
0FGL J1159.2+2912	21.7	2.93 ± 0.15
	11.2	2.85 ± 0.10
	7.7	2.45 ± 0.04
	4.8	1.66 ± 0.05
	2.3	1.02 ± 0.14
0FGL J1229.1+0202	21.7	21.35 ± 0.61
	11.2	32.51 ± 0.43
	7.7	36.40 ± 0.37
	4.8	37.81 ± 2.06
	2.3	48.10 ± 0.97
0FGL J1256.1−0547	21.7	16.44 ± 0.62
	11.2	15.09 ± 1.36
	7.7	14.72 ± 0.28
	4.8	11.76 ± 1.52
	2.3	10.31 ± 0.58
0FGL J1310.6+3220	21.7	1.68 ± 0.28
	11.2	1.49 ± 0.01
	7.7	1.25 ± 0.07
	4.8	0.91 ± 0.04
	2.3	0.81 ± 0.13
0FGL J1457.6−3538	21.7	1.18 ± 0.18
	11.2	1.20 ± 0.04
	7.7	1.25 ± 0.03
	4.8	0.89 ± 0.03
	2.3	0.83 ± 0.08
	1.0	1.02 ± 0.15
0FGL J1504.3+1030	21.7	1.75 ± 0.14
	11.2	1.54 ± 0.05
	7.7	1.41 ± 0.03
	4.8	1.35 ± 0.07
	2.3	1.52 ± 0.10
	1.0	1.54 ± 0.10
0FGL J1512.7−0905	21.7	2.75 ± 0.26
	11.2	3.34 ± 0.25
	7.7	3.23 ± 0.12
	4.8	2.58 ± 0.21
	2.3	2.16 ± 0.19
0FGL J1522.2+3143	21.7	0.34 ± 0.07
	11.2	0.47 ± 0.02
	7.7	0.55 ± 0.05
	4.8	0.53 ± 0.03
	2.3	0.65 ± 0.12
0FGL J1543.1+6130	11.2	0.11 ± 0.02
	7.7	0.09 ± 0.04
	4.8	0.06 ± 0.03
0FGL J1653.9+3946	21.7	0.94 ± 0.09
	11.2	1.31 ± 0.03

Table 7
(Continued)

Table 7
(Continued)

Source Name 0FGL (1)	Central Frequency (GHz) (2)	Flux Density (Jy) (3)
	7.7	1.44 ± 0.04
	4.8	1.29 ± 0.15
	2.3	1.54 ± 0.14
	1.0	1.89 ± 0.23
0FGL J1719.3+1746	21.7	0.56 ± 0.13
	11.2	0.60 ± 0.05
	7.7	0.66 ± 0.02
	4.8	0.62 ± 0.04
	2.3	0.55 ± 0.10
	1.0	0.37 ± 0.09
0FGL J1751.5+0935	21.7	5.36 ± 0.23
	11.2	4.34 ± 0.07
	7.7	3.06 ± 0.10
	4.8	1.94 ± 0.08
	2.3	1.46 ± 0.12
0FGL J2000.2+6506	11.2	0.23 ± 0.03
	7.7	0.28 ± 0.02
	4.8	0.35 ± 0.07
0FGL J2143.2+1741	21.7	0.58 ± 0.09
	11.2	0.60 ± 0.02
	7.7	0.58 ± 0.02
	4.8	0.51 ± 0.04
	2.3	0.49 ± 0.08
0FGL J2158.8−3014	11.2	0.56 ± 0.03
	7.7	0.70 ± 0.04
	4.8	0.59 ± 0.03
	2.3	0.69 ± 0.06
	1.0	0.79 ± 0.20
0FGL J2202.4+4217	21.7	2.30 ± 0.11
	11.2	2.69 ± 0.03
	7.7	2.77 ± 0.03
	4.8	2.25 ± 0.07
	2.3	1.95 ± 0.12
	1.0	1.80 ± 0.22
0FGL J2254.0+1609	11.2	11.45 ± 0.10
	7.7	9.68 ± 0.06
	4.8	9.25 ± 0.13
	2.3	12.07 ± 0.10
	1.0	15.57 ± 1.05
0FGL J2327.3+0947	21.7	1.35 ± 0.10
	11.2	1.31 ± 0.06
	7.7	1.21 ± 0.08
	4.8	1.12 ± 0.07
	2.3	0.72 ± 0.06
	1.0	0.71 ± 0.09

mounted on Unit 3 of the VLT (Melipal). The standard "chopping and nodding" MIR observational technique was used to suppress the background dominating at these wavelengths. Secondary mirror-chopping was performed in the north–south direction with an amplitude of 16″ at a frequency of 0.25 Hz. Nodding technique, needed to compensate for chopping residuals, was chosen as parallel to the chopping and applied using telescope offsets of 16″. Because of the high thermal MIR background for ground-based observations, the detector integration time was set to 16 ms.

We performed broadband photometry in three filters, *PAH1* ($\lambda = 8.59 \pm 0.42\,\mu$m), *PAH2* ($\lambda = 11.25 \pm 0.59\,\mu$m), and *Q2* ($\lambda = 18.72 \pm 0.88\,\mu$m) using the small field in all bands (19.″2 × 19.″2 and 0.″075 plate scale). All the observations were bracketed with standard star observations for flux calibration

Table 8
GASP–WEBT Data

Name (1)	log (ν) (2)	log (νF_ν) (average) (3)	log (νF_ν) (max) (4)	log (νF_ν) min (5)	N_{data} (6)
J0222.6+4302	14.670	−10.446	−10.246	−10.668	521
	14.390	−10.467	−10.300	−10.638	21
	14.265	−10.477	−10.324	−10.643	21
	14.136	−10.496	−10.365	−10.661	21
	10.633	−12.394	−12.371	−12.417	2
	10.342	−12.694	−12.623	−12.778	2
	10.161	−12.850	−12.820	−12.900	3
	9.903	−13.011	−13.007	−13.017	4
J0238.6+1636	14.670	−10.554	−10.011	−11.366	619
	14.390	−10.439	−10.007	−11.145	64
	14.265	−10.401	−10.000	−11.058	62
	14.136	−10.383	−9.983	−10.990	63
	11.538	−10.997	−10.893	−11.038	7
	11.362	−11.056	−10.937	−11.188	13
	10.633	−11.640	−11.618	−11.663	2
	10.342	−12.101	−12.008	−12.220	2
	10.161	−12.204	−12.049	−12.363	22
	9.903	−12.432	−12.302	−12.614	11
	9.699	−12.725	−12.576	−12.888	8
J0423.1−0112	14.670	−11.428	−11.332	−11.486	3
	14.390	−11.307	−11.285	−11.327	6
	14.265	−11.251	−11.197	−11.296	6
	14.136	−11.162	−11.128	−11.187	6
	11.538	−11.253	−11.195	−11.346	8
	11.362	−11.294	−11.249	−11.368	16
	10.633	−11.761	−11.738	−11.785	2
	10.342	−12.079	−12.069	−12.089	2
	10.161	−12.239	−12.210	−12.281	20
	9.903	−12.496	−12.434	−12.543	8
	9.699	−12.793	−12.784	−12.803	1
J0531.0+1331	14.670	−11.646	−11.624	−11.669	2
	14.390	−11.866	−11.705	−11.997	7
	14.265	−11.861	−11.682	−12.057	7
	14.136	−11.918	−11.680	−12.115	6
	11.538	−11.468	−11.417	−11.538	6
	11.362	−11.487	−11.437	−11.552	11
	10.633	−11.887	−11.865	−11.911	2
	10.342	−12.146	−12.092	−12.207	1
	10.161	−12.357	−12.319	−12.383	12
	9.903	−12.566	−12.560	−12.571	2
	9.699	−12.744	−12.726	−12.767	3
J0722.0+7120	14.670	−10.017	−9.809	−10.240	56
	14.390	−10.038	−9.902	−10.188	16
	14.265	−10.035	−9.908	−10.181	15
	14.136	−10.012	−9.898	−10.148	15
	11.538	−11.293	−11.195	−11.421	1
	11.362	−11.228	−11.090	−11.402	6
	10.633	−11.876	−11.868	−11.883	2
	10.342	−12.237	−12.202	−12.276	2
	10.161	−12.550	−12.395	−12.669	10
	9.903	−12.920	−12.797	−13.040	7
	9.699	−13.220	−13.155	−13.328	7
J0855.4+2009	14.670	−10.379	−10.215	−10.485	13
	14.390	−10.222	−10.108	−10.293	4
	14.265	−10.166	−10.059	−10.228	4
	14.136	−10.124	−10.035	−10.177	5
	11.362	−11.216	−11.145	−11.271	6
	10.633	−11.885	−11.877	−11.892	2
	10.342	−12.188	−12.149	−12.230	2
	10.161	−12.410	−12.372	−12.446	9
	9.903	−12.707	−12.672	−12.731	4
	9.699	−13.089	−13.021	−13.170	2
J1104.5+3811	14.670	−10.100	−10.078	−10.123	2
	11.362	−12.180	−12.089	−12.296	0

Table 8
(Continued)

Name	log (ν)	log (νF_ν) (average)	log (νF_ν) (max)	log (νF_ν) min	$N_{\rm data}$
(1)	(2)	(3)	(4)	(5)	(6)
	10.161	−13.207	−13.138	−13.274	8
	9.903	−13.323	−13.148	−13.665	7
	9.699	−13.485	−13.438	−13.538	2
J1159.2+2912	11.362	−11.396	−11.373	−11.419	1
	10.633	−11.850	−11.842	−11.858	2
	10.342	−12.096	−11.972	−12.271	2
	10.161	−12.392	−12.329	−12.476	17
	9.903	−12.753	−12.697	−12.789	6
	9.699	−13.141	−13.121	−13.161	2
J1221.7+2814	14.670	−10.621	−10.604	−10.638	0
	10.633	−12.716	−12.685	−12.749	1
	10.342	−13.017	−12.881	−13.217	1
	10.161	−13.252	−13.231	−13.274	1
	9.903	−13.492	−13.423	−13.573	2
	9.699	−13.740	−13.611	−14.046	3
J1229.1+0202	14.670	−9.837	−9.828	−9.846	0
	14.390	−10.038	−10.036	−10.040	0
	14.265	−10.031	−10.029	−10.033	0
	14.136	−9.894	−9.892	−9.896	0
	11.538	−10.521	−10.408	−10.673	0
	11.362	−10.669	−10.508	−10.792	3
	10.633	−11.148	−11.129	−11.168	2
	10.342	−11.230	−11.224	−11.236	2
	10.161	−11.360	−11.340	−11.374	12
	9.903	−11.541	−11.521	−11.556	9
	9.699	−11.721	−11.719	−11.724	4
J1256.1−0547	14.670	−11.006	−10.788	−11.466	0
	11.362	−10.691	−10.663	−10.705	4
	10.633	−11.077	−11.022	−11.140	2
	10.342	−11.334	−11.307	−11.358	3
	10.161	−11.618	−11.592	−11.670	8
	9.903	−11.942	−11.927	−11.980	8
	9.699	−12.231	−12.221	−12.237	4
J1512.7−0905	14.670	−11.363	−11.245	−11.451	21
	14.390	−11.376	−11.308	−11.450	3
	14.265	−11.341	−11.269	−11.457	3
	14.136	−11.234	−11.201	−11.307	3
	11.362	−11.430	−11.404	−11.458	1
	10.633	−11.935	−11.886	−11.991	2
	10.342	−12.109	−12.080	−12.140	2
	10.161	−12.386	−12.305	−12.446	15
	9.903	−12.624	−12.595	−12.656	7
	9.699	−12.880	−12.817	−12.921	6
J1653.9+3946	14.670	−10.105	−10.085	−10.121	7
	14.390	−9.973	−9.971	−9.976	6
	14.265	−9.967	−9.952	−9.974	7
	14.136	−10.154	−10.149	−10.157	5
	11.362	−12.003	−11.967	−12.042	0
	10.633	−12.459	−12.417	−12.506	1
	10.161	−12.792	−12.775	−12.820	9
	9.903	−12.949	−12.898	−12.983	7
	9.699	−13.156	−13.116	−13.184	4
J2158.8−3014	14.670	−9.917	−9.760	−10.050	46
	10.161	−13.226	−13.173	−13.335	5
J2202.4+4217	14.670	−10.132	−9.970	−10.272	1095
	14.390	−10.066	−9.920	−10.175	39
	14.265	−10.068	−9.921	−10.174	38
	14.136	−10.108	−9.943	−10.212	34
	11.538	−11.285	−11.211	−11.357	5
	11.362	−11.374	−11.260	−11.463	8
	10.633	−11.928	−11.908	−11.950	2
	10.342	−12.162	−12.151	−12.172	2
	10.161	−12.425	−12.384	−12.488	15
	9.903	−12.659	−12.568	−12.711	12

Table 8
(Continued)

Name	log (ν)	log (νF_ν) (average)	log (νF_ν) (max)	log (νF_ν) min	$N_{\rm data}$
(1)	(2)	(3)	(4)	(5)	(6)
	9.699	−12.913	−12.820	−12.981	16
J2254.0+1609	14.670	−10.654	−10.426	−11.009	556
	14.390	−10.531	−10.259	−10.909	35
	14.265	−10.475	−10.171	−10.901	34
	14.136	−10.399	−10.207	−10.834	33
	11.538	−10.202	−10.107	−10.404	21
	11.362	−10.300	−10.206	−10.527	54
	10.633	−10.931	−10.915	−10.947	2
	10.342	−11.394	−11.373	−11.417	2
	10.161	−11.705	−11.662	−11.757	23
	9.903	−12.077	−12.048	−12.122	13
	9.699	−12.322	−12.312	−12.333	16

and PSF determination. The weather conditions were good and stable during the observations.

Raw data were reduced using the IDL reduction package (E. Pantin 2010, in preparation). The elementary images were co-added in real time to obtain chopping-corrected data, then the different nodding positions were combined to form the final image. The VISIR detector is affected by stripes randomly triggered by some abnormal high-gain pixels. A dedicated destriping method was developed to suppress them. The MIR fluxes and observation dates of all observed sources including the 1σ errors are listed in Table 9.

3.3.6. Non-simultaneous Spitzer Space Telescope Observations

The *Spitzer* is a 0.85 m class telescope launched on 2003 August 25. *Spitzer* obtains images and spectra in the spectral range between 3 and 180 μm through three instruments on board: the InfraRed Array Camera, which provides images at 3.6, 4.5, 5.8, and 8.0 μm, the Multiband Imaging Photometer for *Spitzer* (MIPS), which performs imaging photometry at 24, 70, and 160 μm, and the InfraRed Spectrograph which provides spectra over 5–38 μm in low ($R \sim 60$–127) and high ($R \sim 600$) spectral resolution mode. The *Spitzer* Science Archive includes MIPS observations of eight sources belonging to the LBAS sample, all of them performed earlier than three months from the start of the LBAS data taking period. From the *Spitzer* Archive we retrieved the post-BCD (post-basic calibrated data), that is, products generated after calibration of the individual BCD exposures. The DAOPHOT package was used for the photometric analysis, which was carried out on the post-BCD using the method of aperture photometry and subtracting the background emission. The results are reported in Table 10 where Column 1 gives the source name, Column 2 gives the observation date, Column 3 gives the log of frequency log(ν), and Column 4 gives the log of νF_ν.

3.3.7. AGILE γ-ray Data

The *AGILE* satellite, launched in 2007 April, is an Italian Space Agency (ASI) mission devoted to γ-ray astrophysics in the 30 MeV–50 GeV energy range, with simultaneous X-ray imaging in the 18–60 keV band. The *AGILE* instrument (Tavani et al. 2008, 2009) consists of the Silicon Tracker (ST), the X-ray detector SuperAGILE (SA), the CsI(Tl) Mini-Calorimeter (MCAL), and an anti-coincidence system (ACS). The combination of ST, MCAL and ACS forms the Gamma-Ray Imaging Detector (GRID).

Table 9
Mid-infrared Photometry of Blazars Obtained with the VISIR Instrument on VLT/UT3

Source Name 0FGL (1)	Observation Date (2)	UT (3)	Filter (4)	Flux (mJy) (5)	Error (mJy) (6)
J0238.6+1636	2008 Jul 6	10:08	PAH1	82.44	2.02
	2008 Jul 7	09:10	PAH1	108.02	2.03
	2008 Jul 7	09:36	PAH2	155.15	3.59
	2008 Jul 7	09:48	Q2	180.94	9.59
J0457.0−2325	2006 Dec 1	12:00	PAH2	67.7	1.8
	2006 Dec 1	12:00	Q2	73.0	5.3
J1256.1−0547	2007 Jul 15	00:48	PAH1	292.09	2.63
	2007 Jul 15	01:13	Q2	335.81	11.66
	2007 Jul 15	01:27	PAH2	300.58	3.49
	2008 Jul 7	23:16	PAH1	33.73	2.29
	2008 Jul 7	23:27	PAH2	40.91	2.22
	2008 Jul 7	23:39	Q2	106.49	8.25
J1512.7−0905	2008 Jul 6	00:54	PAH1	20.41	1.44
	2008 Jul 6	01:20	Q2	102.16	11.41
	2008 Jul 6	02:11	PAH2	37.33	3.83
J2158.8−3014	2007 Jul 15	09:03	PAH1	295.31	2.44
	2008 Jul 4	08:01	PAH1	136.70	1.86
	2008 Jul 4	08:27	Q2	190.70	12.05
	2008 Jul 4	08:51	PAH2	163.61	2.51
	2008 Jul 5	07:21	PAH1	134.01	3.25
	2008 Jul 5	07:33	Q2	180.87	13.74
	2008 Jul 5	07:48	PAH2	160.83	4.02
	2008 Jul 6	06:09	PAH2	78.89	3.17
	2008 Jul 6	06:20	Q2	93.89	7.66
	2008 Jul 6	06:35	PAH1	70.21	4.73
	2008 Jul 6	07:08	PAH1	160.47	3.31
	2008 Jul 6	07:19	PAH2	201.40	6.03
	2008 Jul 6	07:31	Q2	191.08	10.35
	2008 Jul 7	04:49	PAH1	144.39	3.51
	2008 Jul 7	05:00	PAH2	147.41	2.87
	2008 Jul 7	05:11	Q2	164.30	10.43

Table 10
MIPS (*Spitzer*) Data

Source Name (1)	Observation Date (2)	$\log(\nu)$ (3)	$\log(\nu F_\nu)$ (4)
J1653.9+3946	2004 Apr 11	13.097	−11.080
J1229.1+0202	2007 Jan 15	13.097	−10.121
	2007 Jan 15	12.632	−10.391
	2007 Jan 15	12.273	−10.680
	2007 Jul 11	13.097	−10.160
	2007 Jul 11	12.632	−10.499
J2202.4+4217	2006 Jul 22	13.097	−10.343
	2006 Jul 22	12.632	−10.503
	2006 Jul 22	12.273	−10.806
J2158.8−3014	2004 Nov 9	13.097	−10.937
	2004 Nov 9	12.632	−11.251
	2004 Nov 9	12.273	−11.492
	2004 Nov 27	13.097	−10.617
J1256.1−0547	2007 Feb 26	13.097	−10.281
	2007 Feb 26	12.632	−10.218
	2007 Feb 26	12.273	−10.535
	2007 Jul 12	13.097	−10.308
	2007 Jul 12	12.632	−10.302
J1221.7+2814	2007 Jun 6	13.097	−11.210
	2007 Jun 6	12.632	−11.494
	2007 Jun 6	12.273	−11.784
	2008 Jan 8	13.097	−11.023
	2008 Jan 8	12.632	−11.321
	2008 Jan 8	12.273	−11.506
J1159.2+2912	2005 May 14	13.097	−11.023
	2005 May 14	12.632	−11.151
	2005 May 14	12.273	−11.448
	2006 Apr 8	13.097	−10.543
	2006 Apr 8	12.632	−10.725
	2006 Apr 8	12.273	−11.162
J0722.0+7120	2006 Apr 8	13.097	−10.545
	2006 Apr 8	12.632	−10.725
	2006 Apr 8	12.273	−11.162

The γ-ray data collected by the GRID for energies greater than 100 MeV used in this paper (blue star symbols in the SED figures) are extracted from the first *AGILE* catalog of high-confidence γ-ray sources detected by *AGILE* during the first 12 months of operations, from 2007 July 9 to 2008 June 30 (Pittori et al. 2009). The first *AGILE* catalog includes only high-significance sources characterized by a prominent mean γ-ray flux above 100 MeV when integrated over the total one year exposure period.

Flare detections and determination of source peak fluxes through dedicated investigation over shorter timescales are not included in the first *AGILE* catalog. However, it should be noted that for some blazars, such as Mkn 421 (1AGL J1104+3754) ON 231/W Comae (1AGL J1222+2851), PKS 1510-089 (1AGL J1511-0908), and 3C279 (1AGL J1256-0549), the effective *AGILE* exposure over the entire time period was quite low, only a few effective days, but it included target of opportunity or previously planned observations during a flaring state of the source. In such cases the *AGILE* observed mean γ-ray flux may be close to the source peak flux values.

The differential *AGILE* flux values appearing in the SED figures at fixed energy point ($E = 300$ MeV) have been rescaled from the mean γ-ray flux above 100 MeV, obtained with a simple power-law source model with fixed spectral index −2.1.

Table 11
AGILE Mean Fluxes

Name (1)	*AGILE* Flux (10^{-8} ph cm^{-2} s^{-1}) (2)	*AGILE* Mean Exposure (10^8 cm^2 s) (3)
0FGL J0538.8−4403	43 ± 10	0.81
0FGL J0722.0+7120	69 ± 9	1.39
0FGL J1104.5+3811	42 ± 13	0.51
0FGL J1221.7+2814	38 ± 11	0.50
0FGL J1229.1+0202	24 ± 6	1.98
0FGL J1256.1−0547	65 ± 9	1.98
0FGL J0538.8−4403	43 ± 10	0.81
0FGL J1849.4+6706	20 ± 4	5.52
0FGL J2254.0+1609	200 ± 14	1.16

Table 11 reports the results where Column 1 gives the source name, Column 2 gives the *AGILE* observed flux, and Column 3 gives the mean exposure.

4. QUASI-SIMULTANEOUS RADIO TO γ-RAY SED OF 48 LBAS BLAZARS

In this section, we use the multi-frequency data described above to build quasi-simultaneous SED of 48 objects, in the usual $\log\nu$–$\log\nu\ F_\nu$ representation. These 48 sources are a sizable subset (≈45%) of LBAS that is representative of the entire sample since they were chosen only on the basis of the availability of *Swift* observations carried out between 2008

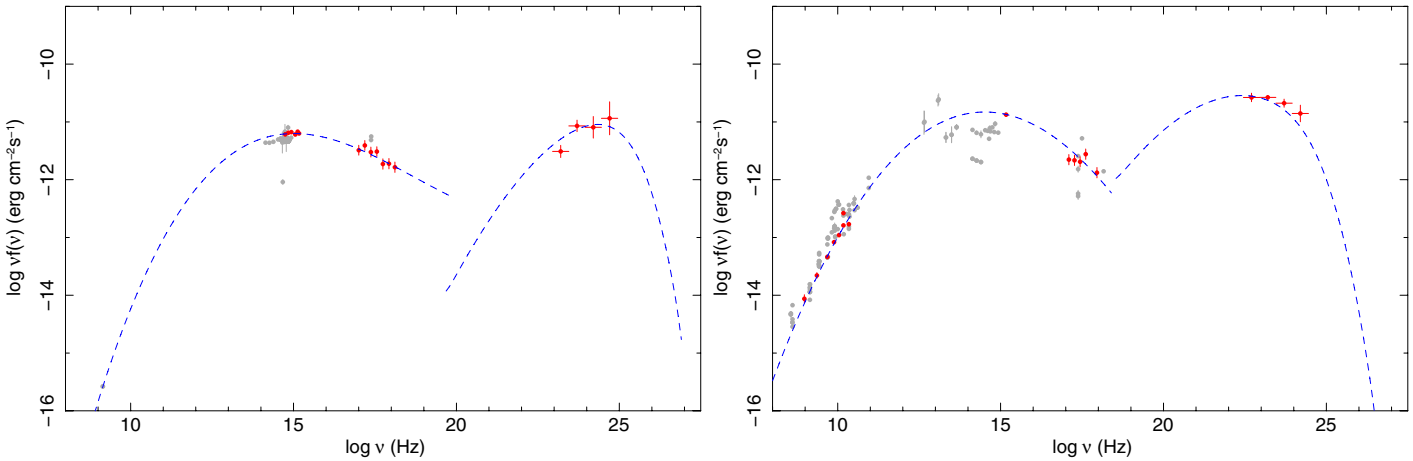

Figure 1. SED of 0FGL J0033.6−1921 = 1RXS J003334.6−192130 = SHBL J003334.2−192133 (left) and of 0FGL J0050.5−0928 = PKS0048-09 (right). The quasi-simultaneous data appear as large filled red symbols, while non-simultaneous archival measurements are shown as small open gray points. The dashed lines represent the best fits to the synchrotron and inverse Compton part of the quasi-simultaneous SED (see the text for detail).

(A color version of this figure is available in the online journal.)

Table 12
TeV Literature Data

Source Name 0FGL (1)	Period of Observations (2)	Instrument (3)	Reference (4)
J0222.6+4302	2007–2008	VERITAS	Acciari et al. 2009a
J0722.0+7120	2008 Apr 22–24	MAGIC	Teshima 2008
J1104.5+3811	2004 Nov–2005 Apr	MAGIC	Albert et al. 2007a
J1221.7+2814	2008 Jan–Apr	VERITAS	Acciari et al. 2009b
J1256.1−0547	2006 Jan–Apr	MAGIC	Errando et al. 2008
J1653.9+3946	2005 May–Jul	MAGIC	Albert et al. 2007b
J2000.2+6506	2004 Sept–Oct	MAGIC	Albert et al. 2006
J2158.8−3014	2002 Jul, Oct, 2003 Jul–Sep	HESS	Aharonian et al. 2009
J2202.4+4217	2005 Aug–Dec, 2006 Jul–Sep	MAGIC	Albert et al. 2007b

May and 2009 January (which have been scheduled largely independently of *Fermi* results) and not on brightness level or on any other condition that could influence the shape of the SED. We checked this by verifying that the distributions of redshift, optical, X-ray, and γ-ray fluxes are all consistent with being the same in the two subsamples.

We stress that there is one important difference between γ-ray and other multi-frequency data: our *Fermi* data were collected over a period of three months while all other data were collected over much shorter periods (typically less than a few hours) and are not necessarily simultaneous among themselves. This is clearly a limitation as flux and spectral variability in blazars often takes place on short timescales. Such a behavior is clearly visible, in fact, in our multi-frequency data when more than one *Swift* observation is available (see, e.g., Figures 3, 4, 6, etc.). Since our γ-ray data have been accumulated over the relatively long period of three months, they likely represent the average of different intensity states.

The SED that we have built are shown in Figures 1–24, where the *Fermi* γ-ray data and the quasi-simultaneous multi-frequency measurements appear as large filled red symbols. In all the SED, we have also included non-simultaneous multi-frequency archival measurements (small open gray points) to increase the data coverage in some energy bands and to illustrate the historical range of variability at different frequencies. Archival data points have been collected using the NED (NASA/IPAC Extragalactic Database) and ASDC online services. The TeV data have been derived from the available literature as listed in Table 12.

Figures 1–24 show that in all cases the overall shape of the SED exhibit the typical broad double hump distribution, where the first bump is attributed to synchrotron radiation and the second one is likely due to one or more components related to inverse Compton emission. The dashed lines represent the best fit to the data as described in the next section.

Our SED show that there are considerable differences in the position of the peaks of the two components and on their relative peak intensities. Large variability is also present, especially at optical/UV and X-ray frequencies. Gamma-ray variability cannot be evaluated as the *Fermi* data that we are using are averaged over the entire LBAS data taking period. The γ-ray variability of *Fermi* LBAS blazars is discussed in detail in a separate paper (Abdo et al. 2010b).

A complete description of the γ-ray spectral shape of LBAS sources is given in Abdo et al (2010a). Here we note that in most cases the *Fermi* data cannot be fit by a simple power law as significant curvature is detected. Downward (convex) curvature is often observed in sources where synchrotron peak is located at low energies (e.g., PKS0454-234, PKS1454-354 and PKS1502+106, 3C454.3 etc.) whereas very flat or even concave type curvature is exhibited by high synchrotron peaked objects (e.g., 3C66A, PKS 0447-439, 1ES 0502+675, and PG 1246+586). A possible explanation of these features is discussed in Section 7.

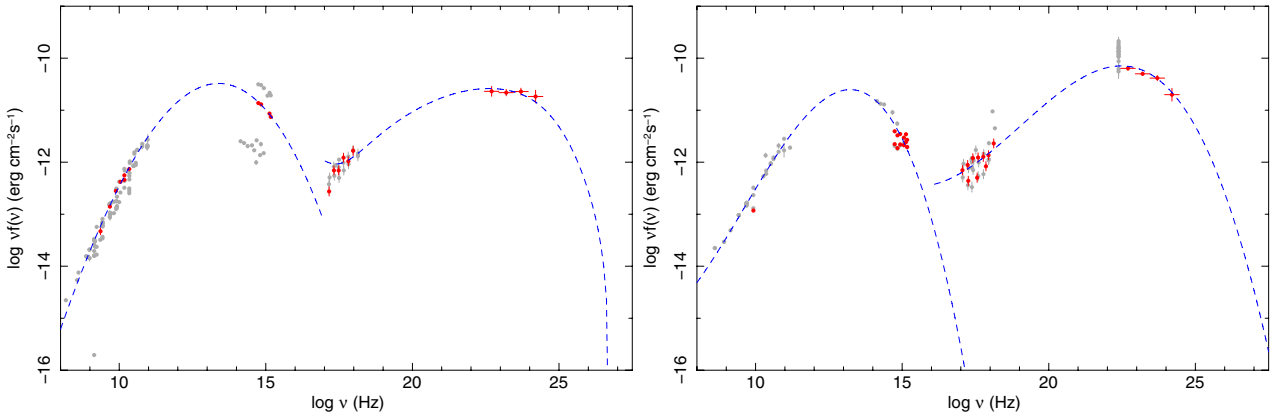

Figure 2. SED of 0FGL J0137.1+4751 = S40133+47 (left) and of 0FGL J0210.8−5100 = PKS0208-512 (right).
(A color version of this figure is available in the online journal.)

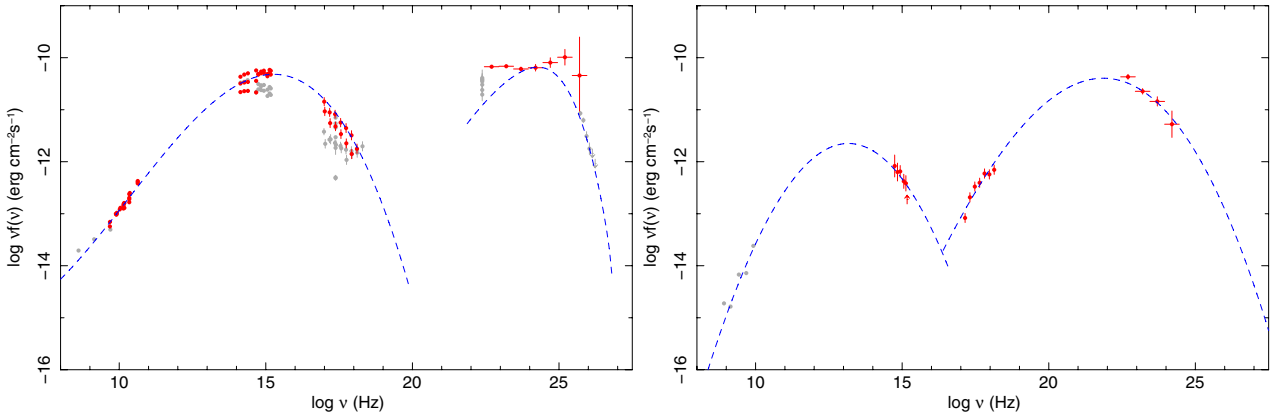

Figure 3. SED of 0FGL J0222.6+4302 = 3C 66A (left) and of 0FGL J0229.5−3640 = PKS0227-369 (right).
(A color version of this figure is available in the online journal.)

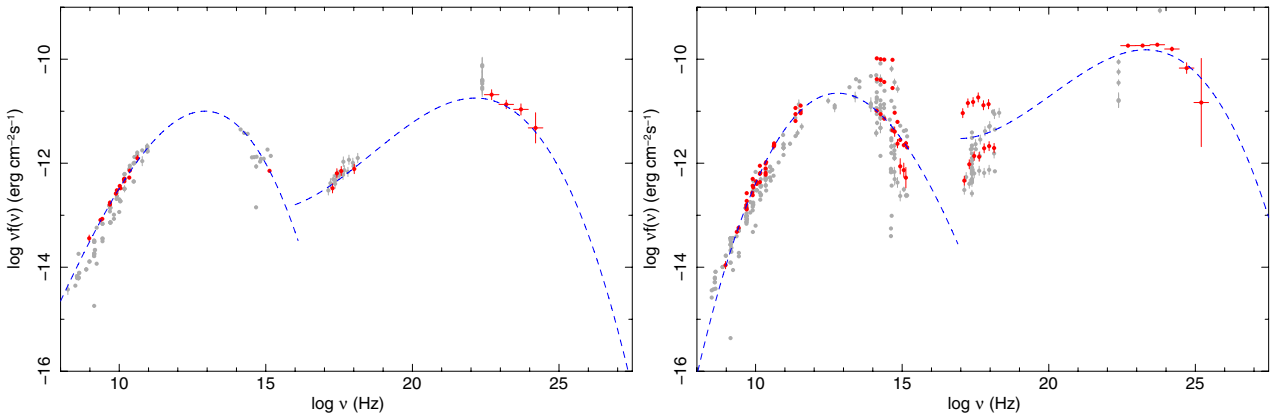

Figure 4. SED of 0FGL J0238.4+2855 = 4C28.07 (left) and of 0FGL J0238.6+1636 = PKS0235+164 (right).
(A color version of this figure is available in the online journal.)

5. BLAZAR SED OBSERVATIONAL PARAMETERS

We now estimate some key observational parameters that characterize the SED of our blazars, namely, the radio spectral index (α_r), the peak frequency and peak flux of the synchrotron component ($\nu^S_{\rm peak}$ and $\nu^S_{\rm peak}$ $F(\nu^S_{\rm peak})$), and the peak frequency and flux of the inverse Compton part of the SED ($\nu^{\rm IC}_{\rm peak}$ and $\nu^{\rm IC}_{\rm peak}$ $F(\nu^{\rm IC}_{\rm peak})$).

5.1. The Radio Spectral Slope

To estimate the blazar spectral slope (α_r, where $f_r(\nu) \propto \nu^{\alpha_r}$) in the radio/mm band we performed a linear regression of all the radio flux measurements that have been used for the SED, including the non-simultaneous ones. The set of frequencies used for the linear regression is not the same for every source but ranged from below 1 GHz up to about 100 GHz, for those sources for which microwave flux measurements are available. The distribution of the radio spectral slopes α_r obtained with this method has an average value $\langle\alpha_r\rangle = -0.03$ and a standard deviation $\sigma = 0.23$ (see Figure 25). Figure 26 shows the distribution of the radio spectral slopes between ∼1 GHz and 8.4 GHz taken from the CRATES catalog (Healey et al. 2007) for the subsample of FSRQs and BL Lac objects, respectively. The distributions shown in Figures 25 and 26 are all very

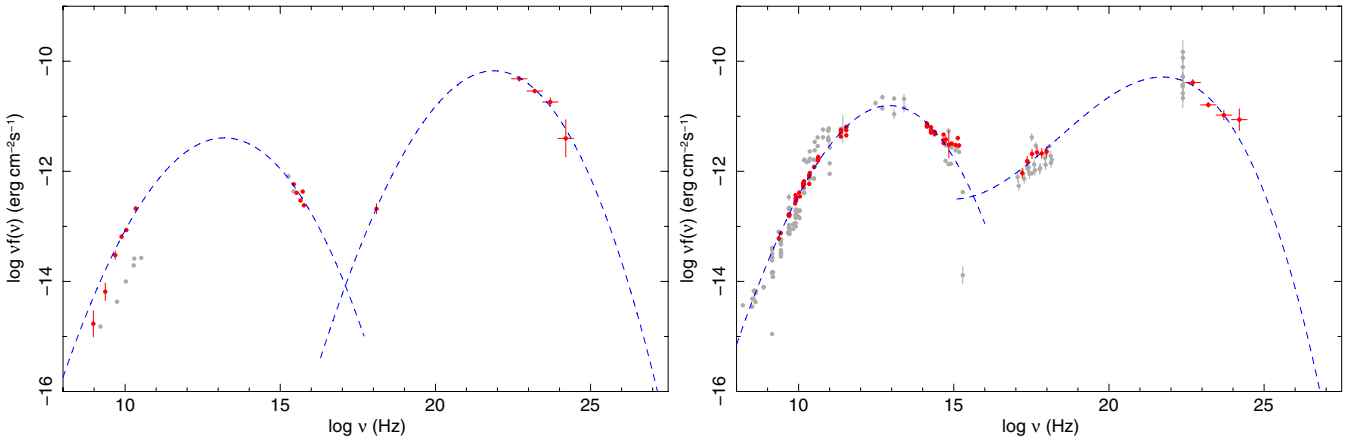

Figure 5. SED of 0FGL J0349.8−2102 = PKS 0347-211 (left) and of 0FGL J0423.1−0112 = PKS0420-01 (right).
(A color version of this figure is available in the online journal.)

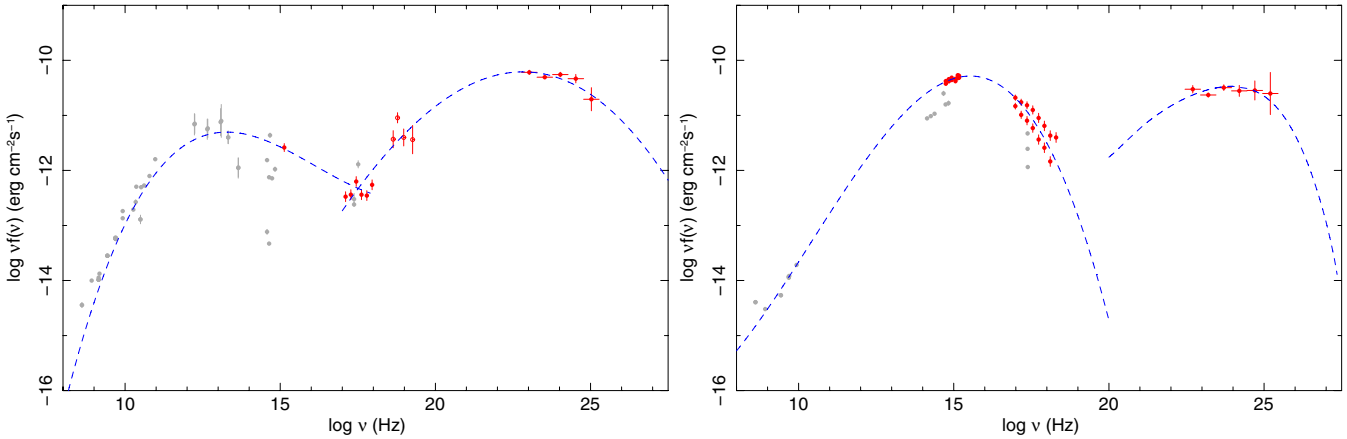

Figure 6. SED of 0FGL J0428.7−3755 = PKS0426-380 (left) and of 0FGL J0449.7−4348 = PKS0447-439 (right).
(A color version of this figure is available in the online journal.)

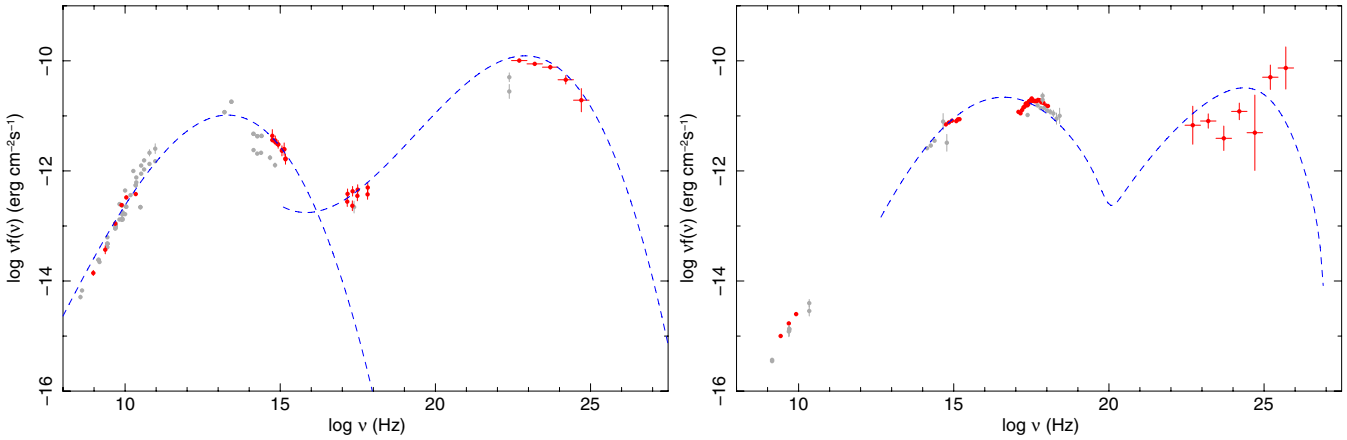

Figure 7. SED of 0FGL J0457.1−2325 = PKS0454-234 (left) and of 0FGL J0507.9+6739 = 1ES 0502+675 (right).
(A color version of this figure is available in the online journal.)

similar with an almost identical average value $\langle \alpha_r \rangle \sim 0.0$ and similar standard deviations $\sigma \sim 0.2/0.3$. In particular, for the α_r distributions of FSRQs and BL Lacs shown in Figure 26 a Kolmogorov–Smirnov test gives a probability of 0.43 that they come from the same parent population. We conclude that the radio to microwave spectral slope in our SED is quite flat ($\langle \alpha_r \rangle \sim 0$) and consistent with being the same in all blazar types.

5.2. *The α_{ox}–α_{ro} Plane*

The α_{ox}–α_{ro} plot of the LBAS sample is shown in Figure 27 which also includes all blazars in the BZCat catalog for which we have radio, optical, and X-ray measurements (small red dots). Note that *Fermi* FSRQs (filled circles), like all FSRQs discovered in any other energy band, are exclusively located along the top-left/bottom-right band, whereas BL Lacs

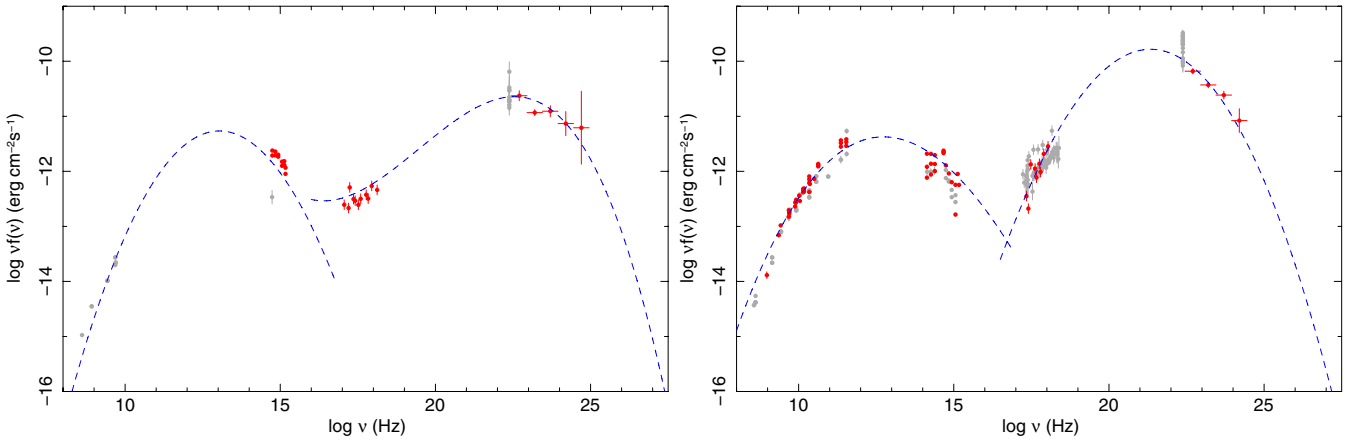

Figure 8. SED of 0FGL J0516.2−6200 = MC4 0516-621 (left) and of 0FGL J0531.0+1331 = PKS 0528+134 (right).
(A color version of this figure is available in the online journal.)

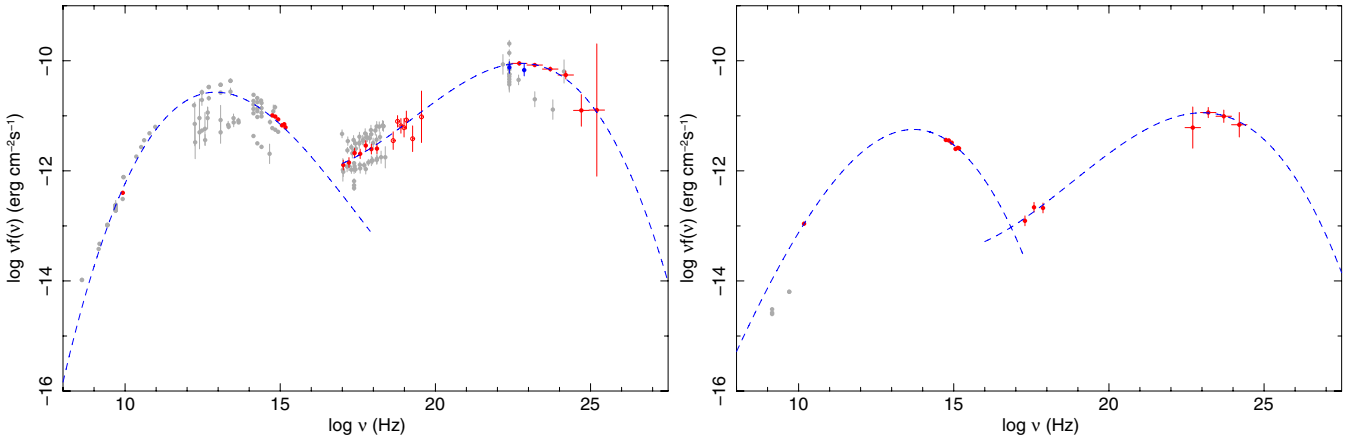

Figure 9. SED of 0FGL J0538.8−4403 = PKS0537-441. (left) and of 0FGL J0712.9+5034 = GB6 J0712+5033 (right).
(A color version of this figure is available in the online journal.)

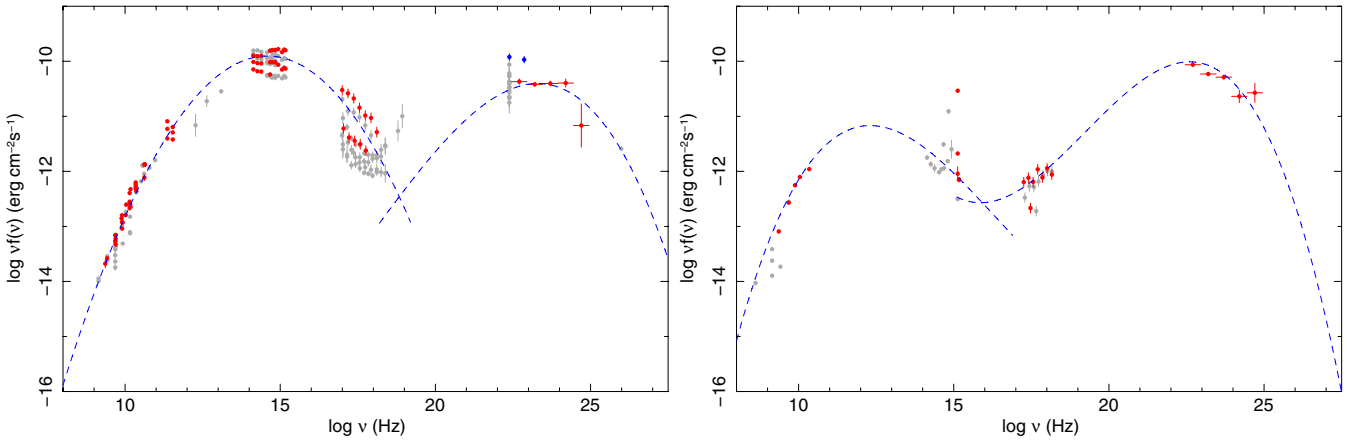

Figure 10. SED of 0FGL J0722.0+7120 = S50716+714 (left) and of 0FGL J0730.4−1142 = PKS0727-11 (right).
(A color version of this figure is available in the online journal.)

(open circles) can be found in all parts of the plane, albeit with a prevalence in the horizontal area defined by values of α_{ro} between 0.2 and 0.4, which is where HBL sources are located (Padovani & Giommi 1995). The area of the α_{ox}–α_{ro} space where the hypothetical population of ultra high energy peaked (UHBLs) blazars (that is, sources where the synchrotron component is so energetic as to peak in the MeV region; Ghisellini 1999; Giommi et al. 2001) could have been found, is empty, implying that these sources are either very rare, very weak, or non-existent (see also Costamante et al. 2007).

5.3. The Synchrotron Peak Energy (ν^S_{peak}) and Peak Intensity (ν^S_{peak} $F(\nu^S_{peak})$)

We estimated the peak energy (ν^S_{peak}) and peak intensity (ν^S_{peak} $F(\nu^S_{peak})$) of the synchrotron power from the SED reported in

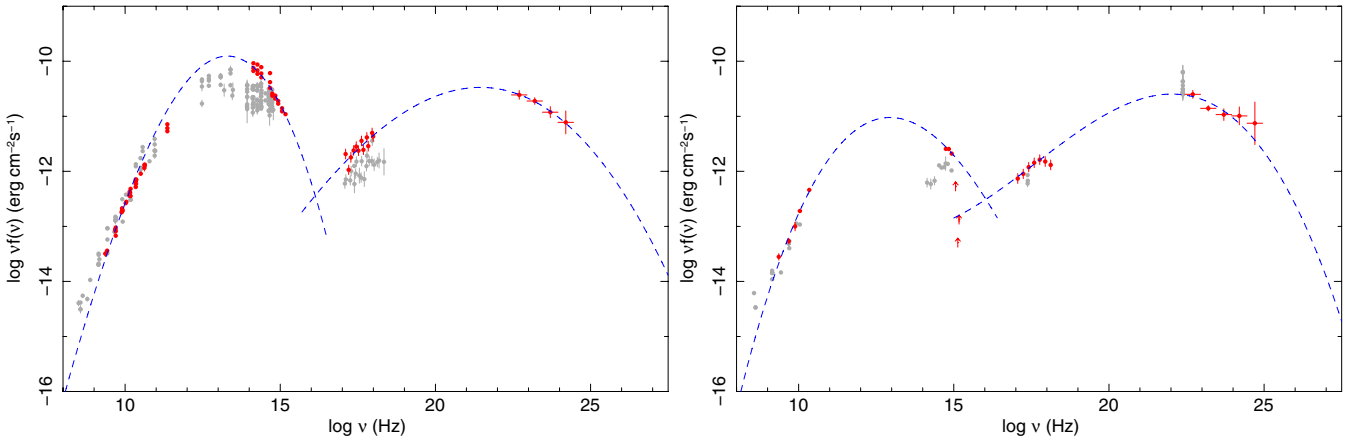

Figure 11. SED of 0FGL J0855.4+2009 = PKS0851+202 (left) and of 0FGL J0921.2+4437 = S40917+44 (right).
(A color version of this figure is available in the online journal.)

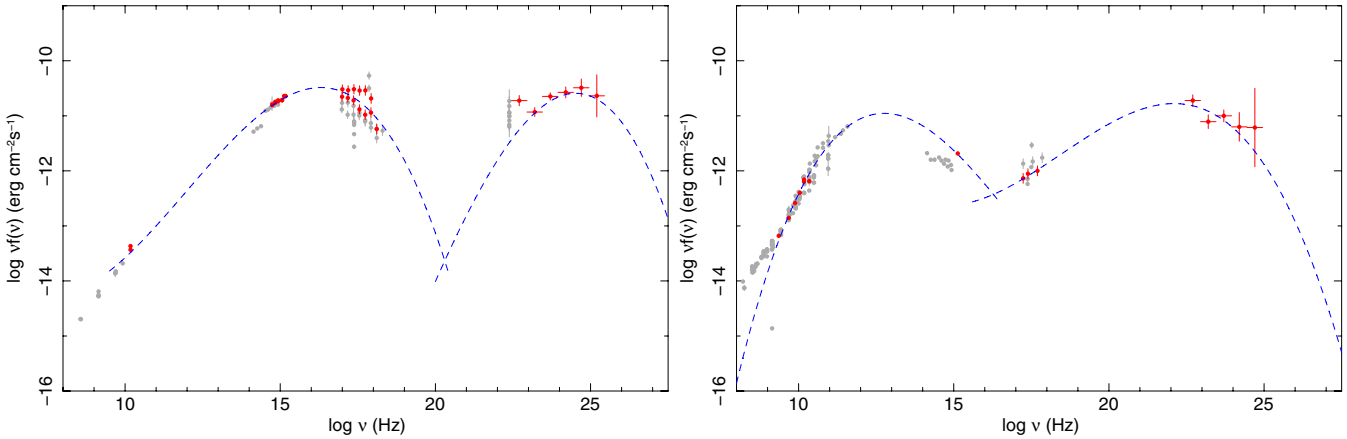

Figure 12. SED of 0FGL J1015.2+4927 = 1H 1013+498 (left) and of 0FGL J1057.8+0138 = 4C01.28 (right).
(A color version of this figure is available in the online journal.)

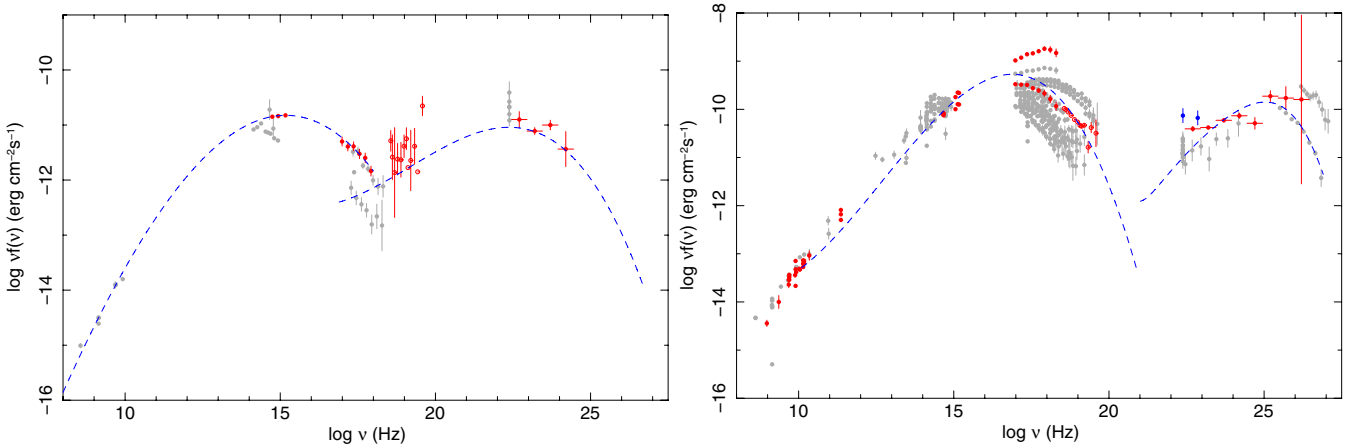

Figure 13. SED of 0FGL J1058.9+5629 = GB6 J1058+5628 (left) and of 0FGL J1104.5+3811 = Mkn 421 (right).
(A color version of this figure is available in the online journal.)

Figures 1–24 by fitting the part of the SED that is dominated by synchrotron emission. As a fitting function we used a simple third-degree polynomial (see Kubo et al. 1998):

$$\nu F_\nu = a \cdot \nu^3 + b \cdot \nu^2 + c \cdot \nu + d. \quad (2)$$

In the case of high redshift sources (e.g., J0229.5−3640, J0921.0+4437 and J1457.4−3538, J1522.2+3143), we excluded from the fitting procedure all points in the optical/UV bands that are likely to be significantly affected by Lyα forest absorption.

5.4. An Empirical Method to Derive $\nu^S_{\rm peak}$ and $\nu^S_{\rm peak}$ $F(\nu^S_{\rm peak})$ from $\alpha_{\rm ox}$ and $\alpha_{\rm ro}$

As shown by Padovani & Giommi (1995) the peak of the synchrotron power $\nu^S_{\rm peak}$ in the SED of a blazar determines its

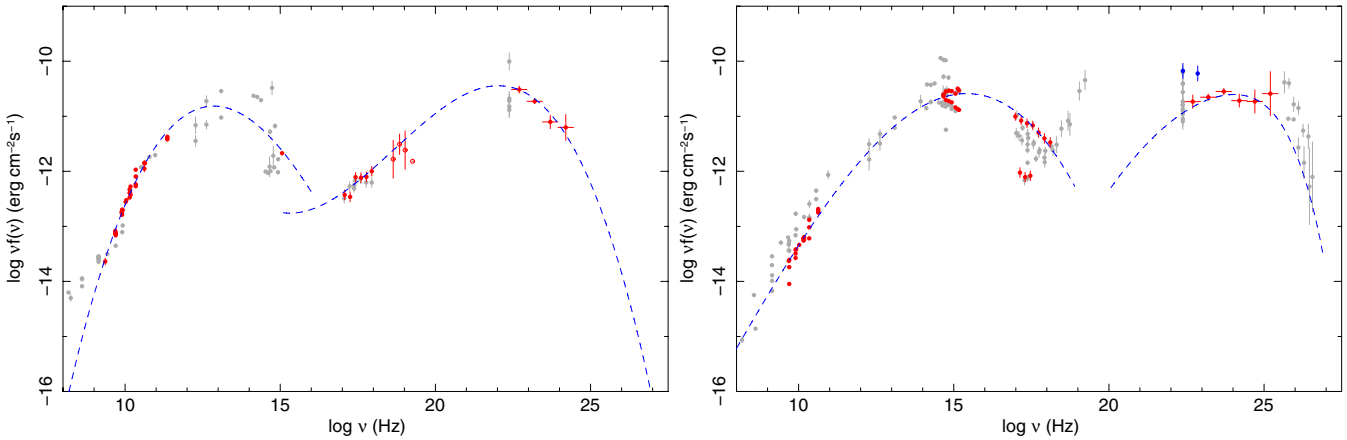

Figure 14. SED of 0FGL J1159.2+2912 = 4C29.45 (left) and of 0FGL J1221.7+2814 = ON231= W Comae (right).
(A color version of this figure is available in the online journal.)

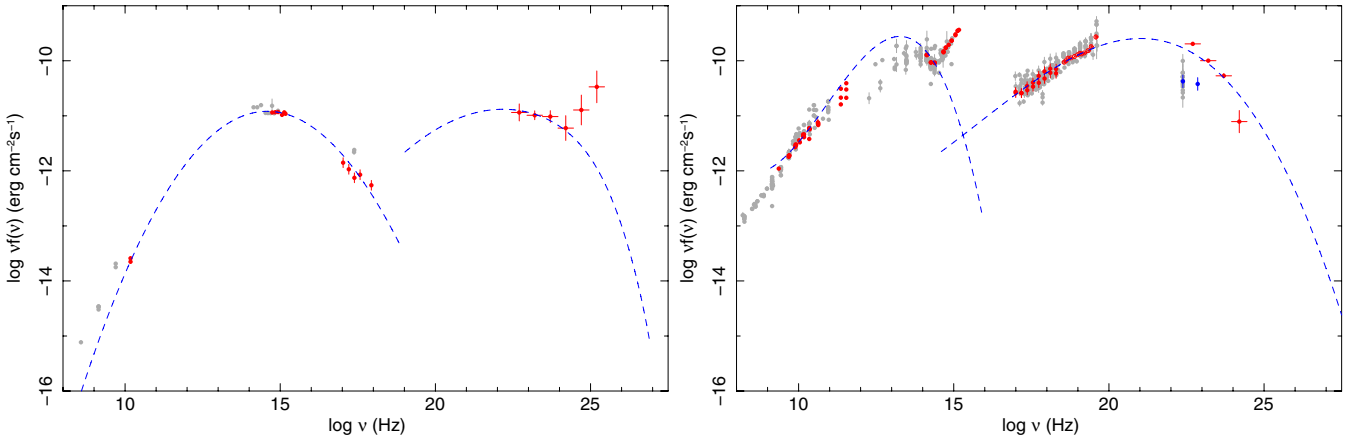

Figure 15. SED of 0FGL J1248.7+5811 = PG 1246+586 (left) and of 0FGL J1229.1+0202 = 3C273 (right).
(A color version of this figure is available in the online journal.)

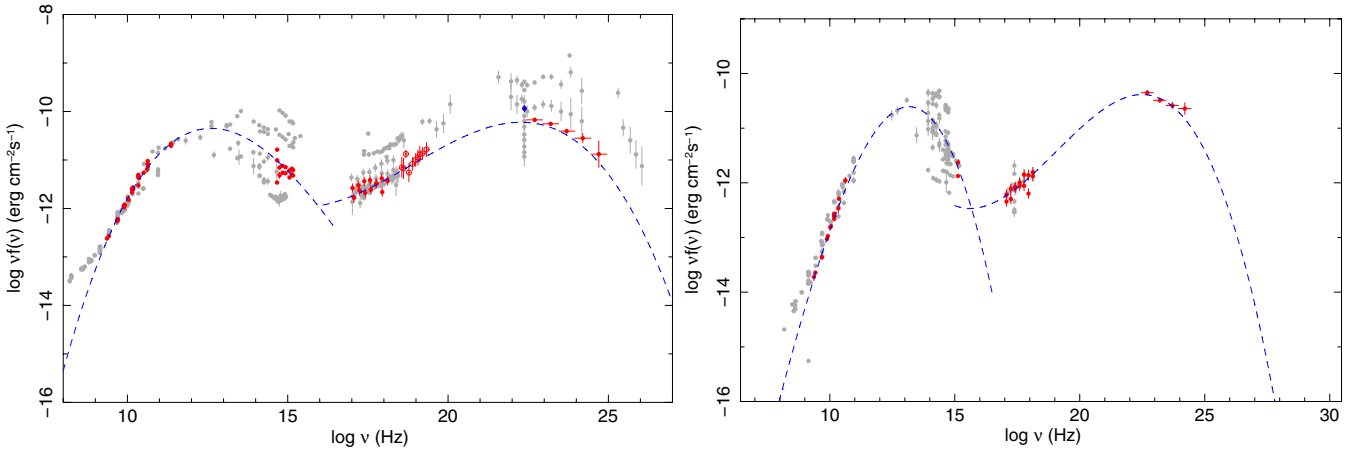

Figure 16. SED of 0FGL J1256.1−0547 = 3C279 (left) and of 0FGL J1310.6+3220 = 1Jy1308+326 (right)
(A color version of this figure is available in the online journal.)

position in the α_{ox}–α_{ro} plane (see Figure 12 of Padovani & Giommi (1995), see also Padovani et al. (2003)). Here we exploit this dependence showing that the value of ν^S_{peak} can be estimated from α_{ox}–α_{ro} through the following analytical relationship,

$$\mathrm{Log}(\nu_{\mathrm{peak_S}}) = \begin{cases} 13.85 + 2.30X & \text{if } X < 0 \text{ and } Y < 0.3 \\ 13.15 + 6.58Y & \text{otherwise,} \end{cases} \quad (3)$$

where $X = 0.565 - 1.433 \cdot \alpha_{ro} + 0.155 \cdot \alpha_{ox}$ and $Y = 1.0 - 0.661 \cdot \alpha_{ro} - 0.339 \cdot \alpha_{ox}$

We have calibrated this relationship using the ν^S_{peak} values directly measured from our 48 quasi-simultaneous SED and the corresponding α_{ox} and α_{ro} values.

Figure 28 (top panel) shows the values of $\log(\nu^S_{peak})$ estimated from Equation (3) plotted against the values of $\log(\nu^S_{peak})$

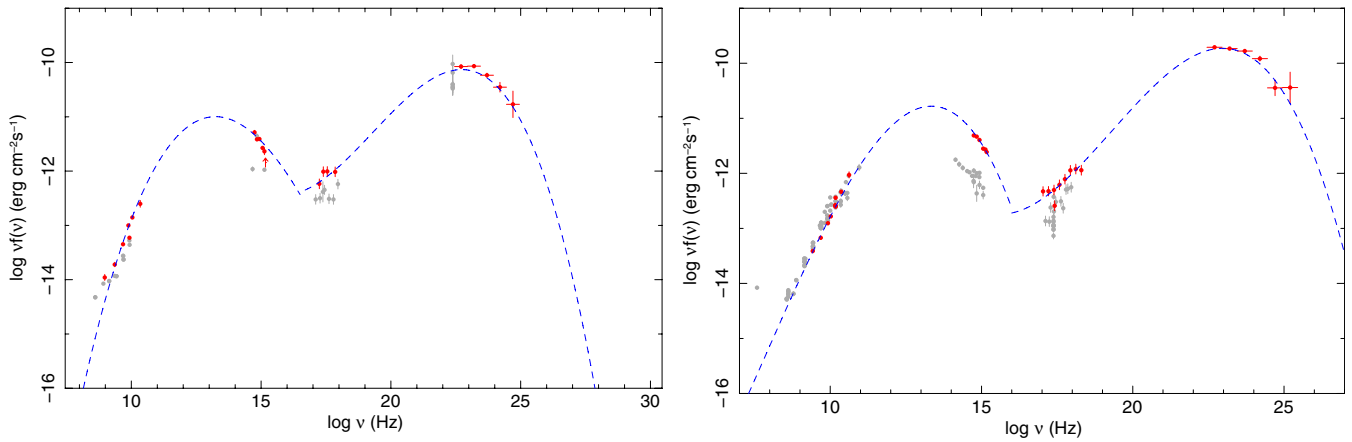

Figure 17. SED of 0FGL J1457.6−3538 = PKS 1454-354 (left) and of 0FGL J1504.3+1030 = PKS1502+106 (right).
(A color version of this figure is available in the online journal.)

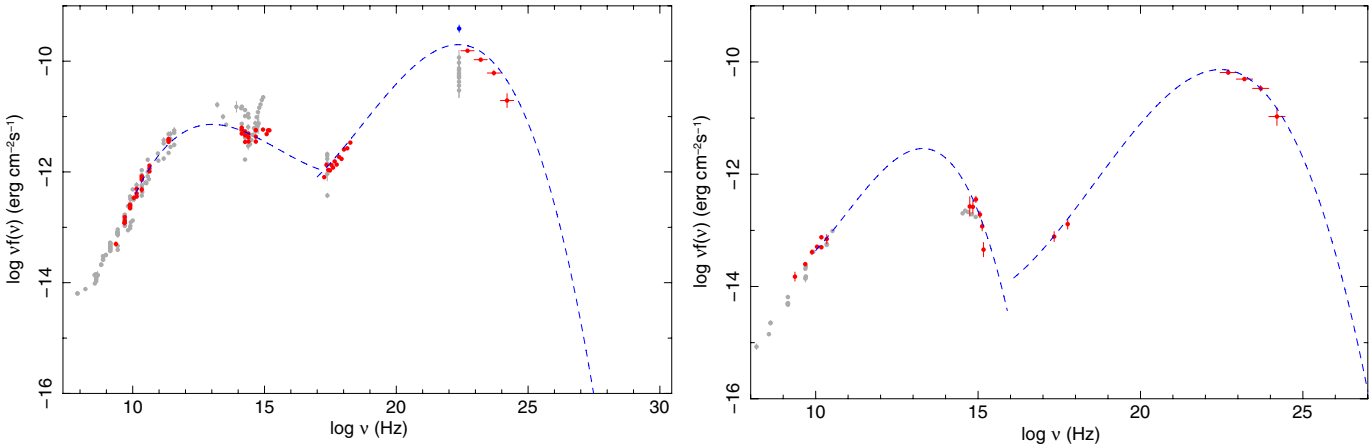

Figure 18. SED of 0FGL J1512.7−0905 = PKS 1510-089 (left) and of 0FGL J1522.2+3143 = B2 1520+31 (right).
(A color version of this figure is available in the online journal.)

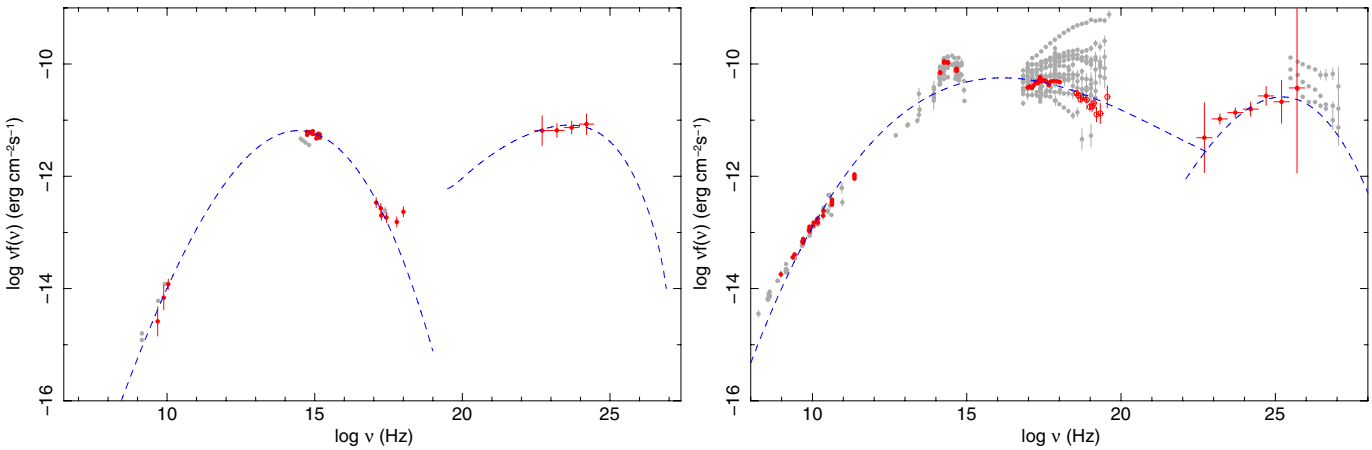

Figure 19. SED of 0FGL J1543.1+6130 = GB6 J1542+6129 (left) and of 0FGL J1653.9+3946 = Mkn 501 (right).
(A color version of this figure is available in the online journal.)

measured by fitting a SSC model to the synchrotron part of the quasi-simultaneous SED of Figures 1 to 24. The distribution of the difference between the values estimated with the two methods has a mean value of 0.04 and a standard deviation of 0.58, implying that the value of $\log(\nu^S_{\rm peak})$ can be derived even from non-simultaneous values of $\alpha_{\rm ox}$ and $\alpha_{\rm ro}$ within 0.6 decade at 1σ level and within one decade in almost all cases.

It must be noted, however, that this method assumes that the optical and X-ray fluxes are not contaminated by thermal emission from the disk or accretion. In blazars where thermal flux components are not negligible (this should probably occur

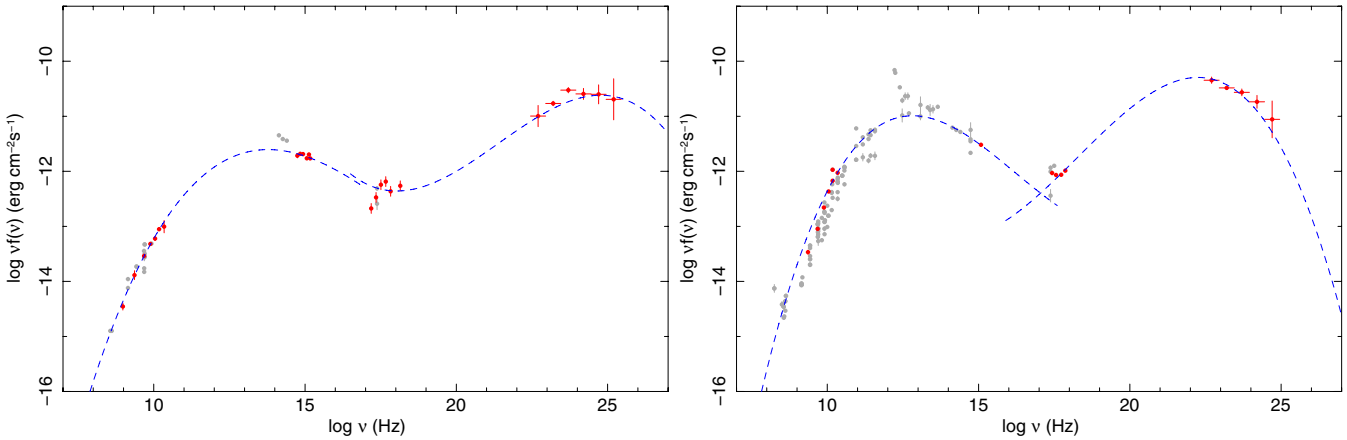

Figure 20. SED of 0FGL J1719.3+1746 = PKS 1717+177 (left) and of 0FGL J1751.5+0935 = OT081 (right).
(A color version of this figure is available in the online journal.)

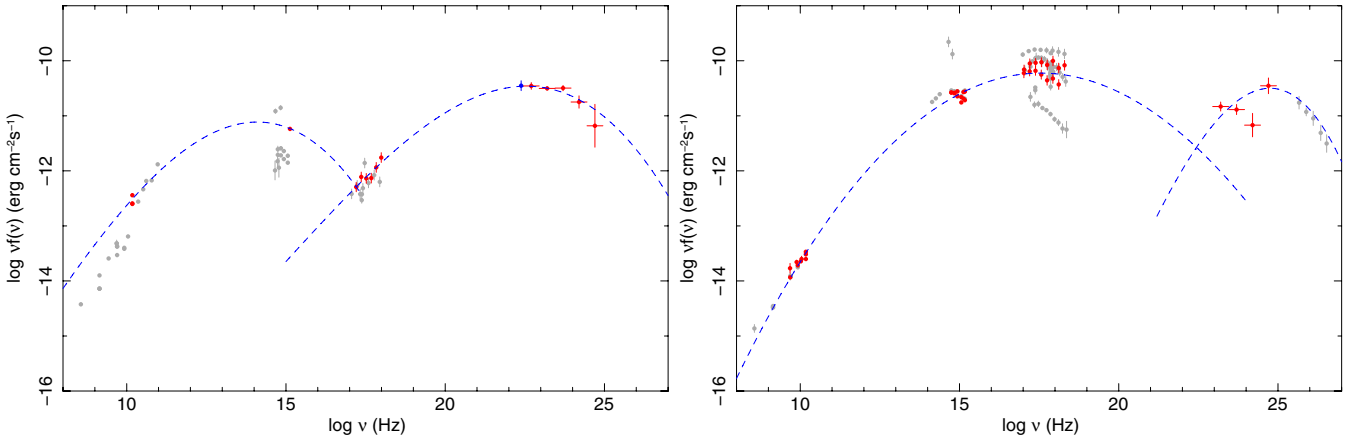

Figure 21. SED of 0FGL J1849.4+6706 = 4C66.20 (left) and of 0FGL J2000.2+6506 = 1ES1959+650 (right).
(A color version of this figure is available in the online journal.)

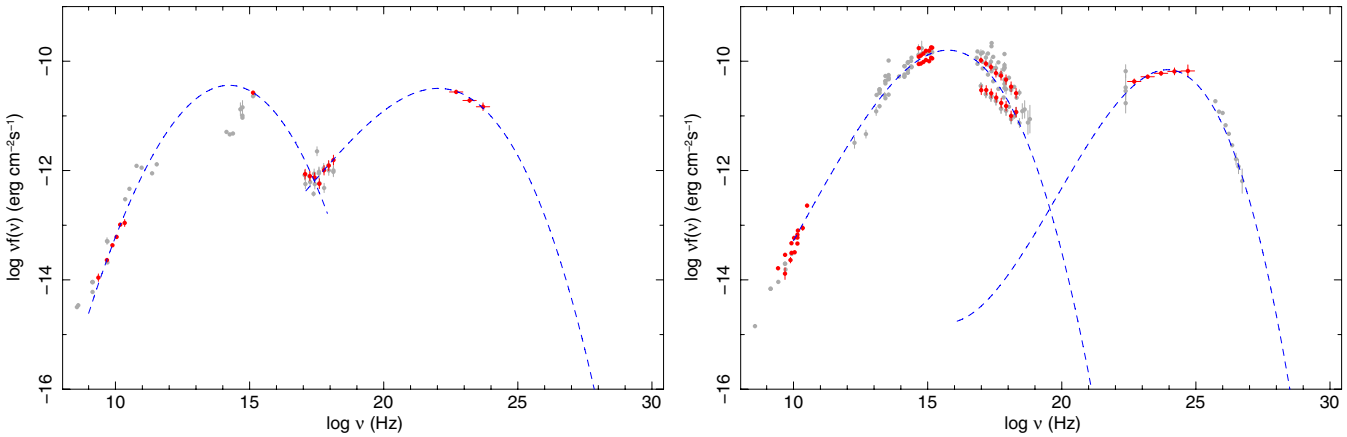

Figure 22. SED of 0FGL J2143.2+1741 = S3 2141+17 (left) and of 0FGL J2158.8−3014 = PKS2155-304 (right).
(A color version of this figure is available in the online journal.)

more frequently in low radio luminosity sources) the method described above may lead to a significant overestimation of the position of $\nu^S_{\rm peak}$.

The peak flux $\nu^S_{\rm peak}\ F(\nu^S_{\rm peak})$ can be estimated using the following relationship:

$$\log\left(\nu^S_{\rm peak}F\left(\nu^S_{\rm peak}\right)\right) = 0.5\cdot\log\left(\nu^S_{\rm peak}\right) - 20.4 + 0.9\cdot\log(R_{5\,\rm GHz}), \quad (4)$$

where $R_{5\,\rm GHz}$ is the radio flux density at 5 GHz in units of mJy.

Figure 28 (bottom panel) plots the value of $\nu^S_{\rm peak}\ F(\nu^S_{\rm peak})$ estimated with the two methods. Also in this case the match is very good with an average value of −0.01 for the difference between the two estimates and a standard deviation of 0.33.

It is quite remarkable that one can derive the synchrotron peak flux simply from $\nu^S_{\rm peak}$ and from the radio flux as this implies

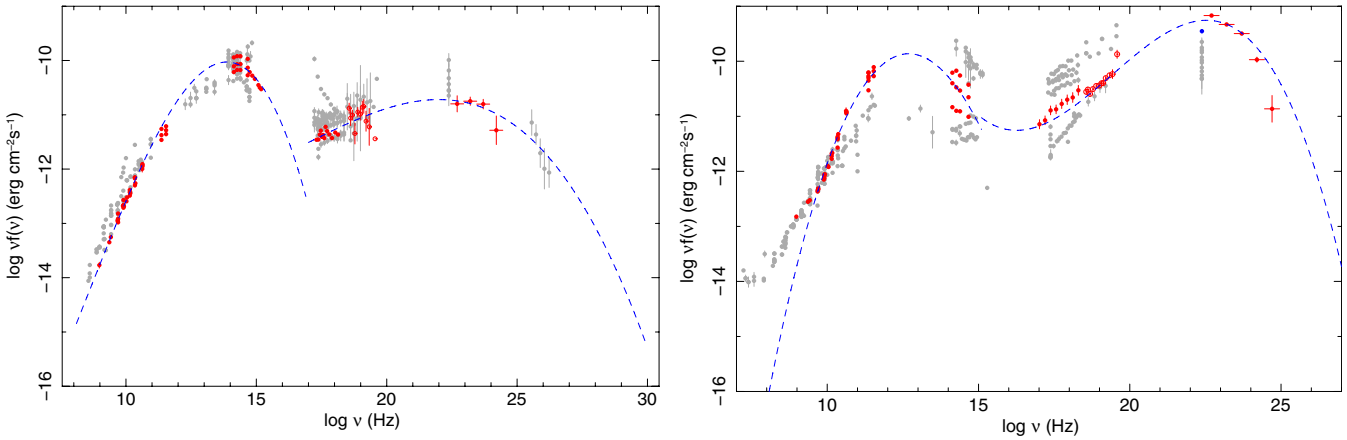

Figure 23. SED of 0FGL J2202.4+4217 = BL Lacertae (left) and of 0FGL J2254.0+1609 = 3C454.3 (right).
(A color version of this figure is available in the online journal.)

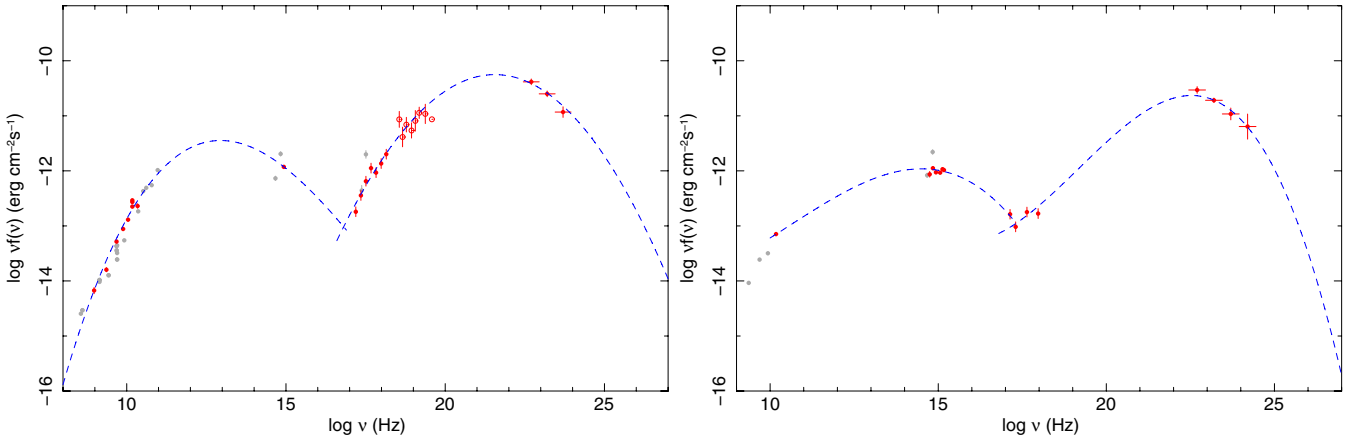

Figure 24. SED of 0FGL J2327.3+0947 = PKS 2325+093 (left) and of 0FGL J2344.5−1559 = PMN J2345-1555 (right).
(A color version of this figure is available in the online journal.)

that within a factor of 10 the radio emission represents a long-term calorimeter for the whole jet activity and the basic source power.

5.5. The Peak Frequency and Peak Intensity of the Inverse Compton Bump

We have estimated the peak of the inverse Compton power in the SED ($\nu^{\rm IC}_{\rm peak}$) and the corresponding peak flux ($\nu^{\rm IC}_{\rm peak}$ F($\nu^{\rm IC}_{\rm peak}$)) by fitting the X-ray to γ-ray part of the SED, which is dominated by inverse Compton emission using the polynomial function of Equation (2).

There are some objects in which the soft X-ray band is still dominated by synchrotron radiation, and only the *Fermi* data can be used to constrain the inverse Compton component, so the above method is subject to large uncertainties. For this reason, in these cases, we have used the ASDC SED[97] interface to fit the simultaneous data points to a SSC model with a log-parabolic electron spectrum (Tramacere et al. 2009).

The polynomial fits described above are a very good representation of the data for almost all the SED shown in Figures 1–24; the only two significant exceptions are 3C66A (see Figure 3, left side) and 3C273 (see Figure 15, right side). In the first case, this could be the result of the short-term variability that is clearly visible in the optical/UV and X-ray data. While the γ-ray photons were collected during the *Fermi* data taking period the synchrotron, and inverse Compton, peak frequencies probably changed causing the unusual shape of the spectrum which reflects the average of all the physical states the source went through during the long γ-ray observation. In the case of 3C273 the excess of optical/UV light above the polynomial fit is attributed to the source strong blue continuum which is due to accretion and not non-thermal radiation; for this reason, this part of the spectrum was excluded from the fit.

For the whole sample we have determined $\nu^{\rm IC}_{\rm peak}$ as the value of ν which maximizes νF_ν in Equation (2) or the predictions of the SSC model. The results are reported in Columns 6 and 7 of Table 13. The best fit to both the synchrotron and inverse Compton components appears as dashed lines in Figures 1–24.

Figure 29 (bottom panel) shows that the $\nu^{\rm IC}_{\rm peak}$, derived as described above for the 48 sources for which we have built the SED, is strongly correlated with their γ-ray spectral slope (Γ) taken from Table 3 of Abdo et al. (2009b). We note that the scatter in the plots of Figure 29 is largest in the regions of low $\nu^{S}_{\rm peak}/\nu^{\rm IC}_{\rm peak}$–steep values of Γ, probably reflecting the presence of γ-ray spectral curvature (see Section 4). The best fit to the $\nu^{\rm IC}_{\rm peak}$–Γ relationship is

$$\log\left(\nu^{\rm IC}_{\rm peak}\right) = -4.0 \cdot \Gamma + 31.6. \quad (5)$$

Since the 48 objects for which we have quasi-simultaneous

[97] http://tools.asdc.asi.it/SED/

Table 13
Blazar SED Parameters

Name 0FGL (1)	SED Available (2)	α_r (3)[a]	$\log(\nu^S_{\rm peak})$ (4)[b]	$\log(\nu^S_{\rm peak}\ {\rm F}(\nu^S_{\rm peak}))$ (5)[b]	$\log(\nu^{\rm IC}_{\rm peak})$ (6)[c]	$\log(\nu^{\rm IC}_{\rm peak}\ F(\nu^{\rm IC}_{\rm peak}))$ (7)	$\log(\gamma^{\rm SSC}_{\rm peak})$ (8)[d]	Compton Dominance (9)	SED Classification (10)	Optical Classification (11)
J0017.4−0503	...	0.127	−/13.6	−/−11.4	−/20.7	...	3.4	...	LSP	FSRQ
J0033.6−1921	Yes	0	16.1/16.3	−11.1/−11.2	24.3/24.8	−11.1	4	1	HSP	BL Lac
J0050.5−0928	Yes	0.205	14.3/14.4	−10.8/−10.6	22.4/23	−10.6	4	1.8	ISP	BL Lac
J0051.1−0647	...	−0.103	−/12.8	−/−11.4	−/22.7	...	4.9	...	LSP	FSRQ
J0100.2+0750	...	−0.076	−/−	−/−	−/24.4	...	...	...	...	Unidentified
J0112.1+2247	...	0.121	−/14.6	−/−10.8	−/23.1	...	4.1	...	ISP	BL Lac
J0118.7−2139	...	0.089	−/13	−/−11.5	−/22.3	...	4.5	...	LSP	FSRQ
J0120.5−2703	...	−0.114	−/13.9	−/−10.8	−/23.6	...	4.7	...	LSP	BL Lac
J0136.6+3903	...	0	−/16	−/−10.9	−/24.9	...	4.4	...	HSP	BL Lac
J0137.1+4751	Yes	0.192	13.6/13.3	−10.5/−10.8	22.6/22.8	−10.6	4.4	0.8	LSP	FSRQ
J0144.5+2709	...	0.011	−/−	−/−	−/22.7	...	...	...	...	BL Lac
J0145.1−2728	...	−0.199	−/13.3	−/−11.2	−/21.4	...	3.9	...	LSP	FSRQ
J0204.8−1704	...	−0.017	−/13.3	−/−11	−/21.6	...	4.1	...	LSP	FSRQ
J0210.8−5100	Yes	−0.099	12.5/13.8	−10.7/−10.4	22.4/22.4	−10.2	4.8	3.6	LSP	FSRQ
J0217.8+0146	...	0.237	−/12.9	−/−11.1	−/23	...	5	...	LSP	FSRQ
J0220.9+3607	...	−0.186	−/12.4	−/−11.4	−/21.1	...	4.3	...	LSP	FSRQ
J0222.6+4302	Yes	0	15.1/14.4	−10.2/−10.6	24.2/23.7	−10.2	4.4	1	ISP	BL Lac
J0229.5−3640	Yes	0	13.5/13	−11.7/−12	21.8/21.3	−10.4	4.1	20.3	LSP	FSRQ
J0238.4+2855	Yes	0.126	12.8/12.8	−10.7/−11	22.1/21.6	−10.8	4.6	0.9	LSP	FSRQ
J0238.6+1636	Yes	0.557	13.5/13.1	−10/−10.9	23.2/23.3	−9.9	4.8	1.5	LSP	BL Lac
J0245.6−4656	...	−0.397	−/13.1	−/−11.2	−/22.2	...	4.4	...	LSP	BZU
J0303.7−2410	...	−0.664	−/15.1	−/−10.6	−/23.5	...	4.1	...	HSP	BL Lac
J0334.1−4006	...	−0.036	−/13.3	−/−11	−/23	...	4.8	...	LSP	BL Lac
J0349.8−2102	Yes	0.014	12.9/13	−11.3/−11.6	21.8/21.3	−10.2	4.4	13.5	LSP	FSRQ
J0407.6−3829	...	0	−/13.6	−/−11	−/22.3	...	4.2	...	LSP	Unidentified
J0412.9−5341	...	−0.513	−/−	−/−	−/22.4	...	...	...	...	Unidentified
J0423.1−0112	Yes	−0.081	13.4/13.3	−10.9/−10.5	21.7/22	−10.3	4	4.1	LSP	FSRQ
J0428.7−3755	Yes	0.419	13.3/13.6	−11/−10.8	22.8/23	−10.2	4.6	6.3	LSP	BL Lac
J0449.7−4348	Yes	−0.498	15.6/15.4	−10.2/−10.6	23.9/23.5	−10.5	4.1	0.5	HSP	BL Lac
J0457.1−2325	Yes	−0.074	13.1/13	−11/−11	22.8/22.6	−9.9	4.7	12.5	LSP	FSRQ
J0507.9+6739	Yes	0	16.6/16.3	−10.7/−11	24.3/24.9	−10.5	3.7	1.4	HSP	BL Lac
J0516.2−6200	Yes	0.226	13.6/13	−11.3/−11.5	22.5/22.9	−10.7	4.4	4.1	LSP	BZU
J0531.0+1331	Yes	0.239	12.8/13.1	−10.9/−10.7	21.3/21.4	−9.8	4.2	11.6	LSP	FSRQ
J0538.8−4403	Yes	−0.084	13.4/13.6	−10.6/−10.3	22.7/22.8	−10.1	4.6	3.6	LSP	BL Lac
J0654.3+5042	...	0.231	−/−	−/−	−/23.5	...	...	...	...	BZU
J0654.3+4513	...	0.005	−/13	−/−11.6	−/22.3	...	4.6	...	LSP	FSRQ
J0700.0−6611	...	−0.173	−/14.1	−/−11.2	−/23.6	...	4.6	...	ISP	BZU
J0712.9+5034	Yes	0.403	13.6/14.3	−11.3/−11.4	23/23.4	−11	4.6	2.1	ISP	BL Lac
J0714.2+1934	...	0	−/−	−/−	−/22.1	...	...	...	...	BZU
J0719.4+3302	...	−0.149	−/13.6	−/−11.4	−/22.1	...	4.2	...	LSP	FSRQ
J0722.0+7120	Yes	−0.126	14.6/14.4	−9.9/−10.6	23.3/23.2	−10.4	4.2	0.3	ISP	BL Lac
J0730.4−1142	Yes	0	13.1/12.8	−11.1/−10.7	22.6/22.5	−10	4.6	10.1	LSP	FSRQ
J0738.2+1738	...	0.271	−/13.8	−/−10.6	−/23.1	...	4.6	...	LSP	BL Lac
J0818.3+4222	...	−0.042	−/12.6	−/−11.2	−/23.3	...	5.2	...	LSP	BL Lac
J0824.9+5551	...	0.095	−/13	−/−11.2	−/20.3	...	3.5	...	LSP	FSRQ
J0855.4+2009	Yes	0.443	13.4/13.9	−9.8/−10.4	21.4/22.3	−10.5	3.9	0.2	LSP	BL Lac
J0909.7+0145	...	0.193	−/−	−/−	−/20.9	...	...	...	...	BL Lac
J0921.2+4437	Yes	0.153	13.4/12.6	−11.2/−11.4	22/22.2	−10.6	4.2	3.3	LSP	FSRQ
J0948.3+0019	...	0.645	−/13.8	−/−11.3	−/21.1	...	3.6	...	LSP	FSRQ
J0957.6+5522	...	−0.41	−/13.1	−/−10.9	−/23.5	...	5	...	LSP	FSRQ
J1012.9+2435	...	−0.19	−/14.8	−/−11.3	−/22.7	...	3.9	...	ISP	FSRQ
J1015.2+4927	Yes	−0.239	16.3/15.5	−10.5/−10.5	24.5/24.6	−10.6	3.9	0.8	HSP	BL Lac
J1015.9+0515	...	−0.178	−/−	−/−	−/22.7	...	...	...	...	FSRQ
J1034.0+6051	...	−0.054	−/12.8	−/−11.6	−/21.6	...	4.3	...	LSP	FSRQ
J1053.7+4926	...	0	−/15	−/−11.3	−/25.9	...	5.3	...	ISP	BL Lac
J1054.5+2212	...	0	−/14.6	−/−11.6	−/22.6	...	3.9	...	ISP	BL Lac
J1058.9+5629	Yes	−0.115	14.6/15	−10.9/−10.8	22.3/23.1	−11	3.7	0.7	ISP	BL Lac
J1057.8+0138	Yes	0.002	13.1/13.1	−10.8/−10.7	22/22.7	−10.8	4.3	1	LSP	BZU
J1100.2−8000	...	0.489	−/13.4	−/−10.8	−/20.7	...	3.6	...	LSP	BL Lac
J1104.5+3811	Yes	−0.109	16.6/16.1	−9.4/−9.8	25/24.5	−9.9	4.1	0.3	HSP	BL Lac
J1129.8−1443	...	−0.387	−/13.3	−/−10.6	−/20.8	...	3.7	...	LSP	FSRQ
J1146.7−3808	...	0.217	−/13.6	−/−10.6	−/22.7	...	4.4	...	LSP	FSRQ
J1159.2+2912	Yes	−0.286	13.1/13.5	−10.7/−10.9	22/21.6	−10.5	4.3	1.8	LSP	FSRQ
J1218.0+3006	...	−0.299	−/15.5	−/−10.3	−/24	...	4.1	...	HSP	BL Lac

Table 13
(Continued)

Name 0FGL (1)	SED Available (2)	α_r (3)[a]	$\log(\nu^S_{\rm peak})$ (4)[b]	$\log(\nu^S_{\rm peak}\ F(\nu^S_{\rm peak}))$ (5)[b]	$\log(\nu^{\rm IC}_{\rm peak})$ (6)[c]	$\log(\nu^{\rm IC}_{\rm peak}\ F(\nu^{\rm IC}_{\rm peak}))$ (7)	$\log(\gamma^{\rm SSC}_{\rm peak})$ (8)[d]	Compton Dominance (9)	SED Classification (10)	Optical Classification (11)
J1221.7+2814	Yes	0.194	14.5/14.1	−10.6/−10.6	24/23.8	−10.6	4.7	0.8	ISP	BL Lac
J1229.1+0202	Yes	−0.158	13.5/13	−9.8/−9.7	21/20.7	−9.6	3.6	1.3	LSP	FSRQ
J1246.6−2544	...	0.245	−/13.4	−/−10.7	−/22.6	...	4.5	...	LSP	FSRQ
J1248.7+5811	Yes	0.147	14.6/15	−11/−10.7	22.1/23.8	−10.9	3.7	1.2	ISP	BL Lac
J1253.4+5300	...	−0.165	−/13.9	−/−11.2	−/22.9	...	4.4	...	LSP	BL Lac
J1256.1−0548	Yes	0.541	12.6/13.1	−10.3/−10.2	22.2/22.1	−10.3	4.7	1.1	LSP	FSRQ
J1310.6+3220	Yes	0.304	13.1/12.5	−10.9/−11.4	22.5/22.6	−10.4	4.6	3.3	LSP	FSRQ
J1331.7−0506	...	0.083	−/13.1	−/−11.4	−/21.2	...	3.9	...	LSP	FSRQ
J1333.3+5058	...	0	−/−	−/−	−/22	...	...	...	...	FSRQ
J1355.0−1044	...	−0.37	−/13.6	−/−11.1	−/22.1	...	4.1	...	LSP	FSRQ
J1427.1+2347	...	−0.338	−/14.9	−/−10.7	−/24.3	...	4.6	...	ISP	BL Lac
J1457.6−3538	Yes	−0.054	13.6/13	−10.9/−11.5	22.7/22.6	−10.2	4.4	5.6	LSP	FSRQ
J1504.4+1030	Yes	−0.03	13.6/12.5	−11/−11.1	22.9/22.9	−9.8	4.6	16.6	LSP	FSRQ
J1511.2−0536	...	0	−/13.3	−/−10.9	−/21.9	...	4.2	...	LSP	FSRQ
J1512.7−0905	Yes	0	13.1/13.6	−10.6/−10.6	22.3/21.6	−9.7	4.5	7.4	LSP	FSRQ
J1517.9−2423	...	0.085	−/13.8	−/−10.6	−/23.8	...	4.9	...	LSP	BL Lac
J1522.2+3143	Yes	0.182	13.3/12.9	−11.5/−11.8	22.4/22	−10.2	4.5	23.3	LSP	FSRQ
J1543.1+6130	Yes	0.268	14.1/14.6	−11.2/−11.3	23.5/23.5	−11.1	4.6	1.1	ISP	BL Lac
J1553.4+1255	...	−0.474	−/−	−/−	−/22.6	...	...	...	...	FSRQ
J1555.8+1110	...	0.258	−/15.4	−/−10.3	−/24.7	...	4.6	...	HSP	BL Lac
J1625.8−2527	...	−0.04	−/12.4	−/−11.1	−/22	...	4.7	...	LSP	FSRQ
J1625.9−2423	...	0.162	−/−	−/−	−/21.7	...	...	...	...	Unidentified
J1635.2+3809	...	−0.085	−/13.1	−/−10.7	−/21.8	...	4.2	...	LSP	FSRQ
J1641.4+3939	...	0.282	−/12.9	−/−11.2	−/21.8	...	4.4	...	LSP	FSRQ
J1653.9+3946	Yes	−0.189	17.1/15.3	−10.3/−10	24.7/24.7	−10.5	3.7	0.5	HSP	BL Lac
J1719.3+1746	Yes	0.032	13.5/13.6	−11.3/−11.2	24.7/24.2	−10.7	5.5	4.6	LSP	BL Lac
J1751.5+0935	Yes	0.64	13.1/13.5	−10.8/−10.6	22.2/22.5	−10.3	4.4	3	LSP	BL Lac
J1802.2+7827	...	0.129	−/13.8	−/−10.5	−/22.5	...	4.3	...	LSP	BL Lac
J1847.8+3223	...	0.106	−/13.1	−/−11.3	−/22.1	...	4.4	...	LSP	FSRQ
J1849.4+6706	Yes	−0.063	13.5/13.5	−10.6/−11.1	22.5/22.9	−10.5	4.4	1.3	LSP	FSRQ
J1911.2−2011	...	0.055	−/12.6	−/−11.1	−/21.8	...	4.5	...	LSP	FSRQ
J1923.3−2101	...	−0.092	−/13.3	−/−10.7	−/22.3	...	4.4	...	LSP	FSRQ
J2000.2+6506	Yes	−0.083	16.6/15.9	−10/−10.3	24.7/24.1	−10.5	3.9	0.3	HSP	BL Lac
J2009.4−4850	...	−0.182	−/15.3	−/−10	−/24.1	...	4.3	...	HSP	BL Lac
J2017.2+0602	...	0	−/14.3	−/−11.9	−/24.1	...	4.8	...	ISP	Unidentified
J2025.6−0736	...	−0.339	−/12.9	−/−11.4	−/22.3	...	4.6	...	LSP	FSRQ
J2056.1−4715	...	−0.161	−/12.9	−/−11	−/21.3	...	4.1	...	LSP	FSRQ
J2139.4−4238	...	0.093	−/14.8	−/−11.2	−/23.5	...	4.3	...	ISP	BL Lac
J2143.2+1741	Yes	0.48	14.1/13.9	−10.4/−10.8	22/21.3	−10.5	3.8	0.8	LSP	FSRQ
J2147.1+0931	...	0.027	−/13.5	−/−10.9	−/21.4	...	3.9	...	LSP	FSRQ
J2157.5+3125	...	0.07	−/12.9	−/−11.6	−/21.9	...	4.4	...	LSP	FSRQ
J2158.8−3014	Yes	−0.179	16/16.5	−9.7/−9.8	23.9/24.1	−10.2	3.9	0.3	HSP	BL Lac
J2202.4+4217	Yes	0	13.6/13.8	−10.1/−10.4	21.9/22.6	−10.8	4	0.2	LSP	BL Lac
J2203.2+1731	...	0.317	−/12.9	−/−11.4	−/22.5	...	4.7	...	LSP	FSRQ
J2207.0−5347	...	−0.12	−/13	−/−11.1	−/21	...	3.9	...	LSP	FSRQ
J2229.8−0829	...	0.127	−/13.4	−/−10.7	−/20.9	...	3.6	...	LSP	FSRQ
J2232.4+1141	...	0	−/13.1	−/−10.7	−/21.1	...	3.9	...	LSP	FSRQ
J2254.0+1609	Yes	−0.112	13.6/13.8	−9.5/−9.8	22.5/21.9	−9.3	4.3	1.7	LSP	FSRQ
J2325.3+3959	...	−0.003	−/14	−/−11.6	−/24	...	4.9	...	LSP	BL Lac
J2327.3+0947	Yes	−0.08	13.1/13	−11/−11.4	21.5/20.6	−10.3	4.1	5.1	LSP	FSRQ
J2345.5−1559	Yes	0.385	13.3/13.3	−11.7/−11.3	22.5/21.9	−10.7	4.5	9.7	LSP	FSRQ

Notes.

[a] The radio power-law spectral index α_r is evaluated in the range 1–100 GHz.

[b] The value to the left is estimated directly from SED, while the value reported to the right has been estimated from $\alpha_{\rm ox}$–$\alpha_{\rm ro}$.

[c] The value to the left is estimated directly from SED, while the value reported to the right has been estimated from Equation (5).

[d] Calculated assuming a simple SSC emission mechanism, i.e., $\gamma^{\rm SSC}_{\rm peak} = \sqrt{3/4 \cdot \nu^{\rm IC}_{\rm peak}/\nu^S_{\rm peak}}$.

SED are representative of the entire LBAS sample, the above equation can be used to estimate the $\nu^{\rm IC}_{\rm peak}$ of the LBAS sources for which we have no simultaneous SED. We have done so and we have listed the results in Column 6 of Table 13. The statistical uncertainty associated with $\nu^{\rm IC}_{\rm peak}$ calculated via Equation (5) can be estimated from the distribution of the difference between

ν^{IC}_{peak} measured from the SED and that from Equation (5). This distribution is centered on the value of 0 and has a sigma of 0.51; considering that the value of ν^{IC}_{peak} from the SED is also subject to a similar error we conservatively conclude that the log of ν^{IC}_{peak} values estimated through Equation (5) has an associated error of about 0.7.

6. AN SED-BASED CLASSIFICATION SCHEME FOR BLAZARS AND OTHER AGNs

Blazars, like other types of AGNs, have been classified in the past according to heterogeneous criteria, often based on observational properties related to the energy band where they were first discovered. This lack of a stable and clear definition can lead to multiple classification of the same object and may cause subtle selection effects and biases in statistical analyses. Now that *Fermi* has started producing large and homogeneous samples of blazars it is useful to re-assess the issue of blazar classification from a physical viewpoint taking into account the results of our SED study, so as to build a more robust base for future statistical/populations work.

We describe here a physical classification scheme based on the widely accepted AGN standard paradigm (e.g., Urry & Padovani 1995) and on well-known radiation emission processes.

The radiation emitted by an AGN is usually attributed to one (or both) of the following two physical processes.

1. Thermal radiation originating from in-falling matter strongly heated in the inner parts of an accretion disk close to the black hole. This radiation is often assumed to be Comptonized by a hot corona producing the power-law X-ray emission.
2. Non-thermal emission emitted in a magnetic field by highly energetic particles that have been accelerated in a jet of material ejected from the nucleus at relativistic speed.

The first process produces radiation mostly in the optical, UV, and X-ray bands, whereas the radiation produced through the second mechanism encompasses the entire electromagnetic spectrum, from radio waves, to the most energetic γ-rays. AGNs that are energetically dominated by thermal radiation (in the optical-X-ray band) can be classified as *thermal-dominated*, or *disk-dominated* AGNs, whereas AGNs where the non-thermal processes are energetically dominant at all frequencies can be classified as *non-thermal radiation dominated* or *jet-dominated* AGNs. AGNs can therefore be subdivided as follows.

1. Thermal/disk-dominated AGNs
   These are objects usually called QSOs or Seyfert galaxies which do not show significant nuclear radio emission compared to the observed emission in the optical or X-ray band. Although thermal-dominated AGNs are the large majority (≈90 %) of AGNs, here we do not go into further detail about their sub-classification since none of the sources so far detected by *Fermi is* thermal/disk dominated.

   We feel, however, that it is necessary to consider this type of AGN in this context as in some cases both the accretion (thermal) and the jet (non-thermal) component may be present in the optical, UV, or X-ray flux of the same object (e.g., 3C120, 3C 273; Grandi et al. 2004). This mix of accretion and non-thermal radiation is rarely seen in the very bright γ-ray sources detected so far, but it will probably become more common as the sensitivity of the *Fermi* survey increases with time and a large number of fainter and less aligned sources are detected.
2. Non-thermal/jet-dominated AGNs
   The class of non-thermal/jet powered AGNs corresponds to the usual type of sources known as radio loud AGNs. These can be subdivided into blazars and non-aligned non-thermal dominated AGNs depending on the orientation of their jets with respect to the line of sight.

   (a) Blazars. These are core-dominated flat or inverted radio spectrum radio loud AGNs. The radio core dominance and the flat radio spectrum together with strong and rapid variability (including superluminal motion) are the observational indicators that these objects point their radio jet in a direction that is closely aligned to our line of sight. Because of this very special perspective their light is strongly amplified by relativistic effects and the time-scales of observed variations are significantly shortened.

   Blazars are divided into two main subclasses, FSRQs and BL Lacs, depending on their optical spectral properties:

   (i) FSRQs or *Blazars of the QSO type* or BZQ (Massaro et al. 2009). These are blazars showing broad emission lines in their optical spectrum just like normal QSOs. This category includes objects normally referred to as FSRQs and broad-line radio galaxies.

   (ii) BL Lacs or *Blazars of the BL Lac type* or BZB (Massaro et al. 2009) These are objects normally called BL Lacs or BL Lacertae objects. Their radio compactness and broadband SED are very similar to that of strong lined blazars but they have no strong and broad lines in their optical spectrum (see e.g., Marchã et al. 1996).

   Sometimes, objects which show many of the hallmarks of blazars do not have optical spectra of sufficient quality to safely determine the presence of broad emission lines or to accurately measure their equivalent width. In these cases, the blazar subclass cannot be established and therefore these objects have to be referred to as BZU or *Blazars of the Unknown type* (see also Massaro et al. 2009).

   (b) Non-aligned non-thermal dominated AGNs. These sources are radio loud AGNs with jets pointed at large or intermediate (≈15°–40°, see Urry & Padovani 1995) angles with respect to the line of sight. For this reason they are sometimes called non-aligned, misaligned, or mispointed blazars. This category includes:

   (i) Radio galaxies or *non-aligned non-thermal dominated AGNs with no broad emission lines* which are sources often showing extended, double-sided radio jets/lobes pointing in opposite directions in the plane of the sky with respect to the central nucleus. The jet is clearly oriented at a very large angle with respect to the line of sight. The nuclear emission is similar to that of blazars but it is not amplified and therefore it is usually fainter than the extended emission, especially at low radio frequencies. The broad emission lines are not present in these sources because at such large angles they are hidden by the torus.

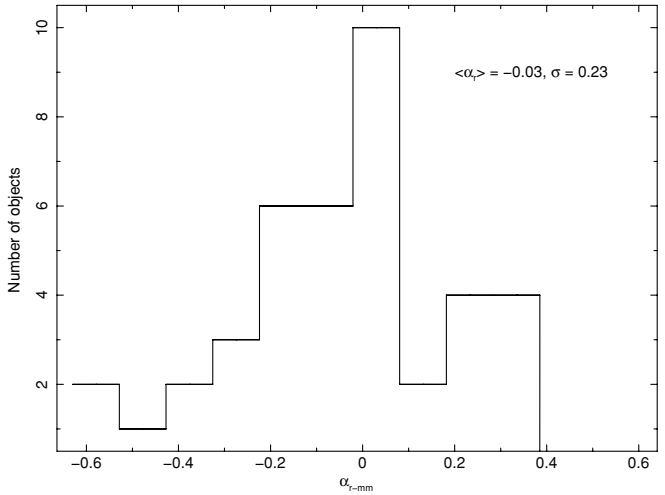

Figure 25. Distribution of radio spectral index ($f_r(\nu) \propto \nu^{\alpha_r}$) measured with the radio data of our 48 SED.

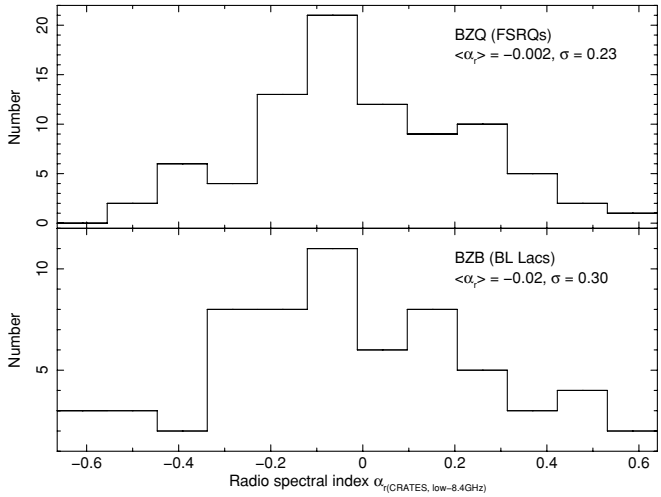

Figure 26. Distribution of radio spectral index ($f_r(\nu) \propto \nu^{\alpha_r}$) taken from the CRATES catalog, estimated between the CRATES low frequency, (∼1 GHz) and 8.4 GHz, for the sample of FSRQ (top panel) and BL Lacs (bottom panel).

(ii) SSRQ or *non-aligned non-thermal dominated AGNs with broad emission lines* which are sources usually known as steep spectrum radio quasars (SSRQ); hence, the orientation of the jet in these sources is thought to be intermediate between that of blazars and radio galaxies Urry & Padovani 1995).

In the literature, BL Lac objects are often subdivided into two or three subclasses depending on their SED. This classification was first introduced by Padovani & Giommi (1995) who used the peak energy of the synchrotron emission, which reflects the maximum energy the particles can be accelerated in the jet, to classify BL Lac into low-energy and high-energy synchrotron peak objects, respectively called LBL and HBL. In the following, we extend this definition to all types of non-thermal dominated AGNs using new acronyms (LSP, ISP, and HSP) to avoid confusion.

1. **LSP** or *low synchrotron peaked* blazars. These are sources where the synchrotron power peaks at low energy (i.e., in the far-IR or IR band or $\nu_{\rm peak} \lesssim 10^{14}$ Hz) and therefore their X-ray emission is flat ($\alpha_{\rm x} \approx 0.4$–$0.7$) and due to the rising part of the inverse Compton component (see Figure 30). At these relatively low energies the inverse Compton scattering occurs in the Thomson regime (see Section 7 and Figure 34).
2. **ISP** or *intermediate synchrotron peaked* blazars. Sources where the synchrotron emission peaks at intermediate energies ($10^{14} \lesssim \nu_{\rm peak} \lesssim 10^{15}$ Hz). In this case, the X-ray band includes both the tail of the synchrotron emission and the rise of the inverse Compton component (see Figure 30).
3. **HSP** or *high synchrotron peaked* blazars. Sources where the emitting particles are accelerated at much higher energies than in LSPs so that the peak of the synchrotron power reaches UV or higher energies ($\nu_{\rm peak} \gtrsim 10^{15}$ Hz) (see Figure 30; Padovani & Giommi 1996). Under these conditions the synchrotron emission dominates the observed flux in the X-ray band and the inverse Compton scattering occurs in the Klein Nishina regime (see Section 7 and Figure 34).

Ideally, blazars should be classified on the basis of a complete SED built with simultaneous data. As in most cases this is not possible, LSP or HSP objects can still be recognized by estimating their $\nu^S_{\rm peak}$ from $\alpha_{\rm ox}$ and $\alpha_{\rm ro}$ and from their X-ray spectral shape or by their radio to X-ray spectral slope (Padovani et al. 2003).

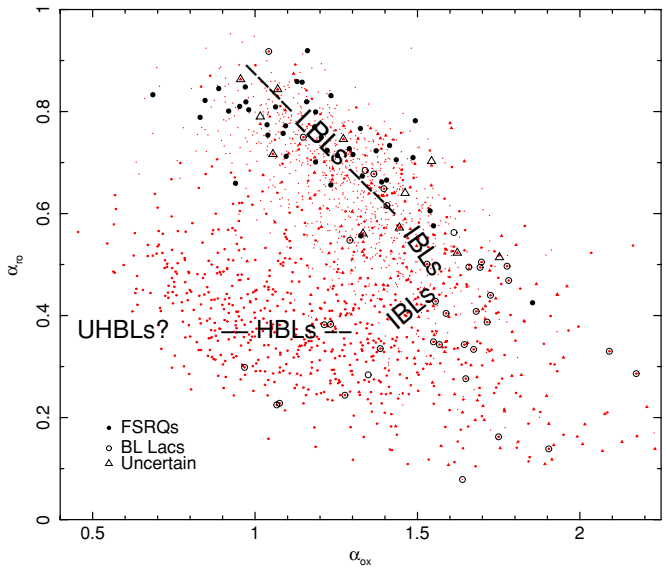

Figure 27. $\alpha_{\rm ox}$–$\alpha_{\rm ro}$ plot of the LBAS blazars (large symbols) compared to the sample of blazars in the BZCAT catalog for which there is radio optical and X-ray information (small red symbols). All γ-ray selected blazars are located in regions covered by previously known blazars. No new γ-ray type of blazars has been found; in particular, there is no evidence for the hypothetical population of UHBLs, with synchrotron peak in the γ-ray band ($\log(\nu^S_{\rm peak}) > 10^{20}$ Hz).
(A color version of this figure is available in the online journal.)

In LSP sources the X-ray spectrum is flat (photon spectral index $1.5 < \gamma_{\rm x} < 1.8$) and dominated by the IC component. In HSP sources, the X-ray spectrum is instead still due to synchrotron emission and it is usually steep ($\gamma_{\rm x} > 2$) if $\nu^S_{\rm peak} \lesssim 10^{17}$ Hz, but it can still be flat in extreme HSPs where $\nu^S_{\rm peak}$ is well into the X-ray band; the radio to X-ray spectral index, α_{rx}, of these blazars is less than 0.7. In ISP objects both the (steep) tail of the synchrotron emission and the (flat) rise of the IC component are within the X-ray band (see Figure 30), and $0.7 \lesssim \alpha_{rx} \lesssim 0.8$.

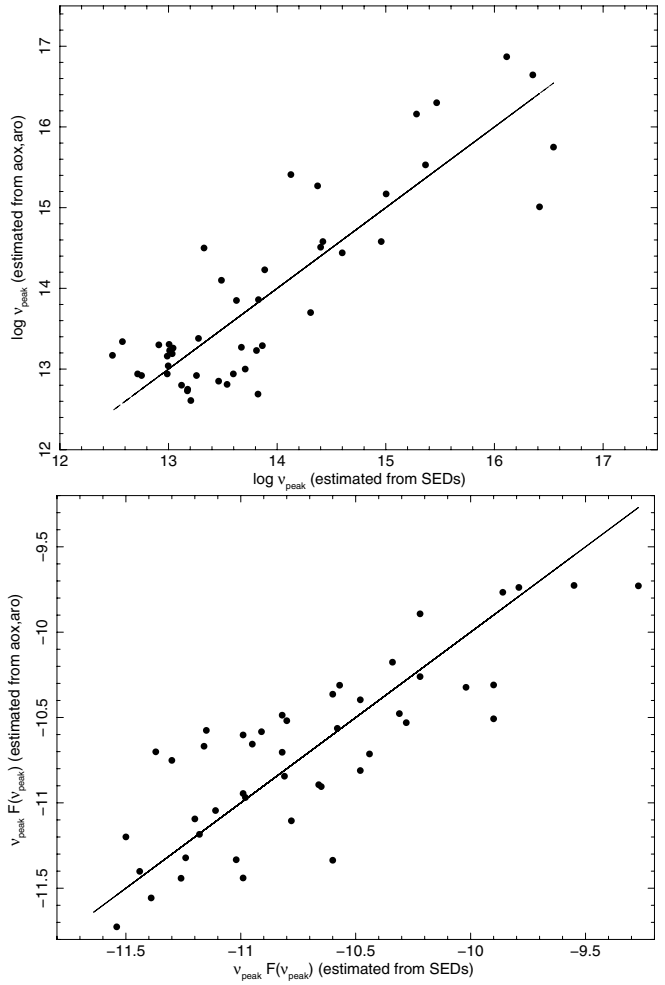

Figure 28. Synchrotron peak frequency ($\nu^S_{\rm peak}$, top panel) and its corresponding peak flux, $\nu^S_{\rm peak}$ $F(\nu^S_{\rm peak})$, bottom panel) value estimated from the SED of Figures 1–24 is plotted against the value estimated using the method based on $\alpha_{\rm ox}$ and $\alpha_{\rm ro}$ values (see the text for details). Despite the fact that $\alpha_{\rm ox}$ and $\alpha_{\rm ro}$ are based on non-simultaneous literature data, the scatter around the solid lines, representing perfect match, is ≈0.6 and ≈0.4 in log space for $\nu^S_{\rm peak}$ and $\nu^S_{\rm peak}$ $F(\nu^S_{\rm peak})$, respectively.

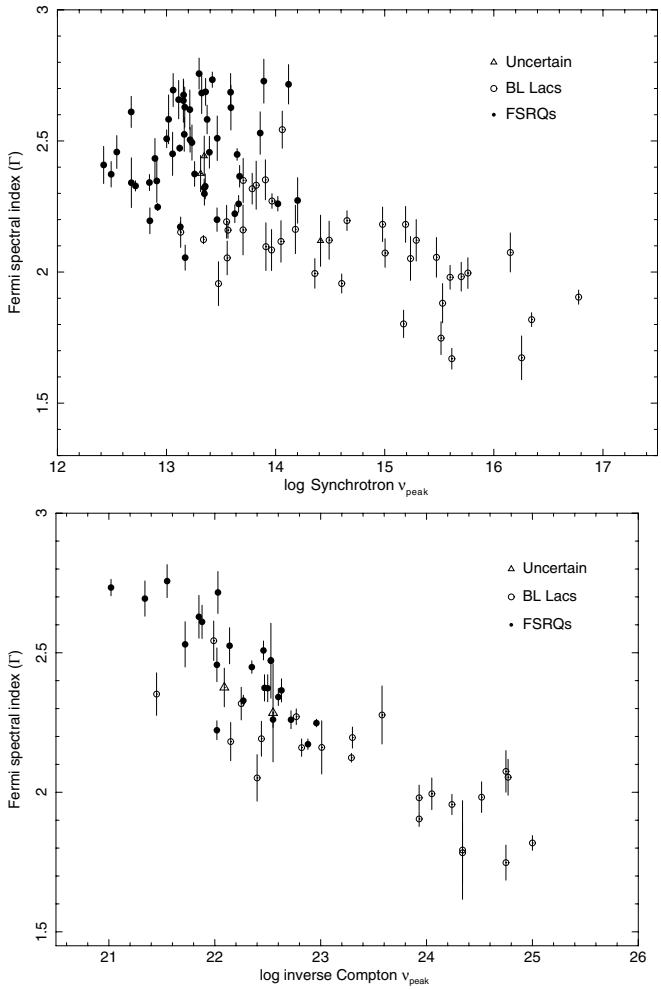

Figure 29. γ-ray power-law photon spectral index (Γ) is plotted against the log of synchrotron peak energy (top panel) and the log of inverse Compton peak energy (bottom panel). A clear correlation is present in both cases. Note that BL Lacs behave differently than FSRQs, spanning a wider range of both $\nu^S_{\rm peak}$ and spectral slopes.

6.1. The Distribution of Synchrotron and Inverse Compton Peak Frequencies

Now that we have a new SED-based classification of blazars and we have a reliable method of estimating $\nu^S_{\rm peak}$, we inspect the LBAS sample in terms of its content of LSP, ISP, and HSP objects and we compare it with that of samples selected in other energy bands.

The distribution of the synchrotron peak frequency ($\nu^S_{\rm peak}$) of LBAS blazars (estimated using the $\alpha_{\rm ox}$–$\alpha_{\rm ro}$ method) is plotted in Figure 31 for the FSRQ and the BL Lac subsamples (top and bottom panels respectively, solid histograms). While the $\nu^S_{\rm peak}$ distribution of FSRQs starts at $\sim10^{12.5}$ Hz, peaks at $\sim10^{13.3}$ Hz, and does not extend beyond $\approx10^{14.5}$ Hz, the distribution of BL Lacs is much flatter, starts at $\sim10^{13}$ Hz, and reaches much higher frequencies($\approx10^{17}$ Hz) than that of FSRQs. For comparison, in the same figure, we plot as a dotted histogram the distribution of $\nu^S_{\rm peak}$ of the sample of FSRQs and BL Lacs detected as foreground sources in the WMAP 3 yr microwave anisotropy maps (Giommi et al. 2009). In Figure 32, we compare the $\nu^S_{\rm peak}$ distribution of the LBAS sample with that of the X-ray selected sample of blazars detected in the *Einstein* Extended Medium Sensitivity Survey (EMSS; Gioia et al. 1990).

From Figures 31 and 32, we see that the $\nu^S_{\rm peak}$ distribution of FSRQs is consistent with being the same in the γ-ray, radio/microwave and in the X-ray band. We note that the large majority of FSRQs are of the LSP type while no FSRQs of the HSP type have been found at any frequency. On the contrary, the $\nu^S_{\rm peak}$ distribution of BL Lac objects is very different in the three energy bands. It is strongly peaked at $\sim10^{13.3}$ Hz in the microwave band, where HBL sources are very rare, whereas in the X-ray and γ-ray bands HSP sources are more abundant than LSPs.

Figure 33 shows the distribution of the inverse Compton peak frequency, $\nu^{\rm IC}_{\rm peak}$, of the FSRQs (dot-dashed histogram) and the BL Lacs (solid histogram) in the LBAS sample. The two distributions are quite different from the BL Lacs exhibiting much higher $\nu^{\rm IC}_{\rm peak}$ values, reproducing the case of the distribution of synchrotron $\nu^S_{\rm peak}$ shown in Figure 28. This is most likely due to the same reason that causes the different $\nu^S_{\rm peak}$ distributions in the two blazar subclasses.

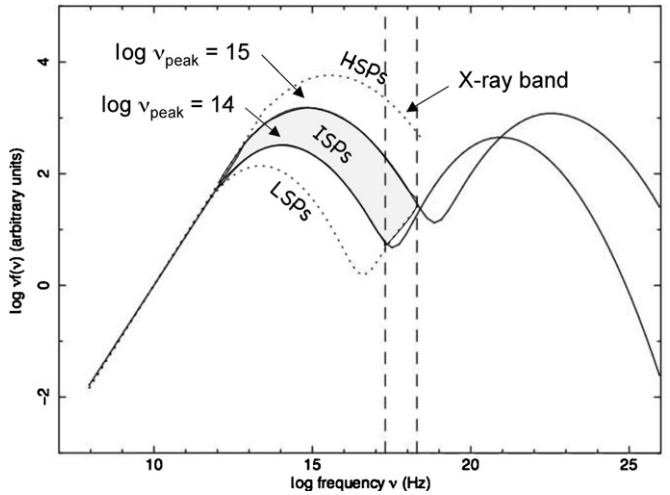

Figure 30. Definition of different blazar types based on the peak of the synchrotron component ($\nu^S_{\rm peak}$) in their SED. Low synchrotron peaked blazars, or LSP, are those where $\nu^S_{\rm peak}$ is located at frequencies lower then 10^{14} Hz (e.g., lower dotted line), for intermediate synchrotron peaked sources, or IPB, 10^{14} Hz $< \nu_{\rm peak_S} < 10^{15}$ Hz, (SED with peak within the gray area) while for high synchrotron peaked blazars, or HPS, $\nu^S_{\rm peak} > 10^{15}$ Hz (e.g., upper dotted line).

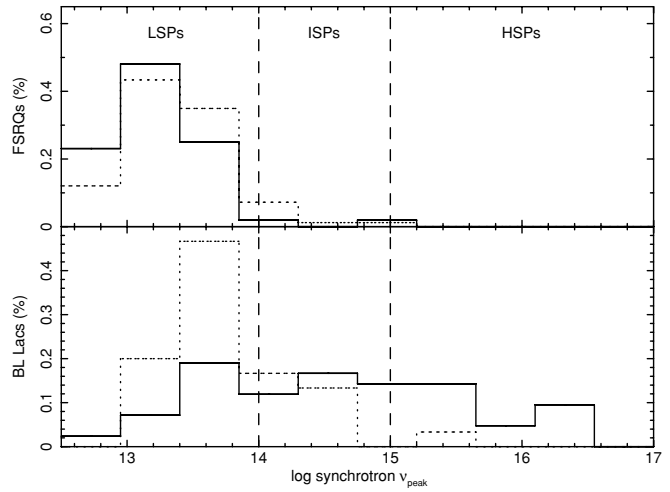

Figure 31. Distribution of synchrotron peak energy for the sample of LBAS FSRQ (solid line, top panel) and BL Lacs (solid line, bottom panel) compared to that of microwave selected blazars listed in the WMAP foreground sources catalog (dotted histograms).

6.2. Summary of Observational Findings and Sources Classification

The blazar observational parameters estimated from the quasi-simultaneous SED and from the broadband spectral indices $\alpha_{\rm ox}$, $\alpha_{\rm ro}$ for the cases where no simultaneous SED are available are summarized in Table 13 where we also classify our blazars according to the scheme described in Section 6. Column 1 gives the source name; Column 2 indicates if the quasi-simultaneous SED for the source is available; Column 3 gives the radio spectral index α_r as estimated in Section 5.1; Columns 4 and 5 give the synchrotron peak frequency ($\nu^S_{\rm peak}$) and intensity ($\nu^S_{\rm peak}$ F($\nu^S_{\rm peak}$)) estimated from the SED and with the $\alpha_{\rm ox}$–$\alpha_{\rm ro}$ method, respectively; Column 6 and 7 give the inverse Compton bump peak frequency ($\nu^{\rm IC}_{\rm peak}$) and intensity ($\nu^{\rm IC}_{\rm peak}$ F($\nu^{\rm IC}_{\rm peak}$)) estimated from the SED and from the correlation between $\nu^{\rm IC}_{\rm peak}$ and the γ-ray spectral slope (see Figure 29), respectively; Column 8 gives the particle peak energy (Lorentz factor) estimated assuming a simple SSC model ($\gamma^{\rm SSC}_{\rm peak} = \sqrt{3/4 \cdot \nu^{\rm IC}_{\rm peak}/\nu^S_{\rm peak}}$, see Equation (7) of Section 7); Column 9 gives the Compton dominance ($\nu^{\rm IC}_{\rm peak}$ F($\nu^{\rm IC}_{\rm peak}$)/$\nu^S_{\rm peak}$ F($\nu^S_{\rm peak}$)); Columns 10 and 11 give the source classification based on the optical spectrum and on the shape of the SED according to the scheme described above.

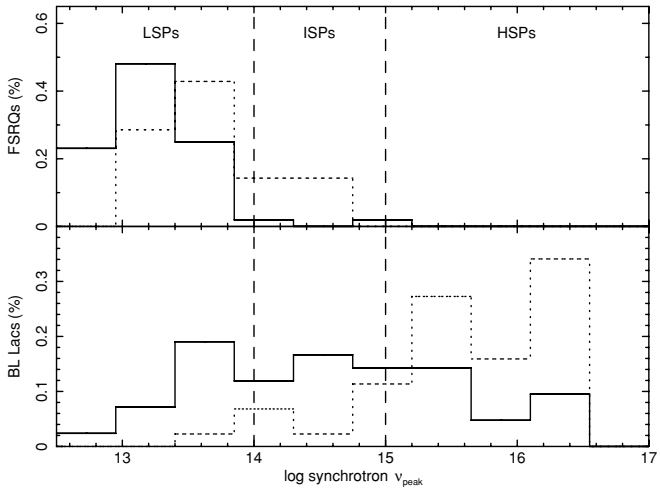

Figure 32. Distribution of synchrotron peak energy for the sample of LBAS FSRQ (solid line, top panel) and BL Lacs (solid line, bottom panel) compared to that of the sample of X-ray selected blazars of the *Einstein* EMSS (dotted histograms).

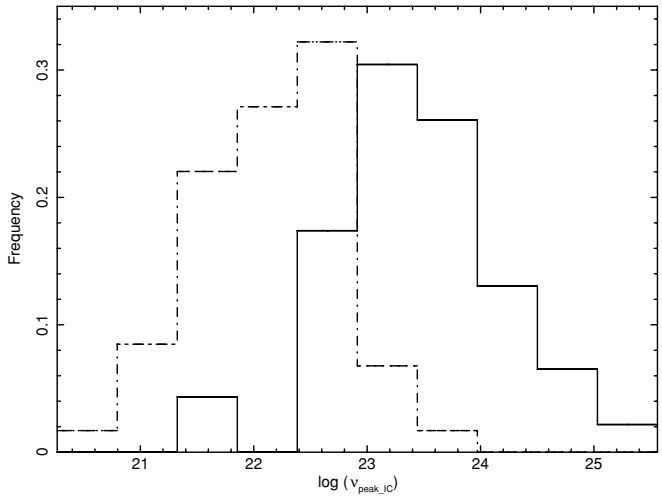

Figure 33. Distribution of inverse Compton peak frequency for the sample of LBAS FSRQ (dot-dashed line) and BL Lacs (solid line).

7. IMPLICATIONS FOR PHYSICAL MODELING

The quasi-simultaneous SED reported in this paper show the typical two bump shape that is seen in radio or X-ray selected blazars. According to current models the low energy bump is interpreted as synchrotron (S) emission from highly relativistic electrons, and the high energy bump is related to inverse Compton (IC) emission of various underlying radiation fields.

In the case of the synchrotron self-Compton model (SSC; Jones et al. 1974; Ghisellini & Maraschi 1989) the seed photons

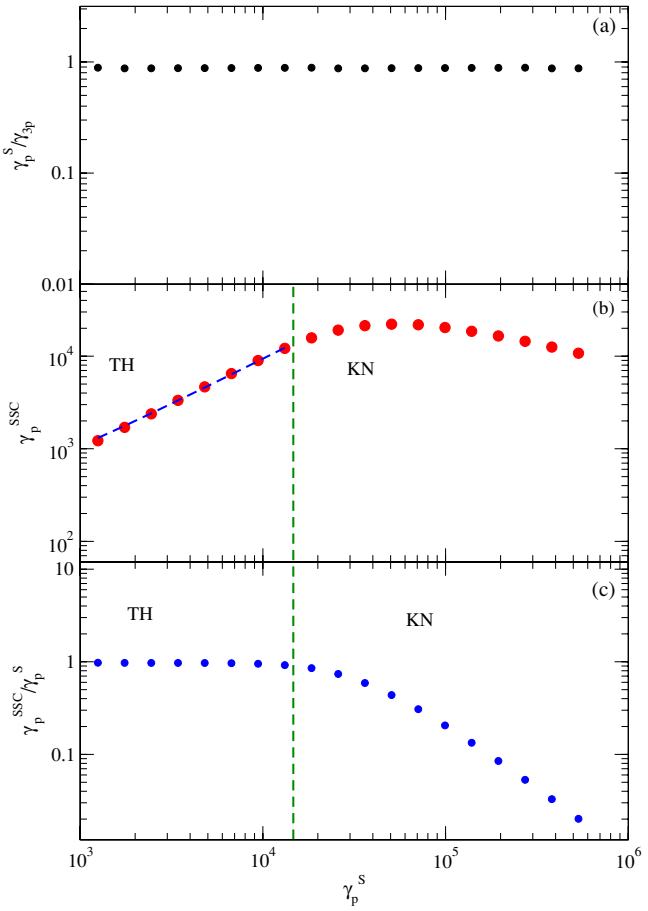

Figure 34. Estimate of $\gamma^{S}_{\rm peak}$ and $\gamma^{\rm SSC}_{\rm peak}$ for numerically computed SED in the case of a SSC model and using as electron distribution a log parabola $n(\gamma) = K \times 10^{r\,\log(\gamma/\gamma_{\rm peak})^2}$ with $\gamma_{\rm peak}$ ranging between 100 and 6×10^5, and the curvature parameter $r = 0.4$. The other model parameters are source size, $R = 10^{15}$ cm; a magnetic field, $B = 0.1$ G; a beaming factor, $\delta = 10$; and an electron density, $N = 1\ e^-{\rm cm}^{-3}$ ($N = \int n(\gamma)d\gamma$). From top to bottom: (a) the ratio of $\gamma^{S}_{\rm peak}$ to γ_{3p} as a function of $\gamma^{S}_{\rm peak}$. (b) $\gamma^{\rm SSC}_{\rm peak}$ as a function of $\gamma^{S}_{\rm peak}$, the transition from the TH trend (blue dashed line) to the KN region is evident for $\gamma > 2 \times 10^4$. (c) The ratio of $\gamma^{\rm SSC}_{\rm peak}$ to $\gamma^{S}_{\rm peak}$, also in this case, above the TH region (vertical dashed green line) the effect of the KN suppression is evident, $\gamma^{\rm SSC}_{\rm peak}$ gets to increasingly underestimate $\gamma^{S}_{\rm peak}$ as $\gamma_{\rm peak}$ is increasing.
(A color version of this figure is available in the online journal.)

for the IC process are the synchrotron photons produced by the same population of relativistic electrons.

In the case of the external radiation Compton (ERC) scenario (Sikora et al. 1994; Dermer et al. 2002), the seed photons for the IC process are typically UV photons generated by the accretion disk surrounding the black hole, and reflected toward the jet by the broad line region (BLR) within a typical distance from the accretion disk of the order of 1 pc. If the emission occurs at larger distances, the external radiation is likely to be provided by a dusty torus (Sikora et al. 2002). In this case, the photon field is typically peaked at IR frequencies.

In this section, we follow a phenomenological approach to obtain information about the peak Lorentz factor of the electron distribution ($\gamma_{\rm peak}$) most contributing to the synchroton emission and to the inverse Compton process. To test the methods used to estimate $\gamma_{\rm peak}$, we employ an accurate numerical model (Tramacere et al. 2009; Tramacere 2007; Massaro et al. 2006; Tramacere & Tosti 2003) that can reproduce both the SSC and ERC models. For the electron distribution we considered a log-

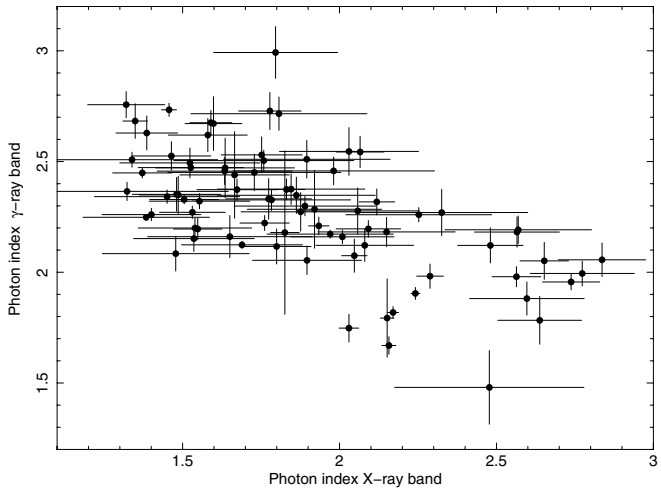

Figure 35. Power-law spectral slope in the γ-ray band is plotted against the spectral slope in the X-ray band. A clear correlation is present.

parabola of the form $n(\gamma) = K \times 10^{r\,\log(\gamma/\gamma_{\rm peak})^2}$ with $\gamma_{\rm peak}$ ranging between 100 and 6×10^5 and with curvature parameter $r = 0.4$ (Massaro et al. 2004; Tramacere et al. 2007). As input parameters for the benchmark SSC model we use a source size $R = 10^{15}$ cm, a magnetic field $B = 0.1$ G, a beaming factor $\delta = 10$, and an electron density $N = 1\ e^-{\rm cm}^{-3}$ ($N = \int n(\gamma)d\gamma$). In the case of the benchmark ERC model, we use the same set of parameters with the addition of the external photon field produced by the accretion disk and reflected by the BLR toward the emitting region with an efficiency $\tau_{\rm BLR} = 0.1$. The accretion disk radiation is modeled by a multitemperature black body, with an innermost disk temperature of 10^5 K.

7.1. The Synchrotron Peak Frequency

The dependence of the observed peak frequency of the synchrotron emission ($\nu^{S}_{\rm peak}$) on magnetic field intensity (B), electron Lorentz factor (γ), beaming factor (δ) and redshift (z) is given by

$$\nu^{S}_{\rm peak} = 3.2 \times 10^6 \left(\gamma^{S}_{\rm peak}\right)^2 B\delta/(1+z) = \nu^{S'}_{\rm peak}\delta/(1+z), \quad (6)$$

where $\nu^{S'}_{\rm peak}$ is the synchrotron peak frequency in the emitting region rest frame. A good estimate of $\gamma^{S}_{\rm peak}$ in terms of the differential electron energy distribution ($n(\gamma) = dN(\gamma)/d\gamma$) is given by the peak of $\gamma^3 n(\gamma)$, hereafter γ_{3p} (Tramacere et al. 2009; Tramacere et al. 2007). In panel (a) of Figure 34, we plot the ratio of $\gamma^{S}_{\rm peak}$ to γ_{3p} as a function of $\gamma^{S}_{\rm peak}$. The ratio is steady and very close to one over the whole range of $\gamma^{S}_{\rm peak}$ values. The value of $\gamma^{S}_{\rm peak}$ is estimated by fitting the peak of the numerically computed synchrotron SED with a log-parabolic analytical function. Note, however, that there is a degeneracy on the value of $\gamma^{S}_{\rm peak}$ given by the product $B\delta$. We discuss this point in the next subsection.

7.2. The Inverse Compton Peak Frequency

In a simple SSC model, and under the Thomson regime (TH) of the IC scattering, the observed peak frequency of the synchrotron component ($\nu^{S}_{\rm peak}$) is related to the observed peak frequency of the inverse Compton one ($\nu^{\rm IC}_{\rm peak}$) by the following

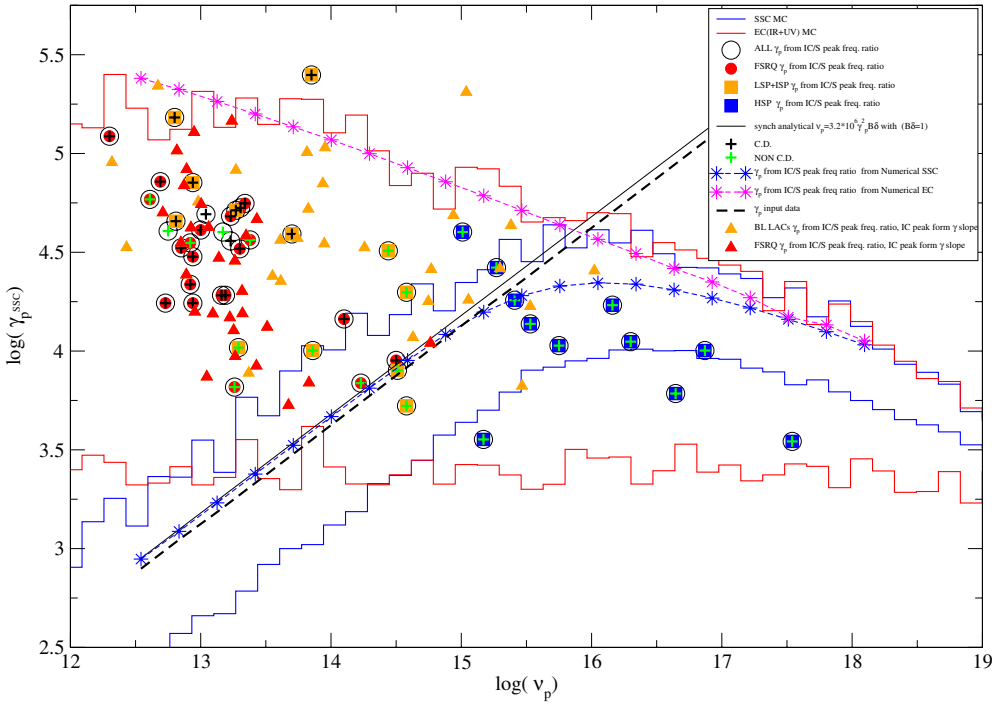

Figure 36. $\gamma_{\rm peak}^{\rm SSC}$ obtained by Equation (7) for the objects reported in Table 10. Blue solid boxes represent HPB objects, orange solid boxes represent IPBs/LPBs objects, and red solid circles represent FSRQs. The black solid line represents $\nu_{\rm peak}^{S}$ estimated by Equation (6) for both the ERC and the SSC numerical SED, the blue solid line represents $\gamma_{\rm peak}^{\rm SSC}$ estimated from Equation (7) applied to numerically computed the SSC SED, and the solid purple line represents the same for the case of ERC emission. The true value of the simulation is represented by the black dashed line. Parameters of the model are given in Section 7. The blue and red contours delimit the area covered by the estimate of $\gamma_{\rm peak}^{\rm SSC}$ for the case of SSC and ERC models respectively and for a Monte Carlo simulation with values of δ ranging between 10 and 15, B ranging between 0.01 and 1 G and T ranging between 10 and $10^{4.5}$ K.
(A color version of this figure is available in the online journal.)

relation:

$$\frac{\nu_{\rm peak}^{\rm IC}}{\nu_{\rm peak}^{S}} \simeq \frac{4}{3}\left(\gamma_{\rm peak}^{\rm SSC}\right)^2, \quad (7)$$

where $\gamma_{\rm peak}^{\rm SSC}$ is of the same order of $\gamma_{\rm peak}^{S}$. Panels (b) and (c) of Figure 34 show that (for the choice of SSC parameters reported above) this trend is valid only for $\gamma_{\rm peak}^{\rm SSC} \lesssim 2 \times 10^4$ where the transition from Thomson to Klein Nishina (KN) regime occurs. In the KN regime, Equation (7) is no longer valid: in fact, the kinematic limit for the maximum energy of the up-scattered photons in the emitting region rest frame is

$$\nu_{\rm max}^{\rm IC} = \frac{4\gamma^2 \nu_S}{1 + 4\gamma^2 (h\nu_S / m_e c^2)}. \quad (8)$$

As the energy of the seed photons in the electron rest frames increases, the maximum up-scattered photon energy approaches the energy of the up-scattering electron ($\gamma m_e c^2$). This means that the peak energy of the IC emission is no longer growing with $\gamma_{\rm peak}^2$ according to Equation (7), but it starts becoming smaller as shown in panels (b) and (c) of Figure 34. We note that this effect is particularly relevant for the case of HBL objects.

Other deviations from the trend given by Equation (7) occur when further radiative components add to a single zone SSC. In fact, for the case of the external Compton scenario, the observed peak frequency of the ERC component in terms of the frequency of the external photon field in the disk rest frame ($\nu_{\rm peak}^{\prime \rm EXT}$) reads

$$\frac{\nu_{\rm peak}^{\rm ERC}}{\nu_{\rm peak}^{\prime \rm EXT}\Gamma} \simeq \left(\frac{4}{3}\right)\left(\gamma_{\rm peak}^{\rm ERC}\right)^2 \delta/(1+z), \quad (9)$$

where $\nu_{\rm peak}^{\prime \rm EXT}\Gamma$ is the external photon field frequency transformed to the rest frame of the emitting region which is moving with a bulk Lorentz factor Γ, and assuming that the BLR radiation is isotropic.

If one uses Equation (7) in place of Equation (9) (an assumption justified by the fact that the UV and IR external radiation fields are usually dominated by the non-thermal synchrotron emission of the source), a significant bias on the value of $\gamma_{\rm peak}^{\rm ERC}$ is introduced in the ERC scenario. In fact, the resulting value of $\gamma_{\rm peak}$ is strongly overestimated in the case of external UV radiation field ($\gamma_{\rm peak}^{\rm SSC} \gg \gamma_{\rm peak}^{\rm ERC}$ and $\gamma_{\rm peak}^{\rm SSC} \gg \gamma_{\rm peak}^{S}$). In the case of the IR external radiation field, the bias is smaller but the measured value of $\gamma_{\rm peak}^{\rm SSC}$ is still overestimating both $\gamma_{\rm peak}^{\rm ERC}$ and $\gamma_{\rm peak}^{S}$.

In conclusion, when $\gamma_{\rm peak}$ is estimated through Equation (7) we expect two main biases:

1. a bias related to the KN effect, affecting mostly HBL objects, which leads to an underestimation of $\gamma_{\rm peak}$;
2. a bias related to the ERC scenario, affecting FSRQs and IBL objects, which yields an overestimate of $\gamma_{\rm peak}$.

These arguments provide an interesting diagnostic tool in the $\nu_{\rm peak}^{S}$–$\gamma_{\rm peak}^{\rm SSC}$ plane. Objects radiating mainly via the ERC mechanism are expected to lie above the $\nu_{\rm peak}^{S} \propto \gamma_{\rm peak}^{S}$ line, and objects radiating γ-rays mainly via the SSC mechanism are expected to lie along the $\nu_{\rm peak}^{S} \propto \gamma_{\rm peak}^{S}$ line in the case of the TH-IC regime, and below it in the case of KN-IC regime.

To test this scenario, we use the value of $\gamma_{\rm peak}^{\rm SSC}$ obtained by Equation (7) applied to the numerically computed SSC/ERC

SED, and we compare these trends with those obtained applying Equation (7) to the data of Table 13. Figure 36 shows the location of HSP objects (blue solid boxes), ISPs/LSPs objects (orange solid boxes) and FSRQs (red solid circles).

The values of $\gamma_{\rm peak}^{\rm SSC}$ estimated for the case of SSC emission (dashed blue line with stars) show clearly the effect of the transition from the TH to the KN regime. We note that all but two of the HBLs, lie below the $\nu_{\rm peak}^{S} \propto \gamma_{\rm peak}^{S}$ line. In particular all the HSP objects below the $\nu_{\rm peak}^{S} \propto \gamma_{\rm peak}^{S}$ line have $\gamma_{\rm peak}$ values below the prediction of the SSC scenario (solid blue line). In contrast, all the FSRQs and the LSP/ISP BL Lacs but one lie above the $\nu_{\rm peak}^{S} \propto \gamma_{\rm peak}^{S}$ line. The majority of the FSRQs objects have a value of $\gamma_{\rm peak}$ in excess of a factor of $\sim 10^4$ and limited by the prediction from the ERC model (purple dashed line with stars). The LBLs/IBLs sources are more uniformly distributed across the region delimited by the SSC TH prediction and by the ERC one. By further dividing the sample in Compton dominated (CD) objects ($\nu_{\rm peak}^{\rm IC} F(\nu_{\rm peak}^{\rm IC}) > 2\, \nu_{\rm peak}^{S} F(\nu_{\rm peak}^{S})$) and non-Compton dominated (NCD) objects ($\nu_{\rm peak}^{\rm IC} F(\nu_{\rm peak}^{\rm IC}) \leqslant 2\, \nu_{\rm peak}^{S} F(\nu_{\rm peak}^{S})$), we found that all the CD objects lie above the $\nu_{\rm peak}^{S} \propto \gamma_{\rm peak}^{S}$ line and populate the region between the SSC TH and the ERC regime, with the FSRQs clustering toward the ERC region.

Our analysis shows that the ERC model could explain the high CD values as well as the high values of $\gamma_{\rm peak}^{\rm SSC}$ estimated in the case of FSRQs and ISP/LSP BL Lacs. In order to explain the high values of $\gamma_{\rm peak}^{\rm SSC}$ obtained in the case of FSRQs in the context of single zone SSC emission model, a very small value of the magnetic field with ($B < 0.01$ G) is required.

As a final step, we discuss two additional effects that have consequences for the source distribution in this parameter space:

1. The $B\delta$ degeneracy on $\gamma_{\rm peak}^{S}$ can affect the transition region from the TH to KN regime, since high values of δ allow the TH regime to propagate toward higher frequencies.
2. The values of $\gamma_{\rm peak}$ in the case of a UV external radiation field (purple line Figure 36) constitute an upper limit to the observed values of $\gamma_{\rm peak}$, meaning that objects in the region below the ERC prediction line require a wider range of external photon energies, extending down to the IR band.

To take into account both these effects we perform Monte Carlo (MC) simulations. Specifically, we generate both the SSC and ERC numerical computation of the SED extracting δ, B, and the temperature of the accretion disk T from a random uniform distribution in order to cover a larger volume of the parameter space. We generate 1000 realizations, with δ ranging in the interval (10–15), B in the interval (0.01–1) G, and T in the interval (10–$10^{4.5}$) K. In Figure 36, the MC results for the case of SSC fall within the area delimited by the blue contour line, while the results in the case of the ERC model are delimited by the light red contour line.

We note that the MC simulations, compared to the ERC one for the only case of UV external photons (purple line), cover a much wider region of the parameter space. In the case of the MC SED, the range of temperatures of the BB emission allows us to take into account external photon fields peaking at IR frequencies. The resulting MC realizations populate the whole parameter space delimited by the ERC/UV (purple line) and the SSC/TH case (solid blue line, below about 10^{15} Hz). This suggests that in the ERC paradigm, the observed data, FSRQs (red circles), and ISP/LSP BL Lacs (orange square symbols), require external photon fields ranging form the UV down to the IR.

An alternative scenario that can explain the distribution of LBAS blazars in the plot of Figure 36 advocates the superposition of two or more SSC components with different intrinsic energetics reflecting different conditions of the associated components. Such composition of multiple relativistic plasmoids predicts that the large γ-ray excess, over a simple SSC model, observed in many LSP blazars in Figure 36, and the flat or concave shape of the γ-ray SED of a number of ISP/HSP blazars (see e.g., 3C66A, Figure 3, PKS 0447-439, Figure 6, 1ES 0502+675, Figure 7, and PG 1246+586, Figure 15) is the result of the presence of a second (or higher order) SSC component that is subdominant in the low-ν (radio-IR) range but emerges at higher energies, after the synchrotron peak of the first, less energetic, component (see, e.g., the case of S5 0716+714; Giommi et al. 2008). The combination of these multiple components is consistent with the intensity and spectral variability observed in these blazars. In such a model, the SED of HBL-type sources can be fitted with a primary SSC component which peaks at the IR/optical (S) and γ-ray band (IC), and with a second more energetic and usually more variable component, which peaks in the UV or X-ray band (S) and at ≈GeV energies (IC) thus explaining the widespread variability of these sources at TeV energies.

The predictions of this last model are quite different from those of the ERC model and can therefore be tested by future multifrequency observation campaigns. A specific discussion of the details of such a multi-component SSC model will be presented in a dedicated paper.

8. SUMMARY AND CONCLUSION

We have carried out a detailed investigation of the broadband (radio to high-energy γ-ray) spectral properties of the LBAS sample of *Fermi* bright blazars using a large number of multi-frequency simultaneous observations as well as literature and archival data. Using data obtained with *Fermi*, *Swift*, radio/millimeter telescopes, infra-red, and optical facilities we have been able to assemble simultaneous or quasi-simultaneous SED of a sizable and representative fraction of a homogeneous sample of blazars detected during a γ-ray all sky survey and not under special circumstances such as strong flaring activity. This collection of high-quality, well-sampled, nearly simultaneous, broadband SED for a large number of blazars is unprecedented and allowed us to estimate a number of important parameters characterizing the SED of γ-ray selected blazars and to address some key aspects of blazar demographics and physics. Our main results are as follows.

1. We derived reliable estimates of the frequency of the synchrotron ($\nu_{\rm peak}^{S}$) and of the inverse Compton peaks ($\nu_{\rm peak}^{\rm IC}$) for over 100 LBAS blazars. This was done directly from the simultaneous data for the 48 sources for which we have the SED (see Figures 1–24). For the remaining ones, $\nu_{\rm peak}^{S}$ and $\nu_{\rm peak}^{\rm IC}$ were estimated indirectly using a refined version of the method of Padovani & Giommi (1995) based on the position in the $\alpha_{\rm ox}$–$\alpha_{\rm ro}$ plane, for the former, and on the slope of the γ-ray spectrum for the latter, as the γ-ray spectral slope and $\nu_{\rm peak}^{\rm IC}$ are strongly correlated (see Figure 29). The determination of $\nu_{\rm peak}^{S}$ for the large majority of the sources in the sample prompted us to develop a new SED-based classification scheme for *all* non-thermal dominated AGNs based on an extension of the classification previously used for BL Lac objects only (see Section 6). We also find that the γ-ray spectral slope is strongly correlated

with the slope of the X-ray spectrum (see Figure 35). Such a correlation is expected at first order in synchrotron-inverse Compton scenarios; however, the expected spectral slopes in the two energy bands depend on the position of the Synchrotron (e.g., Padovani & Giommi 1996) and inverse Compton peaks broadening the correlation.

2. Considering that (a) all the γ-ray sources in the bright sample of *Fermi* blazars that have been associated with radio loud AGNs (Abdo et al. 2009a, 2009b) have α_{ox} and α_{ro} similar to those of previously known blazars (see Figure 27); (b) that among the only seven still unidentified sources with Galactic latitude $|b| > 10^{\circ}$, two are likely blazars (similar to the ones already identified as the γ-ray error region includes radio-optical candidates with $\alpha_{ox} \gtrsim 1.4$ and $\alpha_{ro} \sim 0.5$) and that the error region of the remaining five do not include any radio candidates brighter than 3 mJy, we can conclude that γ-ray selected blazars have broadband spectral properties similar to those of radio and X-ray discovered blazars implying that they are all drawn from the same underlying population. No evidence was found for the hypothetical class of UHBLs (see Ghisellini 1999; Giommi et al. 2001; Nieppola et al. 2006) characterized by a synchrotron emission that is so energetic as to reach the γ-ray band, and thus populate the extreme part of the α_{ox}–α_{ro} diagram defined by $0.2 < \alpha_{ro} < 0.4$ and $\alpha_{ox} \lesssim 0.7$ (see Figure 27). These sources, if bright and existing in good numbers, should have been found in a γ-ray survey such as LBAS, just as the population of HBL BL Lacs was discovered when X-ray surveys became available. Alternatively, UHBLs could be intrinsically weak γ-ray sources and/or mis-identified (Costamante et al. 2007) and their discovery must await the availability of much deeper samples than LBAS.
3. The distribution of the synchrotron peak frequency is very different for the FSRQ and BL Lac subsamples with values of ν^S_{peak} located between $10^{12.5}$ and $10^{14.5}$ Hz in FSRQ and between 10^{13} and 10^{17} Hz in BL Lacs (see Figure 31). This result rules out the existence of FSRQs of the HSP type (HBL in the old BL Lac nomenclature), consistent with what was also observed in radio, microwave, and X-ray surveys. The much larger ν^S_{peak} values that can be reached by BL Lacs explain their observed harder γ-ray spectral slopes and hence the much better sensitivity of the LAT instrument to these sources (see Figure 7 of Abdo et al. 2009b). This selection effect will be even stronger above a few GeV and fits with the well-known fact that TeV detected blazars are almost exclusively of the HSP (HBL) type. This also reproduces the case of the soft X-ray band where HSB BL Lacs (HBLs) are the dominant type of blazars.
4. A remarkable difference between LSP and HSP sources (see Section 6) is that more than 50% (10/16) of the HSP blazars with radio flux larger than 300 mJy at 1.4 GHz, in the BZCat catalog are detected in the LBAS sample while this fraction goes down to only $\lesssim$13% (58/452) for LSP blazars with radio flux larger than 500 mJy at 1.4 GHz. Note that the sample of undetected LBL blazars has similar overall properties than that of the detected ones, e.g., $\langle z \rangle_{detected} = 1.0$, $\langle z \rangle_{undetected} = 1.1$, $\langle V_{mag} \rangle_{detected} = 17.1$ and $\langle V_{mag} \rangle_{undetected} = 17.7$. However, some authors (e.g., Kovalev et al. 2009; Lister et al. 2009; Pushkarev et al. 2009; Kovalev 2009; Savolainen et al. 2010) showed that the LAT detected blazars might have larger Doppler boosting factors than undetected ones. A detailed comparison of all important parameters of γ-ray detected and undetected blazars will be done when the much larger catalog of γ-ray sources based on approximately one year of LAT data is available.
5. The minimum ν^S_{peak} of BL Lac objects of $\sim 10^{13}$ Hz is consistent with the results of Maselli et al. (2010) who conducted a careful search for very low synchrotron peaked BL Lac objects among the over 2000 blazars of the BZcat list and found them to be very rare or non-existent. The fact that the BL Lac minimum ν^S_{peak} appears to be larger than in FSRQs could be due to some intrinsic difference in the mechanism of particle acceleration in the two types of blazars or to a mere selection effect. In fact, the non-thermal emission of very low ν^S_{peak} BL Lacs would be minimal in the optical band (see Figure 30) causing them to be classified more easily as FSRQs rather than BL Lacs if low intensity broad lines (which would normally be below the non-thermal continuum) are present in this type of objects.

   We note that for LSP sources ($\nu^S_{peak} < 10^{14}$ Hz), the ratio of γ-ray detected FSRQs compared to BL Lacs is approximately four, i.e., a value similar to that seen in the radio and microwave bands ($\sim$6 both in the 1 Jy and in the WMAP3 samples; Stickel et al. 1991; Giommi et al. 2009). This strongly suggests that the mechanism that produces γ-rays is, at first order, the same in both LBL FSRQs and BL Lacs (see also Giommi et al. 2009).
6. The results of this study lead to the conclusion that a simple homogeneous, one-zone, SSC model cannot explain the SED of the majority of the detected sources, especially of the LBL type (see Figure 36). In addition, differential variability in the simultaneous optical and X-ray data observed in IBL and HBL objects (that is, close to the peak of the synchrotron component) suggests that multiple components are present in non-LBL blazars (e.g., S5 0716+714; Giommi et al. 2008), as also clearly shown by simultaneous X-ray/TeV campaigns (e.g., PKS 2155-304; Aharonian et al. 2009). Our results also show that ERC models can easily fit the data as they can cover a very wide part of the parameter space of Figure 36 (orange squares). However, models that are based on the presence of external radiation fields that are significantly different in FSRQs and BL Lacs, such as the broad-line region, accretion disk etc., must explain why (a) the ratio of the number of FSRQs and BL Lacs of the LBL type (which have similar γ-ray spectral slopes and therefore are affected in the same way by the higher LAT sensitivity to hard sources) is similar in radio/microwave selected samples (e.g., 1 Jy, WMAP) and in the LBAS γ-ray selected sample, and (b) why BL Lacs appear to show equal, or even larger, values of γ^{SSC}_{peak} (that is larger γ-ray excess above SSC) than FSRQs in Figure 36. Finally, any emission model should explain why only less than 13% of bright radio sources ($F > 0.5$ Jy at 1.4 GHz) of the LBL type are in the LBAS sample, while the other 87% with similar observational properties are below the LBAS detection threshold and may well be radiating close to simple SSC. We intend to address these topics in future papers.

The *Fermi*-LAT Collaboration acknowledges the generous support of a number of agencies and institutes that have supported the *Fermi*-LAT Collaboration. These include the National Aeronautics and Space Administration and the Depart-

ment of Energy in the United States, the Commissariat à l'Energie Atomique and the Centre National de la Recherche Scientifique/Institut National de Physique Nucléaire et de Physique des Particules in France, the Agenzia Spaziale Italiana and the Istituto Nazionale di Fisica Nucleare in Italy, the Ministry of Education, Culture, Sports, Science and Technology (MEXT), High Energy Accelerator Research Organization (KEK), and Japan Aerospace Exploration Agency (JAXA) in Japan, and the K. A. Wallenberg Foundation, the Swedish Research Council, and the Swedish National Space Board in Sweden. Additional support for science analysis during the operations phase from the following agencies is also gratefully acknowledged: the Istituto Nazionale di Astrofisica in Italy and the K. A. Wallenberg Foundation in Sweden. This research is based also on observations with the 100 m telescope of the MPIfR (Max-Planck-Institut für Radioastronomie) at Effelsberg. RATAN-600 observations are supported in part by the Russian Foundation for Basic Research (projects 01-02-16812 and 08-02-00545). Part of this work was supported by Georgian National Science Foundation grant GNSF/ST-08/4-404 The mid-infrared VISIR results are based on observations carried out at the European Southern Observatory under programmes ID 078.B-0366, 079.B-0448, and 081.B-0404. The Submillimeter Array is a joint project between the Smithsonian Astrophysical Observatory and the Academia Sinica Institute of Astronomy and Astrophysics and is funded by the Smithsonian Institution and the Academia Sinica. St. Petersburg University team acknowledges support from Russian RFBR foundation via grant 09-02-00092. AZT-24 observations are made within an agreement between Pulkovo, Rome, and Teramo observatories. We acknowledge the use of data and software facilities from the ASDC, managed by the Italian Space Agency (ASI). Part of this work is based on archival data and on bibliographic information obtained from the NASA/IPAC Extragalactic Database (NED) and from the Astrophysics Data System (ADS).

Facilities: Effelsberg, *Fermi*, OVRO:40m, *Swift*, WEBT

APPENDIX

UNFOLDING ANALYSIS

The purpose of the unfolding method is to estimate the true distribution (in this case the true source energy spectrum), given the observed one and assuming the knowledge of the smearing matrix, which describes the migration effects among the energy bins as well as the efficiencies (Mazziotta 2009). The smearing matrix is evaluated using the Monte Carlo package *Gleam*, a *Geant4* based simulation code of the instrument (Atwood et al. 2009), and taking into account the pointing history of the source under investigation. The unfolding analysis is performed selecting, from the initial data samples, events in an energy-dependent RoI centered on the position of the source under investigation. The maximum allowed angular separation of the events selected from the source position is a decreasing function of energy that reproduces the behavior of the PSF of the LAT. Events entering the LAT with a zenith angle larger than 105° with respect to the Earth reference frame and with an angle larger than 66.°4 with respect to the *Z*-axis in the instruments reference frame have been also excluded from this analysis. The observed spectrum built from the data selected according to the procedure described above includes the background contributions, that have to be subtracted before performing the unfolding. In the examples shown in Figures 37 and 38, the background counts have been evaluated from real data, considering the photons in an annulus external to the analysis RoI and rescaling them in each observed energy bin for the ratio between solid angles and live times. Once the source spectrum has been unfolded from the observed one, both statistical and systematic errors on the observed energy distribution can be easily propagated to the unfolded spectrum. In Figures 37 and 38, a comparison between the SED obtained with the unfolding and the spectra obtained with *gtlike* is shown for the blazars 3C454.3 and ASO0235+164. The unfolded spectra are consistent with the ones obtained from *gtlike*.

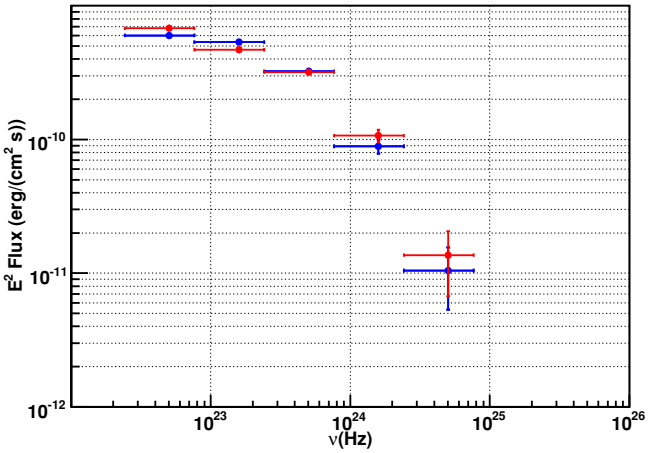

Figure 37. Comparison of the SED of the blazar 3C454.3 obtained with the maximum likelihood approach (red points) and with the unfolding technique (blue points).

(A color version of this figure is available in the online journal.)

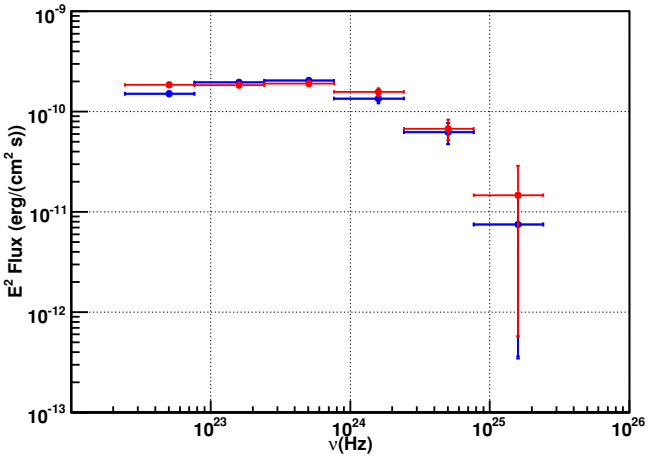

Figure 38. Comparison of the SED of the blazar ASO0235+164 obtained with the maximum likelihood approach (red points) and with the unfolding technique (blue points). The horizontal error bars represent the bin width.

(A color version of this figure is available in the online journal.)

REFERENCES

Abdo, A. A., et al. 2009a, ApJS, 183, 46
Abdo, A. A., et al. 2009b, ApJ, 700, 597
Abdo, A. A., et al. 2009c, ApJ, 701, L123
Abdo, A. A., et al. 2010a, ApJ, 710, 1271
Abdo, A. A., et al. 2010b, ApJ, submitted
Acciari, V. A., et al. 2009a, ApJ, 693, 104L
Acciari, V. A., et al. 2009b, ApJ, 707, 612
Aharonian, F., et al. 2009, ApJ, 696, L150
Ajello, M., et al. 2008, ApJ, 673, 96
Ajello, M., et al. 2009, ApJ, 699, 603
Albert, J., et al. 2006, ApJ, 639, 761
Albert, J., et al. 2007a, ApJ, 669, 862

Albert, J., et al. 2007b, ApJ, 666, 17L
Angelakis, E., et al. 2009, arXiv:0910.0643
Atwood, W. B., et al. 2009, ApJ, 697, 1071
Baars, J. W. M., Genzel, R., Pauliny-Toth, I. I. K., & Witzel, A. 1977, A&A, 61, 99
Barthelmy, S., et al. 2005, Space Sci. Rev., 120, 95
Bessel, M. S., Castelli, F., & Plez, B. 1998, A&A, 333, 231
Blandford, R. D., & Rees, M. J. 1978, in Pittsburgh Conference on BL Lac Objects, ed. A. M. Wolfe (Pittsburgh: Univ. Pittsburgh Press), 328
Burrows, D., et al. 2005, Space Sci. Rev., 120, 165
Cardelli, J. A., Clayton, G. C., & Mathis, J. S. 1989, ApJ, 345, 245
Colafrancesco, S., & Giommi, P. 2006, Chin. J. Astron. Astrophys., 6, 47
Costamante, L., Aharonian, F., & Khangulyan, D. 2007, in AIP Conf. Proc. 921, The First Glast Symp., ed. S. Ritz, P. Michelson, & C. A. Meegan (Melville, NY: AIP), 157
Costamante, L., & Ghisellini, G. 2002, A&A, 384, 56
Dermer, C. D., & Schlickeiser, R. 2002, ApJ, 575, 667
Donnarumma, I., et al. 2009, ApJ, 691, 13L
Errando, M., et al. 2008, in AIP Conf. Ser. 1085, High Energy Gamma-ray Astronomy, ed. F. A. Aharonian, W. Hofmann, & F. Rieger (Melville, NY: AIP), 423
Fitzpatrick, N. 1999, PASP, 111, 63
Fossati, G., Maraschi, L., Celotti, A., Comastri, A., & Ghisellini, G. 1998, MNRAS, 299, 433
Fuhrmann, L., Zensus, J. A., Krichbaum, T. P., Angelakis, E., & Readhead, A. C. S. 2007, in AIP Conf. Proc. 921, The First GLAST Symp., ed. S. Ritz, P. Michelson, & C. A. Meegan (Melville, NY: AIP), 249
Fuhrmann, L., et al. 2008, A&A, 490, 1019
Gehrels, N., et al. 2004, ApJ, 611, 1005
Ghisellini, G. 1999, Astrophys. Lett. Commun., 39, 17
Ghisellini, G., & Maraschi, L. 1989, ApJ, 340, 181
Gioia, I. M., Maccacaro, T., Schild, R. E., Wolter, A., Stocke, J. T., Morris, S. L., & Henry, J. P. 1990, ApJS, 72, 576
Giommi, P., Ansari, S. G., & Micol, A. 1995, A&AS, 109, 267
Giommi, P., & Colafrancesco, S. 2004, A&A, 414, 7
Giommi, P., Ghisellini, G., Padovani, P., & Tagliaferri, G. 2001, in AIP Conf. Proc. 599, X-ray Astronomy: Stellar Endpoints, AGN, and the Diffuse X-ray Background, ed. N. E. White, G. G. C. Palumbo, & G. Malaguti (Melville, NY: AIP), 441
Giommi, P., Piranomonte, S., Perri, M., & Padovani, P. 2005, A&A, 434, 385
Giommi, P., et al. 2002, in Proc. Int. Workshop, Blazar Astrophysics with BeppoSAX and Other Observatories, ed. P. Giommi, E. Massaro, & G. Palumbo (Noordwijk: ESA), 63
Giommi, P., et al. 2006, A&A, 456, 911
Giommi, P., et al. 2007, A&A, 468, 571
Giommi, P., et al. 2008, A&A, 487, L49
Giommi, P., et al. 2009, A&A, 508, 107
Grandi, P., & Palumbo, G. G. C. 2004, Science, 306, 998
Hartman, R. C., et al. 1999, ApJS, 123, 79
Healey, S. E., et al. 2007, ApJS, 171, 61
Healey, S. E., et al. 2008, ApJ, 175, 97
Hill, J. E., et al. 2004, Proc. SPIE, 5165, 217
Jones, T. W., Odell, S. L., & Stein, W. A. 1974, ApJ, 188, 353
Kalberla, P. M. W., et al. 2005, A&A, 440, 775
Korolkov, D. V., & Parijskij, Yu. N. 1979, Sky Tel., 57, 324
Kovalev, Y. Y. 2009, ApJ, 707, L56
Kovalev, Y. Y., Kovalev, Yu. A., Nizhelsky, N. A., & Bogdantsov, A. B. 2002, PASA, 19, 83
Kovalev, Y. Y., Nizhelsky, N. A., Kovalev, Yu. A., Berlin, A. B., Zhekanis, G. V., Mingaliev, M. G., & Bogdantsov, A. V. 1999, A&AS, 139, 545
Kovalev, Y. Y., Petrov, L., Fomalont, E. B., & Gordon, D. 2007, AJ, 133, 1236
Kovalev, Y. Y., et al. 2009, ApJ, 696, L17
Kubo, H., Takahashi, T., Madejski, G., Tashiro, M., Makino, F., Inoue, S., & Takahara, F. 1998, ApJ, 504, 693
Lagage, P. O., et al. 2004, Messenger, 117, 12
Lister, M. L., et al. 2009, ApJ, 696, L22
Marchã, M. J. M., Browne, I. W. A., Impey, C. D., & Smith, P. S. 1996, MNRAS, 281, 425
Massaro, E., Giommi, P., Leto, C., Marchegiani, P., Maselli, A., Perri, M., Piranomonte, S., & Sclavi, S. 2009, A&A, 495, 691
Massaro, E., Perri, M., Giommi, P., & Nesci, R. 2004, A&A, 413, 489
Massaro, E., Tramacere, A., Perri, M., Giommi, P., & Tosti, G. 2006, A&A, 448, 861
Maselli, A., Massaro, E., Nesci, R., Rossi, C., & Giommi, P. 2010, A&A, 512, 74
Mazziotta, M. N., & the Fermi-LAT Collaboration, 2009, arXiv:0912.1236
Monet, D. G., et al. 2003, AJ, 125, 984
Moretti, A., et al. 2005, Proc. SPIE, 5898, 360
Nieppola, E., Tornikoski, M., & Valtaoja, E. 2006, A&A, 445, 441
Nilsson 2007, A&A, 475, 199
Ott, M., Witzel, A., Quirrenbach, A., Krichbaum, T. P., Standke, K. J., Schalinski, C. J., & Hummel, C. A. 1994, A&A, 284, 331
Padovani, P., & Giommi, P. 1995, ApJ, 444, 567
Padovani, P., & Giommi, P. 1996, MNRAS, 279, 526
Padovani, P., Perlman, E. S., Landt, E., Giommi, P., & Perri, M. 2003, ApJ, 588, 128
Padovani, P., et al. 2006, A&A, 456, 131
Pittori, C., et al. 2009, A&A, 506, 1563
Pushkarev, A. B., Kovalev, Y. Y., Lister, M. L., & Savolainen, T. 2009, A&A, 507, L33
Poole, T. S., et al. 2008, MNRAS, 383, 627
Raiteri, C., et al. 2005, A&A, 438, 39
Raiteri, C., et al. 2008a, A&A, 485, L17
Raiteri, C., et al. 2008b, A&A, 480, 339
Readhead, et al. 1989, ApJ, 346, 566
Roming, P. W. A., et al. 2005, Space Sci. Rev., 120, 143
Sambruna, R. M., Maraschi, L., & Urry, C. M. 1996, ApJ, 463, 444
Savolainen, T., et al. 2010, A&A, 512, A24
Schlegel, D. J., Finkbeiner, D. P., & Davis, M. 1998, ApJ, 500, 525
Sikora, M., Begelman, M. C., & Rees, M. 1994, ApJ, 421, 153
Sikora, M., Blazejowski, M., Moderski, R., & Madejski, G. M. 2002, ApJ, 577, 78
Stickel, M., Padovani, P., Urry, C. M., Fried, J. W., & Kühr, H. 1991, ApJ, 374, 431
Tavani, M., et al. 2008, Nucl. Instrum. Method Phys. Res. A, 588, 52
Teshima, M. 2008, ATel, 1500, 1
Thompson, D. J., et al. 1993, ApJS, 86, 629
Toffolatti, L., Argueso Gomez, F., de Zotti, G., Mazzei, P., Franceschini, A., Danese, L., & Burigana, C. 1998, MNRAS, 297, 117
Tramacere, A. 2007, PhD Thesis, La Sapienza Univ., Rome
Tramacere, A., Massaro, F., & Cavaliere, A. 2007, A&A, 466, 521
Tramacere, A., & Tosti, G. 2003, New Astron. Rev., 47, 697
Tramacere, A., et al. 2009, A&A, 501, 879
Urry, M., & Padovani, P. 1995, PASP, 107, 803
Vercellone, S., et al. 2009, ApJ, 690, 1018
Villata, M., et al. 2007, A&A, 464, L5
Villata, M., et al. 2008, A&A, 481, L79
von Montigny, C., et al. 1995, ApJ, 440, 525
Weekes, T. C. 2008, in AIP Conf. Ser. 1085, High Energy Gamma-ray Astronomy, ed. F. A. Aharonian, W. Hofmann, & F. Rieger (Melville, NY: AIP), 3